



Delft University of Technology

Reduced Order Models For Unsteady Fluid Dynamic Optimization of Turbomachinery

Rubino, Antonio

DOI

[10.4233/uuid:11bb7f0d-c39b-4a32-8936-6ff8905543e1](https://doi.org/10.4233/uuid:11bb7f0d-c39b-4a32-8936-6ff8905543e1)

Publication date

2019

Document Version

Final published version

Citation (APA)

Rubino, A. (2019). Reduced Order Models For Unsteady Fluid Dynamic Optimization of Turbomachinery.
<https://doi.org/10.4233/uuid:11bb7f0d-c39b-4a32-8936-6ff8905543e1>

Important note

To cite this publication, please use the final published version (if applicable).
Please check the document version above.

Copyright

Other than for strictly personal use, it is not permitted to download, forward or distribute the text or part of it, without the consent of the author(s) and/or copyright holder(s), unless the work is under an open content license such as Creative Commons.

Takedown policy

Please contact us and provide details if you believe this document breaches copyrights.
We will remove access to the work immediately and investigate your claim.

**Reduced order models for
unsteady fluid dynamic optimization of turbomachinery**

Dissertation

for the purpose of obtaining the degree of doctor
at Delft University of Technology
by the authority of the Rector Magnificus, Prof.dr.ir. T.H.J.J. van der Hagen,
chair of the Board of Doctorates
to be defended publicly on
Tuesday 9 July 2019 at 15 o'clock

by

Antonio RUBINO

Master of Science in Mechanical Engineering, Delft University of Technology, The Netherlands
born in Avellino, Italy

This dissertation has been approved by the promotores.

Composition of the doctoral committee:

Rector Magnificus chairperson
Prof. dr. P. Colonna Delft University of Technology, promotor
Dr. M. Pini Delft University of Technology, copromotor

Independent members:

Prof. dr. S. Klein Delft University of Technology
Prof. dr. L. He Oxford University, United Kingdom
Prof. dr. D. Peitsch Technical University of Berlin, Germany
Dr. N. Wolfrum MTU Aero Engines AG, Germany
Dr. T. Economou Robert Bosch LLC, USA

This research has been supported by Bosch GmbH and the Applied and Engineering Sciences Domain (TTW) of the Dutch Organization for Scientific Research (NWO), Technology Program of the Ministry of Economic Affairs, grant number 13385.



ISBN 978-94-6375-455-2

Copyright © 2019 by Antonio Rubino. All rights reserved. No part of the material protected by this copyright notice may be reproduced or utilized in any form or by any means, electronic or mechanical, including photocopying, recording or by any information storage and retrieval system, without the prior permission of the author. An electronic version of this thesis is available at <http://repository.tudelft.nl>

Published by A. Rubino, Delft

Printed by Ridderprint in the Netherlands

Cover designed by Diego De Dominicis

*Dedicata ai miei genitori,
Alfonso e Maria*

Table of Contents

Summary	iii
Samenvatting	v
1 Introduction	1
1.1 Reduced-order models for unsteady flows	3
1.2 Adjoint-based unsteady automated design of turbomachinery in the context of ROMs	4
1.3 Motivation	5
1.4 Contribution	6
1.5 Outline	6
2 Adjoint-based fluid dynamic design optimization in quasi-periodic unsteady flow problems using a harmonic balance method	15
Abstract	16
2.1 Introduction	16
2.2 Method	17
2.2.1 Time Discretization	17
2.2.2 Harmonic Balance Operator	19
2.2.3 Time-domain harmonic balance	20
2.2.4 Governing equations of the adjoint solver	21
2.3 Results	23
2.3.1 NACA64A010 pitching airfoil	23
2.3.2 T106D-EIZ Turbine Cascade	27
2.4 Conclusions	35
3 Fully-turbulent adjoint method for the unsteady shape optimization of multi-row turbomachinery	41
Abstract	42
3.1 Introduction	42
3.2 Method	43
3.2.1 Fully-turbulent discrete adjoint	45
3.3 Application	47
3.3.1 Flow field analysis	48

3.3.2	Adjoint-based design sensitivities	52
3.3.3	Constant eddy viscosity (CEV) assumption	52
3.3.4	Constrained optimization	55
3.4	Performance assessment	59
3.4.1	2D stage	59
3.4.2	3D stage	59
3.5	Conclusions	62
4	A look-up table method based on unstructured grids and its application to non-ideal compressible fluid dynamic simulations	67
	Abstract	68
4.1	Introduction	68
4.1.1	Generation of the thermodynamic mesh	69
4.1.2	Search algorithm	70
4.2	Application to NICFD simulations	73
4.2.1	2D supersonic nozzle	74
4.2.2	Turbulent transonic 2D turbine cascade	74
4.2.3	Turbulent 3D supersonic ORC turbine cascade	75
4.3	Performance and memory assessment	80
4.3.1	Structured-grid LuT algorithm — <i>sg-LUT</i>	80
4.3.2	Comparison <i>sg-LUT</i> vs. <i>ug-LUT</i>	80
4.4	Conclusions	82
5	Adjoint-based unsteady optimization of turbomachinery operating with non-ideal compressible flows	89
	Abstract	90
5.1	Introduction	90
5.2	Method	91
5.2.1	Fully-turbulent discrete adjoint and non-ideal compressible flows	92
5.3	Adjoint-based optimization using <i>ug-LUT</i>	94
5.4	Shape optimization of an axial ORC turbine stage	97
5.5	Conclusions	101
6	Conclusion	105
6.1	Limitations and recommendations	107
6.2	Outlook	107
Acknowledgements		109
List of publications		111
About the author		113

Summary

The need to meet the increasingly demanding sustainability goals entails remarkable new challenges for technical innovation. Due to the crucial role of turbomachinery in present and future energy scenarios, advancements in turbomachinery performance by means of design methods represent a fundamental step towards global sustainable development.

Thanks to the progress in high-performance computing, automated turbomachinery design based on computational fluid dynamics is becoming more and more a viable option to tackle complex design problems. Because of the inherently unsteady nature of turbomachinery flows, optimization methods that are able to account for accurate time resolution of the flow features offer an increased level of simulation fidelity, if compared to methods that assume steady state flows. In this respect, unsteady-based optimization can lead not only to higher fluid dynamic performance, but it can also be seen as a key enabler to address complex multi-disciplinary design problems.

To date, however, most turbomachinery optimization methods are based on the assumption of steady state flows, as a consequence of the high computational cost associated with unsteady fluid dynamic simulations. Reduced order methods offer a computational efficient solution for shape optimization in unsteady flows.

This dissertation documents research on reduced order methods for unsteady adjoint-based shape optimization of turbomachinery. In particular, the reduced order methods considered are: the harmonic balance and the look-up table method for the estimation of thermo-physical fluid properties.

The research work resulted in an optimization framework based on a novel harmonic balance discrete adjoint solver, implemented in the open source code *SU2*. Results show the computational efficiency and effectiveness of the proposed optimization method to deal with unsteady turbomachinery design problems. For the exemplary test cases considered, the unsteady-based optimization led to increased fluid dynamic performance if compared to the optimization results based on steady state computations. Furthermore, the method was successfully employed for design problems of turbomachinery operating with non-ideal compressible flows.

Samenvatting

De noodzaak om aan de steeds veeleisendere duurzaamheidsdoelen te voldoen brengt opmerkelijke nieuwe uitdagingen met zich mee voor technologische innovatie. Gezien de cruciale rol van turbomachines in hedendaagse en toekomstige energie-scenarios, zet de vooruitgang in de prestaties van turbomachines door middel van ontwerpmethodes een fundamentele stap in de richting van globale duurzame ontwikkeling.

Dankzij de geboekte vooruitgang in supercomputers wordt geautomatiseerd ontwerp van turbomachines, gebruikmakend van computationele vloeistofdynamica, een steeds bereikbaardere optie om complexe ontwerpproblemen op te lossen. Vanwege de inherent instationaire aard van stromingen in turbomachines, kunnen optimalisatiemethodes die in staat zijn een accurate tijdsresolutie van de stromingskenmerken mee te nemen, een verhoogd waarheidsgehalte van de simulatie bieden in vergelijking met methodes die stationaire stroming aannemen. In dit opzicht kan optimalisatie gebaseerd op instationaire stroming niet alleen leiden naar verbeterde vloeistofdynamische prestaties, maar het kan ook gezien worden als sleutelmethode om complexe multidisciplinaire ontwerpproblemen aan te pakken.

Momenteel zijn de optimalisatiemethodes voor de meeste turbomachines gebaseerd op de stationaire stromingsaannname, vanwege de hoge berekeningstijd die gepaard gaat met instationaire vloeistofdynamische simulaties. Gereduceerde ordermethodes bieden een computationeel efficiënte oplossing voor vormoptimalisatie met instationaire stromingen.

Dit proefschrift documenteert onderzoek naar gereduceerde ordermethodes voor instationaire vormoptimalisatie van turbomachines gebaseerd op de adjointmethode. In het bijzonder zijn de volgende gereduceerde ordermethodes in beschouwing genomen: de harmonische balans en de opzoektafelmethode voor de inschatting van de thermofysische vloeistofeigenschappen. Het onderzoekswerk heeft geresulteerd in een optimalisatie framework gebaseerd op een nieuw uitgevonden harmonische balans discrete adjoint solver, gplementeerd in de open-source code *SU2*.

De resultaten tonen de computationele efficiëntie en effectiviteit van de voorgestelde optimalisatiemethode om om te gaan met instationaire ontwerpproblemen voor turbomachines. In de geanalyseerde illustratieve testgevallen leidde de instationaire optimalisatie tot verbeterde vloeistofdynamische prestaties in vergelijking met de optimalisatiereultaten gebaseerd op stationaire berekeningen. Bovendien is de methode met succes toegepast bij ontwerpproblemen met turbomachines die opereren met niet-ideale, samen-drukbare stromingen.

1

Introduction

The global increase in energy demand is posing a major challenge to sustainable growth. The scenario provided in the World Energy Outlook by the International Energy Agency estimates a global rise in energy demand of 30%, between today and 2040 [1]. In a context of strong urbanization and population expansion from 7.4 billion to 9 billion, for the same period, road travel and air traffic volumes are expected to double [2]. These long term projections, and associated international policy and economic objectives point to a challenging future also regarding energy technology innovation in order to comply with targets on sustainability.

Among energy conversion technologies, turbomachines play a crucial role in both the present and future energy scenarios. According to Ref. [3], more than 80% of worldwide electricity generation is obtained by means of thermal turbines. Furthermore, devices based on turbomachinery are essential in the transportation and industrial sector at large. Examples include gas turbine engines for aerospace propulsion, turbochargers for the automotive industry, and compressors for refrigeration applications.

In view of a more sustainable energy supply, turbomachinery design is challenged by an increasing number of performance requirements, often in new and unconventional applications. A substantial step forward is required for increasing power plants efficiency, thus mitigating the related emissions. Furthermore, the increasing market share of electricity produced by renewable energy systems, with its load variability, entails the introduction of highly flexible power plant operation [4, 5]. New turbomachinery concepts based on hydrogen combustion have proved their environmental advantage in a favorable hydrogen economy outlook; the realization of such devices implies a complete redesign of turbomachinery components. In the aviation sector, gas turbine engines will have to meet strict regulations on emissions and noise. Advancements in turbomachinery design are also required for decentralized energy conversion systems, of which a very representative example is given by the turbines of Organic Rankine Cycle power systems [6]. These low power output turbines (from few kW_e up to few MW_e) operate with organic fluids and, compared to the design of conventional steam and gas turbines, there is a lack of well-established design guidelines for optimal performance. Ultimately, in a more sustainable energy scenario, turbomachines can be regarded not only as a fundamental technology but also as a key enabler for new applications.

The reduction of overall emissions and noise, the need for highly flexible operational levels in power plants, and next-generation applications demand a paradigm shift in turbomachinery design towards more holistic and multi-disciplinary methods based on detailed multi-physical models. In this perspective, advanced computational methods can pave the way to fundamental technology improvements and the ability to effectively explore new design concepts [7].

Thanks to the progress in high-performance computing and the available computational resources, it is possible to employ more and more automated design methods based on computational fluid dynamics (CFD) for turbomachinery design [8]. These methods are based on optimization algorithms and can be classified as either non-deterministic or deterministic optimization procedures [9].

Non-deterministic algorithms, do not require any gradient information of the objective function. They are more suited for noisy objective functions and are less prone to

converge to local minima. Their computational cost highly depends on the number of design variables. Examples of commonly used non-deterministic optimization algorithms are: Evolutionary Algorithms [10–14], Simulated Annealing [15], Random Search [16], and Random Walk [17].

In contrast, deterministic methods, and in particular gradient-based algorithms, require the computation of the derivatives of the objective function. Because of this requirement, they perform worse than non-deterministic methods for discontinuous or noisy cost functions. However, once an accurate computation of the gradient of the objective function is provided, they are very computationally efficient. They might suffer from the problem of converging to local minima solutions and they require an efficient gradient estimation [9].

As previously outlined, the necessity for significant advancement in turbomachinery technology and innovation requires substantial progress in turbomachinery design methods. This entails the development of optimization algorithms based on accurate and detailed simulations in order to address complex problems. Given the inherently unsteady nature of turbomachinery flows, modeling time-dependent flow features for design purposes can lead to performance gain over steady state methods and it can give the possibility of tackling multi-disciplinary optimization problems.

However, taking into account unsteady effects, for automated turbomachinery shape optimization, is computationally onerous [18, 19]. A possible solution, to mitigate this computational burden, is employing reduced order models [20] (ROMs).

1.1 Reduced-order models for unsteady flows

Accurate modeling of time-dependent turbomachinery flows in computational fluid dynamics can be prohibitive if applied in combination with optimization algorithms, especially if the aim is to perform calculations for routine design.

In order to overcome this limitation, reduced-order models (ROMs) can be adopted to provide sufficiently accurate modeling of dynamic problems at a fraction of the computational cost. Because of this advantage, ROMs can bridge the gap between accurate unsteady flow analysis and the capability to perform unsteady multi-disciplinary CFD optimization [21].

Reduced-order models applied to automated design aim at representing only the most relevant physical behavior for design purposes. They can be seen as a way to provide, for a selected problem, a smaller number of degrees of freedom or unknowns when compared to high-fidelity models [22]. Some of the most common ROMs applied to CFD simulations are [20, 21]: Volterra series representations [23–25], proper orthogonal decomposition (POD) [26–28], surrogate-based recurrence framework (SBRF) [29], radial basis functions (RBF) [30], state-space modeling [31, 32], and harmonic balance (HB) [33–35].

In this work, two ROMs are considered to reduce the computational cost of unsteady simulations: the harmonic balance method and the look-up table method for the estimation of thermophysical fluid properties.

Harmonic Balance Method The harmonic balance (HB) method can be classified as a ROM that offers significant computational advantages, compared to time-accurate algorithms, when a discrete set of known frequencies characterizes the flow field. For this reason, it is a very attractive approach for turbomachinery applications if, especially for design purposes, the main unsteady effects are only related to the blade passing frequencies.

The HB method was initially applied to CFD simulations by linearization of the time-varying states [36], both for single and multiple frequencies. Although these formulations can accurately model stationary non-linearities of state variables (e.g., steady shock waves), they proved to be unsuitable in dealing with time-dependent non-linear effects. This is an essential drawback for turbomachinery simulations, especially in transonic or supersonic working conditions.

Non-linear harmonic balance methods have been developed and successfully applied to turbomachinery fluid dynamic computations [33–35, 37]. They allow modeling temporal non-linearities and resolving a known set of frequencies that do not need to be integer multiples of a fundamental harmonic.

Look-up Table Method For turbomachines operating with non-ideal fluid flows it is essential to accurately model thermophysical fluid properties by means of thermodynamic models based on complex equations of state (EoS) and transport property models. When complex EoS-based thermodynamic models are used in combination with CFD simulations, the computational cost increases significantly. This issue can become a bottleneck, particularly in demanding computational tasks, as it is the case for unsteady turbomachinery design.

Look-up table methods can be adopted to significantly decrease the simulation time related to the use of complex equations of state [38–40]. They consist of tabulating the needed properties in the thermodynamic region of interest. These properties are obtained with a preliminary calculation using an accurate fluid thermophysical model. During the flow simulation, the desired properties are retrieved utilizing a search algorithm and proper interpolation. Besides the reduction in computational cost, look-up table methods must be robust and accurate.

1.2 Adjoint-based unsteady automated design of turbomachinery in the context of ROMs

As previously discussed, the advancements in high-performance computing have enabled the increasing employment of optimization methods for automated design. Gradient-based optimization methods are very efficient but require an accurate evaluation of the necessary gradients. For this purpose, algorithms based on adjoint equations have gained growing interest owing to their ability to efficiently deal with problems in which the number of design variables is much higher than the number of objective functions or constraints [41]. The use of adjoint equations was initially introduced in the field of optimal

control theory [42] and subsequently in fluid dynamic optimization problems [43].

Although originally developed for the aerodynamic design of aircraft [44], adjoint-based optimization methods have been successfully extended to other engineering optimization problems, such as fluid-structure interaction [45, 46], heat transfer [47], and turbomachinery, to name a few.

For turbomachinery design most of the adjoint-based optimization methods have been developed considering steady state flows [48–55], due to the high computational cost and the large storage involved with unsteady algorithms. Recently, a time-accurate adjoint method has been developed for multi-row turbomachinery design problems adopting temporal coarsening to reduce the storage requirements [19]. The use of ROMs in combination with adjoint methods can offer an efficient alternative to time-accurate methods for performing automated design based on unsteady simulations.

Among ROMs, the harmonic balance (HB) method is a very attractive choice for adjoint-based turbomachinery shape optimization because of the following reasons: i. it allows to reach the final quasi-periodic solution, i.e., a solution characterized by a set of discrete frequencies not necessarily harmonically related, so that initial transients do not need to be resolved; ii. for design purposes just the main flow frequencies can be considered and spectral gaps can be enforced in order to save computational time; iii. in order to calculate the adjoint-based gradients, there is no need to store the large number of solutions required by a time-accurate adjoint approach.

Moreover, if unsteady shape optimization has to be performed for turbomachinery involving non-ideal compressible flows, look-up table (LuT) methods can be used to reduce the computational time required by the need of employing accurate thermodynamic models. In this regard, LuT methods have to be properly included for both flow and adjoint solver to obtain accurate design sensitivities.

1.3 Motivation

Unsteady adjoint-based shape optimization using HB has been applied to turbomachinery design. However, current methods are limited to adjoint formulations that consider single row [56], constant eddy viscosity or the impossibility to resolve for frequencies that are not harmonically related [57]. Furthermore, to date, unsteady adjoint-based optimization has never been applied to turbomachinery operating with non-ideal compressible flows.

In this regard, the study documented in this dissertation aims to advance current unsteady design methods for automated shape optimization of turbomachinery and to investigate the possible advantages of using reduced order models for unsteady design.

All the methods proposed in this research work are implemented in the open-source code *SU2*. This choice stems from the strong belief in the power of open-source communities and their positive social impact.

Finally, the development of unsteady optimization methods based on ROMs can be seen as a fundamental step towards multi-disciplinary turbomachinery design and for industrial applications in which automated design has to be performed routinely.

1.4 Contribution

The original contribution of this dissertation can be summarized as follows:

- A novel fully-turbulent adjoint-based harmonic balance (HB) optimization method has been formulated and implemented. The method, successfully validated versus second order accurate finite differences, does not require any assumption on the turbulence viscosity for the computation of design sensitivities.
- The fully-turbulent HB optimization method has been successfully extended and applied to multi-rows turbomachinery constrained shape optimization problems. Preliminary comparisons between steady and unsteady optimization have been carried out.
- For fast and accurate evaluation of thermophysical properties, a new tabulation method, based on unstructured grids of the thermodynamic region of interest, has been developed and applied to non-ideal compressible fluid dynamics problems.
- For the first time, unsteady adjoint-based optimization has been applied to the constrained shape optimization of turbines operating in the non-ideal compressible flow regime.
- All the methods of this dissertation have been implemented in the open source code *SU2*. This makes *SU2*, currently, the only open-source software having the capability to perform adjoint-based unsteady shape optimization of turbomachinery stages and to deal with unsteady design for non-ideal compressible fluid dynamics efficiently.

1.5 Outline

This dissertation contains material presented at international conferences or published in peer-review international journals. It is organized in six chapters and its content is summarized below.

Chapter 2 reports the formulation of the time-domain harmonic balance (HB) method and the derivation of the corresponding fully-turbulent discrete adjoint equations. The details of the implementation for automated design problems in quasi-periodic unsteady flows are discussed. The design sensitivities provided by the method are verified versus second-order finite difference and applied to the constrained shape optimization of a pitching airfoil and a turbine cascade.

Chapter 3 extends the adjoint-based HB optimization method from single-zone to multi-zone problems, i.e., problems involving multiple physical computational domains. The proposed algorithm is applied to the constrained shape optimization of an axial turbine

stage for two different working conditions. A comparison with steady optimization methods is discussed.

Chapter 4 introduces a novel tabulation method for fast and accurate estimation of thermophysical properties. The method is based on meshing the thermodynamic region of interest by means of unstructured grids, and it is applied to non-ideal compressible fluid dynamic simulations.

Chapter 5 presents the application of the HB-based discrete adjoint method to the shape optimization of turbomachinery for non-ideal compressible flow conditions. For this purpose, the tabulation method discussed in Chapter 4 is included in the discrete adjoint formulation in order to obtain accurate design sensitivities. The method is applied to the unsteady design of two exemplary Organic Rankine Cycle turbines.

Chapter 6 summarizes the main research findings of this work, outlining current limitations of the proposed methods, and giving an outlook to possible future research directions.

References

- [1] International Energy Agency, 2017. World Energy Outlook.
- [2] International Air Transport Association, 2015. Air Passenger Forecasts: Global Report.
- [3] EUTurbines, 2012. A Roadmap on Turbomachinery Research.
- [4] Gonzalez-Salazar, M. A., Kirsten, T., and Prchlik, L., 2017. “Review of the operational flexibility and emissions of gas-and coal-fired power plants in a future with growing renewables”. *Renewable and Sustainable Energy Reviews*.
- [5] de Groot, M., Crijns-Graus, W., and Harmsen, R., 2017. “The effects of variable renewable electricity on energy efficiency and full load hours of fossil-fired power plants in the european union”. *Energy*, **138**, pp. 575–589.
- [6] Colonna, P., Casati, E., Trapp, C., Mathijssen, T., Larjola, J., Turunen-Saaresti, T., and Uusitalo, A. “Organic Rankine Cycle Power Systems: From the Concept to Current Technology, Applications, and an Outlook to the Future”. p. 100801.
- [7] Slotnick, J., Khodadoust, A., Alonso, J., Darmofal, D., Gropp, W., Lurie, E., and Mavriplis, D., 2014. “CFD vision 2030 study: a path to revolutionary computational aerosciences”.
- [8] Li, Z., and Zheng, X., 2017. “Review of design optimization methods for turbomachinery aerodynamics”. *Progress in Aerospace Sciences*, **93**, pp. 1–23.
- [9] Verstraete, T., 2010. “Introduction to optimization and multidisciplinary design”. In *Introduction to optimization and multidisciplinary design in aeronautics and turbomachinery*. VKI, Lecture Series, pp. 1–38.
- [10] Holland, J. H., 1992. *Adaptation in natural and artificial systems: an introductory analysis with applications to biology, control, and artificial intelligence*. MIT press.
- [11] Rechenberg, I., 1973. *Evolutionsstrategie—Optimierung technischer Systeme nach Prinzipien der biologischen Evolution*. Frommann-Holzboog.
- [12] Zitzler, E., and Thiele, L., 1999. “Multiobjective evolutionary algorithms: a comparative case study and the strength pareto approach”. *IEEE transactions on Evolutionary Computation*, **3**(4), pp. 257–271.

- [13] Goldberg, D. E., 1989. *Genetic Algorithms in Search, Optimization and Machine Learning*, 1st ed. Addison-Wesley Longman Publishing Co., Inc., Boston, MA, USA.
- [14] Storn, R., and Price, K., 1997. “Differential evolution—a simple and efficient heuristic for global optimization over continuous spaces”. *Journal of global optimization*, **11**(4), pp. 341–359.
- [15] van Laarhoven, P., and Aarts, E., 1987. *Simulated Annealing: Theory and Applications*, 1st ed., Vol. 37. Springer.
- [16] Price, W., 1983. “Global optimization by controlled random search”. *Journal of Optimization Theory and Applications*, **40**(3), pp. 333–348.
- [17] Vanderplaats, G. N., 2001. *Numerical optimization techniques for engineering design*. Vanderplaats Research and Development, Incorporated.
- [18] Mavriplis, D. J., 2006. “Multigrid solution of the discrete adjoint for optimization problems on unstructured meshes”. *AIAA journal*, **44**(1), pp. 42–50.
- [19] Ntanakas, G., Meyer, M., and Giannakoglou, K. C., 2018. “Employing the time-domain unsteady discrete adjoint method for shape optimization of three-dimensional multirow turbomachinery configurations”. *Journal of Turbomachinery*, **140**(8), p. 081006.
- [20] Ghoreyshi, M., Jirasek, A., and Cummings, R. M., 2014. “Reduced order unsteady aerodynamic modeling for stability and control analysis using computational fluid dynamics”. *Progress in Aerospace Sciences*, **71**, pp. 167–217.
- [21] Lucia, D. J., Beran, P. S., and Silva, W. A., 2004. “Reduced-order modeling: new approaches for computational physics”. *Progress in Aerospace Sciences*, **40**(1-2), pp. 51–117.
- [22] Amsallem, D., and Farhat, C., 2008. “Interpolation method for adapting reduced-order models and application to aeroelasticity”. *AIAA Journal*, **46**(7), pp. 1803–1813.
- [23] Silva, W. A., 1993. “Application of nonlinear systems theory to transonic unsteady aerodynamic responses”. *Journal of Aircraft*, **30**(5), pp. 660–668.
- [24] Silva, W., 2005. “Identification of nonlinear aeroelastic systems based on the volterra theory: progress and opportunities”. *Nonlinear Dynamics*, **39**(1-2), pp. 25–62.
- [25] Da Ronch, A., Badcock, K. J., Khrabrov, A., Ghoreyshi, M., and Cummings, R., 2011. “Modeling of unsteady aerodynamic loads”. In AIAA Atmospheric Flight Mechanics Conference, p. 6524.

-
- [26] Hall, K., Thomas, J., and Dowell, E., 1999. “Reduced-order modelling of unsteady small-disturbance flows using a frequency-domain proper orthogonal decomposition technique”. In 37th Aerospace Sciences Meeting and Exhibit, p. 655.
 - [27] LeGresley, P., and Alonso, J., 2000. “Airfoil design optimization using reduced order models based on proper orthogonal decomposition”. In Fluids 2000 conference and exhibit, p. 2545.
 - [28] Willcox, K., and Peraire, J., 2002. “Balanced model reduction via the proper orthogonal decomposition”. *AIAA Journal*, **40**(11), pp. 2323–2330.
 - [29] Glaz, B., Liu, L., and Friedmann, P. P., 2010. “Reduced-order nonlinear unsteady aerodynamic modeling using a surrogate-based recurrence framework”. *AIAA journal*, **48**(10), pp. 2418–2429.
 - [30] Ghoreyshi, M., and Cummings, R. M., 2013. “Challenges in the aerodynamics modeling of an oscillating and translating airfoil at large incidence angles”. *Aerospace Science and Technology*, **28**(1), pp. 176–190.
 - [31] Goman, M., and Khrabrov, A., 1994. “State-space representation of aerodynamic characteristics of an aircraft at high angles of attack”. *Journal of Aircraft*, **31**(5), pp. 1109–1115.
 - [32] Kyle, H., Lowenberg, M., and Greenwell, D., 2004. “Comparative evaluation of unsteady aerodynamic modelling approaches”. In AIAA Atmospheric Flight Mechanics Conference and Exhibit, p. 5272.
 - [33] Hall, K. C., Thomas, J. P., and Clark, W. S., 2002. “Computation of unsteady nonlinear flows in cascades using a harmonic balance technique”. *AIAA journal*, **40**(5), pp. 879–886.
 - [34] Gopinath, A., Van Der Weide, E., Alonso, J., Jameson, A., Ekici, K., and Hall, K., 2007. “Three-dimensional unsteady multi-stage turbomachinery simulations using the harmonic balance technique”. In 45th AIAA Aerospace Sciences Meeting and Exhibit, p. 892.
 - [35] Sicot, F., Dufour, G., and Gourdain, N., 2012. “A time-domain harmonic balance method for rotor/stator interactions”. *Journal of Turbomachinery*, **134**(1), p. 011001.
 - [36] Verdon, J. M., and Caspar, J. R., 1984. “A linearized unsteady aerodynamic analysis for transonic cascades”. *Journal of Fluid Mechanics*, **149**, p. 403429.
 - [37] He, L., and Ning, W. “Efficient approach for analysis of unsteady viscous flows in turbomachines”. pp. 2005–2012.
 - [38] Yiu, K., Greaves, D., Cruz, S., Saalehi, A., and Borthwick, A., 1996. “Quadtree grid generation: information handling, boundary fitting and cfd applications”. *Computers & Fluids*, **25**(8), pp. 759–769.

- [39] Xia, G., Li, D., and Merkle, C. L., 2007. “Consistent properties reconstruction on adaptive cartesian meshes for complex fluids computations”. *Journal of Computational Physics*, **225**(1), pp. 1175–1197.
- [40] Pini, M., Spinelli, a., Persico, G., and Rebay, S., 2015. “Consistent look-up table interpolation method for real-gas flow simulations”. *Computers & Fluids*, **107**, Jan., pp. 178–188.
- [41] Giles, M. B., and Pierce, N. A., 2000. “An introduction to the adjoint approach to design”. *Flow, turbulence and combustion*, **65**(3-4), pp. 393–415.
- [42] Lions, J. L., 1971. *Optimal control of systems governed by partial differential equations (Grundlehren der Mathematischen Wissenschaften)*, Vol. 170. Springer Berlin.
- [43] Pironneau, O., 1974. “On optimum design in fluid mechanics”. *Journal of Fluid Mechanics*, **64**(1), pp. 97–110.
- [44] Jameson, A., 1988. “Aerodynamic design via control theory”. *Journal of scientific computing*, **3**(3), pp. 233–260.
- [45] Mishra, A., Mani, K., Mavriplis, D., and Sitaraman, J., 2015. “Time dependent adjoint-based optimization for coupled fluidstructure problems”. *Journal of Computational Physics*, **292**, pp. 253 – 271.
- [46] Sanchez, R., Albring, T., Palacios, R., Gauger, N. R., Economou, T. D., and Alonso, J. J. “Coupled adjoint-based sensitivities in large-displacement fluid-structure interaction using algorithmic differentiation”. *International Journal for Numerical Methods in Engineering*, **113**(7), pp. 1081–1107.
- [47] Kontoleontos, E. A., Papoutsis-Kiachagias, E. M., Zymaris, A. S., Papadimitriou, D. I., and Giannakoglou, K. C., 2013. “Adjoint-based constrained topology optimization for viscous flows, including heat transfer”. *Engineering Optimization*, **45**(8), pp. 941–961.
- [48] Papadimitriou, D., and Giannakoglou, K., 2006. “A continuous adjoint method for the minimization of losses in cascade viscous flows”. In 44th AIAA Aerospace Sciences Meeting and Exhibit, p. 49.
- [49] Corral, R., and Gisbert, F., 2008. “Profiled end wall design using an adjoint navier–stokes solver”. *Journal of Turbomachinery*, **130**(2), p. 021011.
- [50] Luo, J., Xiong, J., Liu, F., and McBean, I., 2011. “Three-dimensional aerodynamic design optimization of a turbine blade by using an adjoint method”. *Journal of Turbomachinery*, **133**(1), p. 011026.
- [51] Wang, D., and He, L., 2010. “Adjoint aerodynamic design optimization for blades in multistage turbomachinespart i: Methodology and verification”. *Journal of Turbomachinery*, **132**(2), p. 021011.

- [52] Wang, D., He, L., Li, Y., and Wells, R., 2010. “Adjoint aerodynamic design optimization for blades in multistage turbomachines part ii: Validation and application”. *Journal of Turbomachinery*, **132**(2), p. 021012.
- [53] Walther, B., and Nadarajah, S., 2015. “Optimum shape design for multirow turbomachinery configurations using a discrete adjoint approach and an efficient radial basis function deformation scheme for complex multiblock grids”. *Journal of Turbomachinery*, **137**(8), p. 081006.
- [54] Pini, M., Persico, G., Pasquale, D., and Rebay, S., 2015. “Adjoint method for shape optimization in real-gas flow applications”. *Journal of Engineering for Gas Turbines and Power*, **137**(3), p. 032604.
- [55] Vitale, S., Albring, T. A., Pini, M., Gauger, N. R., and Colonna, P. “Fully turbulent discrete adjoint solver for non-ideal compressible flow applications”. *Journal of the Global Power and Propulsion Society*, **1**, pp. 252 – 270.
- [56] Huang, H., and Ekici, K., 2014. “A discrete adjoint harmonic balance method for turbomachinery shape optimization”. *Aerospace Science and Technology*, **39**, pp. 481–490.
- [57] Ma, C., Su, X., and Yuan, X., 2017. “An efficient unsteady adjoint optimization system for multistage turbomachinery”. *Journal of Turbomachinery*, **139**(1), p. 011003.

2

Adjoint-based fluid dynamic design optimization in quasi-periodic unsteady flow problems using a harmonic balance method

Part of the contents of this chapter appeared in:

Adjoint-based fluid dynamic design optimization in quasi-periodic unsteady flow problems using a harmonic balance method. Rubino, A., Pini, M., Colonna, P., Albring T., Nimmagadda, S., Economou, T., and Alonso, J.

Journal of Computational Physics, 2018

Abstract Shape optimization in unsteady flow problems enables the consideration of dynamic effects on design. The ability to treat unsteady effects is attractive, as it can provide performance gains when compared to steady-state design methods for a variety of applications in which time-varying flows are of paramount importance. This is the case, for example, in turbomachinery or rotorcraft design. Given the high computational cost involved in time-accurate design problems, adjoint-based shape optimization is a promising option. However, efficient sensitivity analysis should also be accompanied by a significant decrease in computational cost for the primal flow solution, as well. Reduced-order models, like those based on the harmonic balance concept, in combination with the calculation of gradients via adjoint methods, are proposed for the efficient solution of a certain class of aerodynamics optimization problems. The harmonic balance method is applicable if the flow is characterized by discrete finite dominant flow frequencies that do not need to be integer multiples of a fundamental harmonic. A fully-turbulent harmonic balance discrete adjoint formulation based on a duality-preserving approach is proposed. The method is implemented by leveraging algorithmic differentiation and is applied to two test cases: the constrained shape optimization of both a pitching airfoil and a turbine cascade. A key advantage of the current approach is the accurate computation of gradients as compared to second order finite differences without any approximation in the linearization of the turbulent viscosity. The shape optimization results show significant improvements for the selected time-dependent objective functions, demonstrating that design problems involving almost-periodic unsteady flows can be tackled with manageable computational effort.

2.1 Introduction

The advancement of computational resources has enabled the application of CFD-based design methods to complex shapes, discretized on large domains, often in combination with high fidelity models [1, 2].

Optimization methods for design purposes have significantly improved, offering the possibility to deal with complex problems at a reduced computational cost [3–5]. In particular, adjoint-based optimization methods [6, 7] provide a very efficient approach for computing design sensitivities irrespective of the number of design variables. In applications where the number of design variables is considerably greater than the number of objective functions, adjoint methods allow the computation of optimal solutions in the most cost-effective way, making them well suited for complex industrial applications [8–10].

To date, most of the work on adjoint methods has been based on the assumption of steady flow. Obtaining the adjoint solution of an unsteady flow problem can pose a challenge because of the associated large computational and memory requirements [11]. However, accounting for time-dependent flow phenomena in the optimization process is often essential in applications characterized by intrinsic unsteady effects, such as the aero-dynamic design of rotorcraft, turbomachinery, open rotors, and wind turbines, to name a few. Furthermore, unsteady adjoint-based optimization methods can pave the way to the solution of multidisciplinary problems characterized by time-dependent phenomena such

as those encountered in aeroelasticity or noise reduction [12], for example.

Given the computational cost of accurately obtaining an unsteady solution and thus its adjoint, sufficiently accurate reduced order methods [13] must be used with each primal flow solver, if the objective is to solve design problems routinely. Among others, the Harmonic Balance method (HB) is a promising option for applications involving quasi-periodic flows characterized by a finite amount of dominant frequencies that need not be harmonics of each other [14–16].

Considerable development has been dedicated to HB methods for turbomachinery applications, whereby the flow spectrum is dominated by the blade passing frequencies [15]. One technique that is a subset of the harmonic balance method, sometimes referred to as the Time Spectral method [14, 15, 17], has been originally formulated for periodic flow problems, and associated adjoints have been derived [18–21].

HB adjoint-based optimization opens up the possibility to deal with problems featuring flow frequencies that are not harmonically related, thus without the restriction of resolving harmonics of a single fundamental flow frequency. Currently available methods in the literature are limited to inviscid flow problems or frozen turbulence assumptions during design [22, 23], which can have a strong impact on the final optimization result [24]. In this work, a fully-turbulent HB adjoint-based shape optimization method is proposed and implemented within the *SU2* open-source software environment [25, 26]. The algorithm is based on the duality-preserving approach [27–30], which allows the adjoint solver to inherit the same convergence properties of the primal flow solver. The chosen algorithm ensures robust convergence of the numerical solution of the turbulent adjoint equations, without the assumption of constant eddy viscosity, for all the resolved harmonics.

The method is described in detail first, followed by the illustration of two application cases. An airfoil pitching at a rate characterized by two frequencies that are not harmonically related is first considered, followed by a turbine cascade subject to unsteady inlet conditions.

2.2 Method

2.2.1 Time Discretization

The semi-discrete form of the Navier-Stokes equations, for a generic cell volume Ω , is

$$\Omega \frac{\partial \mathbf{U}}{\partial t} + \mathcal{R}(\mathbf{U}) = 0, t > 0. \quad (2.1)$$

$\mathbf{U} = (\rho, \rho v_1, \rho v_2, \rho v_3, \rho E)$ is the vector of conservative variables, with ρ the density, \mathbf{v} the velocity vector, and E the total specific energy. Ω and its boundary $\partial\Omega$ are assumed to vary their position in time, with velocity \mathbf{u}_Ω , without deforming. \mathcal{R} is the residual operator for the spatial integration of the convective and viscous fluxes, i.e., \mathbf{F}^c and \mathbf{F}^v . Using an

Arbitrary Lagrangian-Eulerian (ALE) formulation [31] ,

$$\begin{aligned}\mathcal{R}(\mathbf{U}) &= f(\mathbf{F}^c, \mathbf{F}^v) && \text{in } \Omega, t > 0 \\ \mathbf{v} &= \mathbf{u}_\Omega && \text{on } \partial\Omega, t > 0\end{aligned}\quad (2.2)$$

with

$$\mathbf{F}^c = \begin{pmatrix} \rho(\mathbf{v} - \mathbf{u}_\Omega) \\ \rho\mathbf{v} \times (\mathbf{v} - \mathbf{u}_\Omega) + p\bar{\mathbf{I}} \\ \rho E(\mathbf{v} - \mathbf{u}_\Omega) + p\mathbf{v} \end{pmatrix}, \quad (2.3)$$

where p is the static pressure. The viscous fluxes are given by

$$\mathbf{F}^v = \begin{pmatrix} \cdot \\ \mu\dot{\bar{\tau}} \\ \mu\bar{\tau} \cdot \mathbf{v} + \kappa\nabla T \end{pmatrix}. \quad (2.4)$$

where T is the static temperature, κ the thermal conductivity, μ the dynamic viscosity and $\bar{\tau}$ the viscous stress tensor

$$\bar{\tau} = \nabla\mathbf{v} + \nabla\mathbf{v}^\top - \frac{2}{3}\bar{\mathbf{I}}(\nabla \cdot \mathbf{v}). \quad (2.5)$$

The turbulence modeling is considered, according to the Boussinesq hypothesis, by defining $\mu = \mu_l + \mu_t$, and $\kappa = \kappa_l + \kappa_t$. μ_l and μ_t are the laminar and turbulent dynamic viscosities, whereas κ_l and κ_t are the laminar and turbulent thermal conductivities. More in general, for RANS equations, the vector of the conservative variables \mathbf{U} can be redefined as

$$\mathbf{U} := \begin{pmatrix} \mathbf{U}_l \\ \mathbf{U}_t \end{pmatrix}, \quad \mathcal{R}(\mathbf{U}) = \mathcal{R}(\mathbf{U}_f, \mathbf{U}_t) := \begin{pmatrix} \mathcal{R}_f(\mathbf{U}_l, \mathbf{U}_t) \\ \mathcal{R}_t(\mathbf{U}_l, \mathbf{U}_t) \end{pmatrix}, \quad (2.6)$$

in which $\mathbf{U}_l = (\rho, \rho v_1, \rho v_2, \rho v_3, \rho E)$ and \mathbf{U}_t is the vector of the conservative variables associated to the selected turbulence model. For example, in case of the Menter Shear Stress Transport (SST) model [32], $\mathbf{U}_t = (\rho\kappa, \rho\omega)$ with κ the turbulent kinetic energy and ω the specific dissipation. The application of time-discretization to (2.1), using an implicit Euler scheme, leads to

$$\Omega\mathcal{D}_t(\mathbf{U}^{q+1}) + \mathcal{R}(\mathbf{U}^{q+1}) = 0, \quad (2.7)$$

where q is the physical time step index, and \mathcal{D}_t is the time-derivative operator. For a dual time stepping approach [33, 34] with pseudo-time τ , one would obtain the following discretization

$$\Omega\frac{\Delta\mathbf{U}^{q+1}}{\Delta\tau} + \Omega\mathcal{D}_t(\mathbf{U}^{q+1}) + \mathcal{R}(\mathbf{U}^{q+1}) = 0. \quad (2.8)$$

where the additional term is used to relax the solution at each physical time step.

2.2.2 Harmonic Balance Operator

As given in Ref. [15], the Fourier coefficients resulting from the application of the discrete Fourier transform (DFT) are

$$\hat{\mathbf{u}}_k = \frac{1}{N} \sum_{n=0}^{N-1} \tilde{\mathbf{U}}_n e^{-i\omega_k t_n}, \quad (2.9)$$

where $\tilde{\mathbf{U}} = [\mathbf{U}_0, \mathbf{U}_1, \dots, \mathbf{U}_{N-1}]$, is the vector of the conservative variables evaluated at N time instances

$$\mathbf{t} = [t_0, t_1, \dots, t_{N-1}]. \quad (2.10)$$

Hence the corresponding Fourier coefficients are

$$\hat{\mathbf{u}} = [\mathbf{u}_0, \mathbf{u}_1, \dots, \mathbf{u}_{K-1}], \quad (2.11)$$

with $N = 2K + 1$, $\omega_k = 2\pi f_k$ and K being the number of frequencies. An odd number of time instances is used in this work in order to prevent numerical instabilities [35]. The ensemble of the K resolved frequencies is denoted by $\boldsymbol{\omega} = [0, \omega_1, \dots, \omega_K, \omega_{-K}, \dots, \omega_{-1}]$. By defining the DFT matrix as

$$E_{k,n} = \frac{1}{N} e^{-i\omega_k t_n}, \quad n, k \in [0, N], \quad (2.12)$$

and its inverse discrete Fourier transform (IDFT)

$$E_{n,k}^{-1} = e^{i\omega_k t_n}, \quad n, k \in [0, N], \quad (2.13)$$

one can calculate the Fourier coefficients as

$$\hat{\mathbf{u}} = \mathbf{E} \tilde{\mathbf{U}}, \quad (2.14)$$

with the corresponding vector of conservative variables

$$\tilde{\mathbf{U}} = \mathbf{E}^{-1} \hat{\mathbf{u}}. \quad (2.15)$$

If the frequencies f_k (and hence ω_k) are not multiples of f_1 , once the DFT matrix from (2.12) or the IDFT matrix from (2.13) are constructed, it is not possible to obtain an analytical expression for the corresponding inverse matrix. The IDFT can be obtained by means of numerical matrix inversion methods.

The time operator of (2.7) can be approximated using spectral interpolation. Applying the spectral operator to the vector of conservative variables $\tilde{\mathbf{U}}$, evaluated at N time instances, yields

$$\mathcal{D}_t(\mathbf{U}) \approx \mathcal{D}_t(\tilde{\mathbf{U}}). \quad (2.16)$$

Given that $\hat{\mathbf{u}}$ is independent from time, using (2.15) and (2.14), one can write

$$\mathcal{D}_t(\tilde{\mathbf{U}}) = \mathcal{D}_t(\mathbf{E}^{-1}\hat{\mathbf{u}}) = \frac{\partial \mathbf{E}^{-1}}{\partial t}\hat{\mathbf{u}} = \frac{\partial \mathbf{E}^{-1}}{\partial t}\mathbf{E}\tilde{\mathbf{U}}. \quad (2.17)$$

From (2.13)

$$\frac{\partial \mathbf{E}^{-1}}{\partial t} = \mathbf{E}^{-1}\mathbf{D}, \quad (2.18)$$

where

$$\mathbf{D}_{k,n} = i\omega_k \delta_{k,n}. \quad (2.19)$$

\mathbf{D} is the diagonal matrix given by

$$\mathbf{D} = \text{diag}(0, i\omega_1, \dots, i\omega_K, i\omega_{-K}, \dots, i\omega_{-1}). \quad (2.20)$$

One can combine (2.17) with (2.18) and define the spectral operator matrix \mathbf{H} as

$$\mathbf{H} = \mathbf{E}^{-1}\mathbf{D}\mathbf{E}. \quad (2.21)$$

Here, \mathbf{E}^{-1} is given analytically by (2.13), and \mathbf{E} is computed by inverting \mathbf{E}^{-1} using Gaussian elimination. It eventually follows that

$$\mathcal{D}_t(\tilde{\mathbf{U}}) = \mathbf{H}\tilde{\mathbf{U}}. \quad (2.22)$$

2.2.3 Time-domain harmonic balance

Considering $\tilde{\mathbf{U}}$, the set of the conservative variables evaluated at N time instances, one can write (2.8) for a single time instance n as

$$\Omega \frac{\Delta \mathbf{U}_n^{q+1}}{\Delta \tau} + \Omega \mathcal{D}_t(\mathbf{U}_n^{q+1}) + \mathcal{R}(\mathbf{U}_n^{q+1}) = 0. \quad (2.23)$$

Linearization of the residual yields

$$\mathcal{R}(\mathbf{U}_n^{q+1}) = \mathcal{R}(\mathbf{U}_n^q) + \frac{\partial \mathcal{R}(\mathbf{U}_n^q)}{\partial \mathbf{U}_n^q} \Delta \mathbf{U}_n = \mathcal{R}(\mathbf{U}_n^q) + \mathbf{J} \Delta \mathbf{U}_n. \quad (2.24)$$

From (2.22), \mathcal{D}_t is a linear operator, so the following manipulations are possible:

$$\mathcal{D}_t(\Delta \mathbf{U}_n) = \mathcal{D}_t(\mathbf{U}_n^{q+1} - \mathbf{U}_n^q) = \mathcal{D}_t(\mathbf{U}_n^{q+1}) - \mathcal{D}_t(\mathbf{U}_n^q), \quad (2.25)$$

and

$$\mathcal{D}_t(\mathbf{U}_n^{q+1}) = \sum_{k=0}^{N-1} H_{n,k} \Delta \mathbf{U}_k + \sum_{k=0}^{N-1} H_{n,k} \mathbf{U}_k^q. \quad (2.26)$$

Substitution of the linearized expressions transforms (2.23) into

$$\left(\frac{\Omega I}{\Delta\tau} + J + \Omega H_{n,n} \right) \Delta U_n + \mathcal{R}(U_n^q) = -\Omega \sum_{k=0}^{N-1} (1 - \delta_{n,k}) H_{n,k} \Delta U_k - \Omega \sum_{k=0}^{N-1} H_{n,k} U_k^q. \quad (2.27)$$

In this work, a semi-implicit approach is used to solve (2.27) as

$$\left(\frac{\Omega I}{\Delta\tau} + J \right) \Delta U_n = \widehat{\mathcal{R}}_n(\hat{U}^q), \quad (2.28)$$

where

$$\widehat{\mathcal{R}}_n(U^q) = -\mathcal{R}(U_n^q) - \Omega \sum_{k=0}^{N-1} H_{n,k} \Delta U_k - \Omega \sum_{k=0}^{N-1} H_{n,k} U_k^q. \quad (2.29)$$

Equation (2.28) is solved for each time instance in a segregated manner. Therefore, an unsteady flow problem characterized by K frequencies requires that the solution of $2K+1$ nonlinear systems of equations need to be computed. The current harmonic balance approach is implemented in the open-source *SU2* code [25, 26].

2.2.4 Governing equations of the adjoint solver

The adjoint equations are now derived for the proposed Harmonic Balance formulation described in Sec. 2.2.3 for both laminar and turbulent flows.

Equation (2.28) is reformulated in terms of a fixed-point iteration for each U_n as

$$U_n^{q+1} = \mathcal{G}_n(U^q), \quad (2.30)$$

where \mathcal{G}_n is the iteration operator of the pseudo time-stepping at time instance n . If \mathcal{G}_n is contractive, i.e., $\|\frac{\partial \mathcal{G}_n}{\partial U_n}\| < 1$, according to the Banach fixed-point theorem [36], (2.30) admits a unique fixed-point solution U_n^* such that

$$\widehat{\mathcal{R}}_n(U^*) = 0 \iff U_n^* = \mathcal{G}_n(U^*). \quad (2.31)$$

The aerodynamic design problem, including a possible explicit dependence of the objective function \mathcal{J} on the vector of the design variables α , can be expressed as

$$\begin{aligned} & \underset{\alpha}{\text{minimize}} \quad \mathcal{J}(U(\alpha), X(\alpha)) \\ & \text{subject to} \quad U_n(\alpha) = \mathcal{G}_n(U(\alpha), X_n(\alpha)), \quad n = 1, 2, \dots, N \\ & \quad X_n(\alpha) = M_n(\alpha). \end{aligned} \quad (2.32)$$

X_n are the physical grids constructed for each time instance, and $M_n(\alpha)$ is a differentiable function representing the mesh deformation algorithm. The objective function \mathcal{J} is obtained as the spectral average, using (2.43), over the resolved time instances

$$\mathcal{J} = f(\mathcal{J}(U_1, X_1), \mathcal{J}(U_2, X_2), \dots, \mathcal{J}(U_N, X_N)). \quad (2.33)$$

The Lagrangian of the constrained optimization problem is given by

$$\mathcal{L} = \mathcal{J} + \sum_{n=1}^N \{(\mathcal{G}_n(\mathbf{U}(\alpha), \mathbf{X}_n(\alpha)) - \mathbf{U}_n(\alpha)^\top \boldsymbol{\lambda}_n + (\mathbf{M}_n(\alpha) - \mathbf{X}_n(\alpha))^\top \boldsymbol{\mu}_n\}, \quad (2.34)$$

with $\boldsymbol{\lambda}$ and $\boldsymbol{\mu}$ being the adjoint variables. Given the constraint equations in (2.32)

$$\begin{aligned} \mathbf{U}_n(\alpha) - \mathcal{G}_n(\mathbf{U}(\alpha), \mathbf{X}_n(\alpha)) &= 0, \quad n = 0, 1, \dots, N-1 \\ \mathbf{X}_n(\alpha) - \mathbf{M}_n(\alpha) &= 0, \end{aligned} \quad (2.35)$$

and omitting in the notation the explicit dependence from the independent variables, one can express the differential of the Lagrangian as

$$\begin{aligned} d\mathcal{L} = \sum_{n=0}^{N-1} &\left(\frac{\partial \mathcal{J}}{\partial \mathbf{U}_n}^\top + \sum_{k=0}^{N-1} \frac{\partial \mathcal{G}_k}{\partial \mathbf{U}_n}^\top \boldsymbol{\lambda}_k - \boldsymbol{\lambda}_n \right) d\mathbf{U}_n + \\ &\sum_{n=0}^{N-1} \left(\frac{\partial \mathcal{J}}{\partial \mathbf{X}_n}^\top + \frac{\partial \mathcal{G}_n}{\partial \mathbf{X}_n}^\top \boldsymbol{\lambda}_n - \boldsymbol{\mu}_n \right) d\mathbf{X}_n + \\ &\sum_{n=0}^{N-1} \frac{\partial \mathbf{M}_n}{\partial \alpha}^\top \boldsymbol{\mu}_n d\alpha, \end{aligned} \quad (2.36)$$

from which the adjoint equations can be obtained as

$$\frac{\partial \mathcal{J}}{\partial \mathbf{U}_n}^\top + \sum_{k=0}^{N-1} \frac{\partial \mathcal{G}_k}{\partial \mathbf{U}_n}^\top \boldsymbol{\lambda}_k = \boldsymbol{\lambda}_n, \quad (2.37)$$

and

$$\frac{\partial \mathcal{J}}{\partial \mathbf{X}_n}^\top + \frac{\partial \mathcal{G}_n}{\partial \mathbf{X}_n}^\top \boldsymbol{\lambda}_n = \boldsymbol{\mu}_n. \quad (2.38)$$

Equation (2.38) can be solved directly once the solution of (2.37) is known. Similar to the flow solver, (2.37) can be seen as a fixed-point iteration in $\boldsymbol{\lambda}_n$, namely

$$\boldsymbol{\lambda}_n^{q+1} = \frac{\partial \mathcal{N}}{\partial \mathbf{U}_n}(\mathbf{U}_n^*, \boldsymbol{\lambda}^q, \mathbf{X}_n), \quad (2.39)$$

where \mathbf{U}_n^* is the numerical solution for the flow equation (2.31) and \mathcal{N} is the shifted Lagrangian defined as

$$\mathcal{N} = \mathcal{J} + \sum_{n=1}^N \mathcal{G}_n^\top(\mathbf{U}, \mathbf{X}_n) \boldsymbol{\lambda}_n. \quad (2.40)$$

Since \mathcal{G}_n is contractive, $\frac{\partial \mathcal{N}}{\partial \mathbf{U}_n}$ is also contractive because

$$\left\| \frac{\partial}{\partial \boldsymbol{\lambda}_n} \left(\frac{\partial \mathcal{N}}{\partial \hat{\mathbf{U}}_n} \right) \right\| = \left\| \frac{\partial \mathcal{G}_n}{\partial \hat{\mathbf{U}}_n}^\top \right\| = \left\| \frac{\partial \mathcal{G}_n}{\partial \hat{\mathbf{U}}_n} \right\| < 1. \quad (2.41)$$

Therefore, according to the fixed-point theorem, (2.39) will converge at the same rate as the primal flow solver.

The right hand side of equation (2.39) is obtained using Algorithmic Differentiation applied to the underlying source code of the program that computes \mathcal{G}_n . The AD tool adopted [37] makes use of the *Jacobi taping method* in combination with the *Expression Templates* feature of C++, leading only to a small runtime overhead.

Finally, the gradient of the objective function \mathcal{J} with respect to the vector of the design variables α can be computed from the converged flow and adjoint solutions using

$$\frac{d\mathcal{L}^\top}{d\alpha} = \frac{d\mathcal{J}^\top}{d\alpha} = \frac{\partial M_n^\top(\alpha)}{\partial \alpha} \boldsymbol{\mu}_n. \quad (2.42)$$

2.3 Results

The proposed HB-based adjoint method has been applied to two test cases: the fluid dynamic shape optimization of both a pitching airfoil and a turbine cascade. For both cases, a harmonic balance flow solution has been first obtained and verified against a fully-unsteady simulation using a second-order dual time stepping method [34]. For the spatial discretization, second-order accuracy has been obtained for the convective fluxes using a centered scheme or the MUSCL approach [38] and for the viscous fluxes using a corrected average-of-gradients method. The reader is referred to Ref. [26] for details on the numerical methods and tools available in *SU2*.

The results obtained with the HB solver at N time instances for a generic quantity of interest Γ are interpolated to a larger time vector t^* of length N^* using

$$\Gamma^* = \mathbf{E}^{*-1} (\mathbf{E} \Gamma), \quad (2.43)$$

where \mathbf{E}^{*-1} is the larger interpolated IDFT matrix of size $N^* \times N$ given by $E_{n,k}^{*-1} = e^{i\omega_k t_n^*}$, and \mathbf{E}^{-1} is the $N \times N$ IDFT matrix.

The constrained shape optimization problem is solved once the gradient is obtained from the adjoint solution, using a modified version of the nonlinear least-squares method (SLSQP) [39]. Accurate gradient values are obtained by leveraging Algorithmic Differentiation (AD). The reverse mode of the open-source AD tool *CoDiPack* [29, 40] is used in this work to linearize the primal solver.

2.3.1 NACA64A010 pitching airfoil

A two-dimensional pitching NACA 64A010 airfoil in inviscid flow is considered first. The rigid body motion is imposed by assigning a time-varying angle of attack computed as

$$\alpha = 1.01[\sin(\omega t) + \sin(2.6 \omega t)]. \quad (2.44)$$

The flow is transonic with shocks appearing along the upper and lower surfaces of the airfoil while pitching, as can be observed in Figs. 2.5a, 2.5b and 2.5c. The convective fluxes

are computed with the JST scheme [33]. The mesh is composed entirely of triangular elements. It contains approximately 11 000 grid points with 200 points along the airfoil and 100 points on the far-field boundary. The main simulation parameters are summarized in Tab. 2.1.

Table 2.1: Simulation parameters of the pitching NACA64A010 airfoil test case. The reduced frequency ω^* is based on the semi-chord length.

	Symbol	Value	Units
Free-stream temperature	T_∞	288.15	[K]
Mach number	Ma_∞	0.78	[$-$]
Reduced frequencies	$[\omega_1^*, \omega_2^*]$	[0.197, 0.512]	[$-$]

A reference time-accurate simulation was performed with 160 time steps per smallest period (corresponding to $2.6\omega_1$) in order to get a well-resolved solution in time. Fig. 2.1a and 2.1b show the mesh close to the airfoil and the frequency spectrum of the drag coefficient. Fig. 2.1b shows that the overall dominant frequencies are the pitching frequencies ω , 2.6ω and their linear combinations. This analysis is performed to select the relevant frequencies for the HB computation.

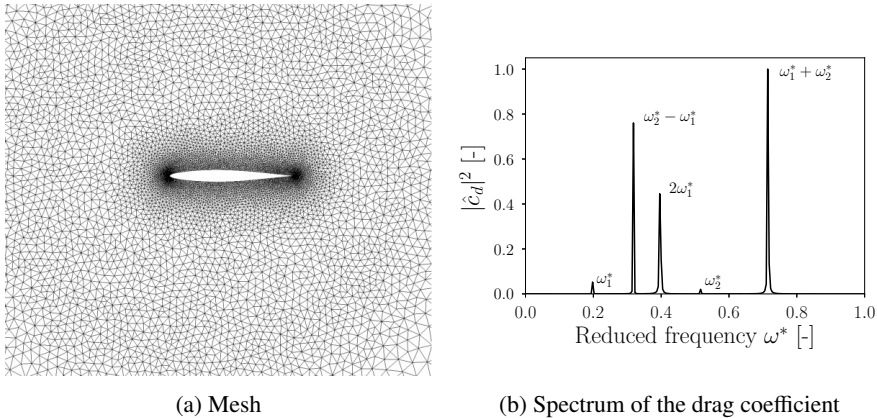


Figure 2.1: NACA 64A010 airfoil mesh at $t = 0$ and spectrum of the drag coefficient.

The test case is then simulated using the harmonic balance method with several choices for the number of time instances with the two input frequencies as pitching frequencies. Fig. 2.2 shows the convergence of the harmonic balance solution to the fully-unsteady solution with an increase in the number of input frequencies. The converged solution for the selected time instances of both the lift and the drag coefficient is interpolated using (2.43). According to the spectrum of the drag coefficient (Fig. 2.1b), the selected input frequencies are reported in Tab. 2.2.

In the context of quasi-periodic flows, the definition of *pseudo-period* is introduced to

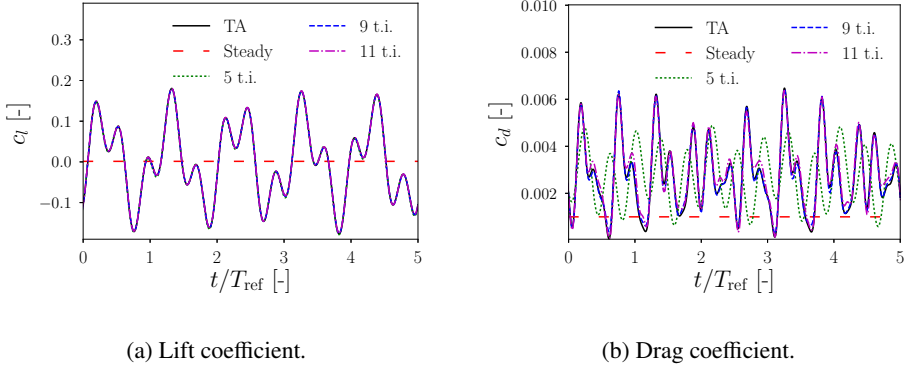


Figure 2.2: Lift coefficient c_l and drag coefficient c_d : HB solution obtained for different time instances vs time accurate solution. T_{ref} is the reference time interval corresponding to the highest frequency.

Table 2.2: Optimal time period ratio T_{opt}/T_0 and input frequencies for the pitching airfoil test case, with $\omega_2 = 2.6\omega_1$. T_0 is the period corresponding to the lowest frequency value.

Time instances	T_{opt}/T_0	Input frequencies
5	1.13	$0, \pm\omega_1, \pm\omega_2$
7	1.00	$0, \pm\omega_1, \pm\omega_2, \pm 2\omega_1$
9	1.41	$0, \pm\omega_1, \pm(\omega_2 - \omega_1), \pm\omega_2, \pm(\omega_2 + \omega_1)$
11	1.38	$0, \pm\omega_1, \pm(\omega_2 - \omega_1), \pm 2\omega_1, \pm\omega_2, \pm(\omega_2 + \omega_1)$

indicate the time interval $T = [t_0, t_{N-1}]$, with t defined in (2.10).

In order to ensure convergence for any set of frequencies, an optimal time pseudo-period is selected using the algorithm proposed in Ref. [41]. A uniform time sampling within the pseudo-period T is adopted, and the values of the optimal time period are reported in Tab. 2.2.

Overall, the agreement of the lift coefficient is excellent, resulting in a root-mean-square-error (RMSE) of 0.00275 with just two input frequencies, due to the fact that the movement of the airfoil is primarily in the direction of the lift (Fig. 2.2a). Conversely, in the case of drag, a larger number of input frequencies is required to capture the fully-unsteady result due to the dominant non-linearities in the flow (shocks). Hence, more than five time instances are necessary for the accurate determination of the drag coefficient, as can be seen in Fig. 2.2b. Since the selected objective function is the drag coefficient, a suitable number of input frequencies should be identified. The time-averaged drag coefficient is 0.0027 for 5 time instances, 0.0028 for 9, 11 and 13 time instances compared to 0.0028 for the time-accurate unsteady solution. It can be inferred that 9 time instances are sufficient for shape optimization. Fig. 2.2 reports also the steady-state values of Cl and Cd obtained with $\alpha = 0$.

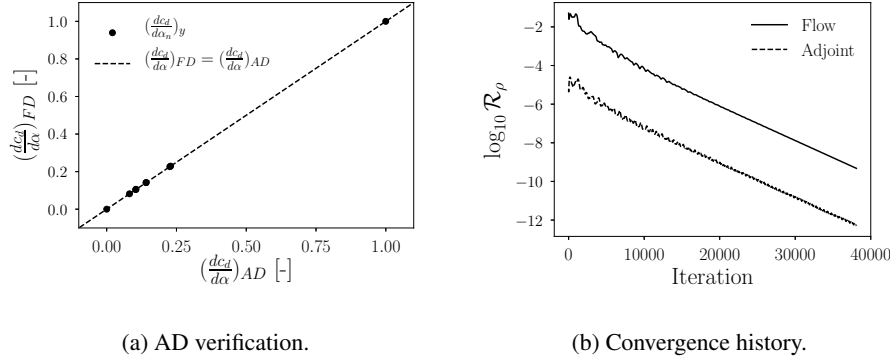


Figure 2.3: Comparison between the normalized gradients of the objective function calculated with the reverse mode of the AD and the second order central finite difference (a); flow and adjoint solver convergence history of the density residual relative to the first time instance (b).

After the analysis of the flow solution, the adjoint-based shape optimization problem is considered. The time-averaged drag coefficient c_d is minimized over the pseudo-period. Equality constraints on the lift coefficient (c_l) and the maximum thickness (θ_{max}) are imposed. The resulting optimization problem is set as follows

$$\begin{aligned} & \underset{\alpha}{\text{minimize}} \quad c_d(\mathbf{U}_n, \mathbf{X}_n, \alpha) \\ & \text{subject to: } c_l = c_{l_0}, \\ & \quad \delta_{\max} = \delta_{\max_0}, \\ & \quad \mathbf{U}_n = \mathcal{G}_n, \quad n = 1, 2, \dots N \\ & \quad \mathbf{X}_n = M_n. \end{aligned} \tag{2.45}$$

50 Hicks-Henne bump function variables [42] distributed uniformly over the upper and lower surfaces of the airfoil are chosen as the design variables.

The gradients of the discrete adjoint are first compared with the gradients obtained with a second-order accurate finite difference (FD) method. This verification is performed over a set of 8 Hicks-Henne bump functions with the first 4 located on the suction side of the airfoil and the others on the pressure side. Fig. 2.3a depicts the comparison between the adjoint-based gradients and the FD gradients. Fig. 2.3b shows the convergence of both the flow and the adjoint solver as a function of the number of iterations. As discussed in Sec. 2.2.4, the convergence rate of the adjoint solver is inherited from the primal flow solver. The computational time ratio between the adjoint solution and the flow solution is about 1.3. The average computational time for one iteration of the primal solver was approximately 0.28 seconds, using the 4 cores *Intel Xeon E5-1620 Processor* with hyper-threading.

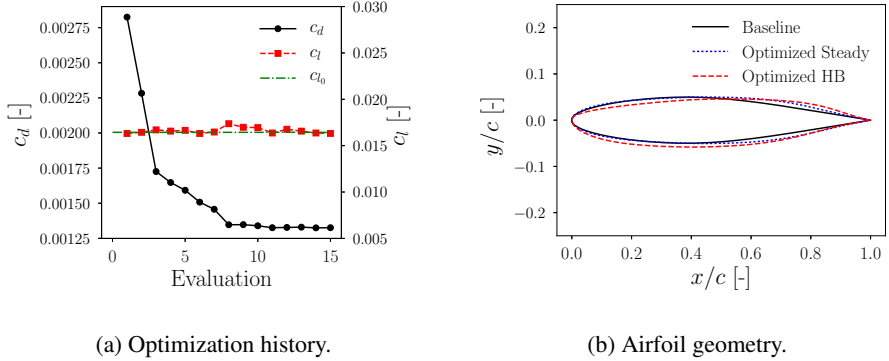


Figure 2.4: Shape optimization convergence history of the drag coefficient (a); baseline vs optimized airfoil (b).

Fig. 2.4a reports the reduction in drag coefficient with the number of optimizer iterations as well as the lift coefficient constraint. The shape optimization process (Fig. 2.4) achieves a decrease in drag coefficient of about 50%, while maintaining the lift coefficient and the maximum thickness within 1% of the constraint value.

The Mach contours of the baseline airfoil compared with the contours of the optimized airfoil at different time instances are reported in Fig. 2.5. The optimized airfoil shape leads to an attenuation of the strong shocks characterizing the baseline configuration, resulting in drag reduction.

Finally, the unsteady optimization results are compared with those obtained from a similar constrained steady state optimization of the airfoil at $\alpha = 0$. The final shape given by the unsteady design method differs from the steady one and it is shown in Fig. 2.4b. Furthermore, when the steady-optimized airfoil undergoes the pitching motion prescribed by the test case, the reduction of the time-averaged drag coefficient is 44%, whereas it was reduced by more, i.e. 50%, for the unsteady optimization. This shows that the inclusion of unsteadiness is worthwhile in this case.

2.3.2 T106D-EIZ Turbine Cascade

The aim of this test case is to assess the capability of the HB-based design method for fully-turbulent flows. In the experimental setup [43], the unsteadiness in the wake of an upstream blade row is approximated by a moving bar, as depicted in Fig. 2.6a. The moving bars are located at $x_b/l = 0.7$ upstream of the cascade inlet plane, having a velocity $v_b = 21.4$ m/s parallel to the inlet. A schematic representation is shown in Fig. 2.6a, and the main operating conditions for the test case are reported in Tab. 2.3.

The two-dimensional flow domain is discretized with approximately 40 000 elements (Fig. 2.6b), and the Roe scheme is selected for the convective flux discretization. A suitable spacing of quadrilateral elements is used to cluster the near wall cells such that y^+ is

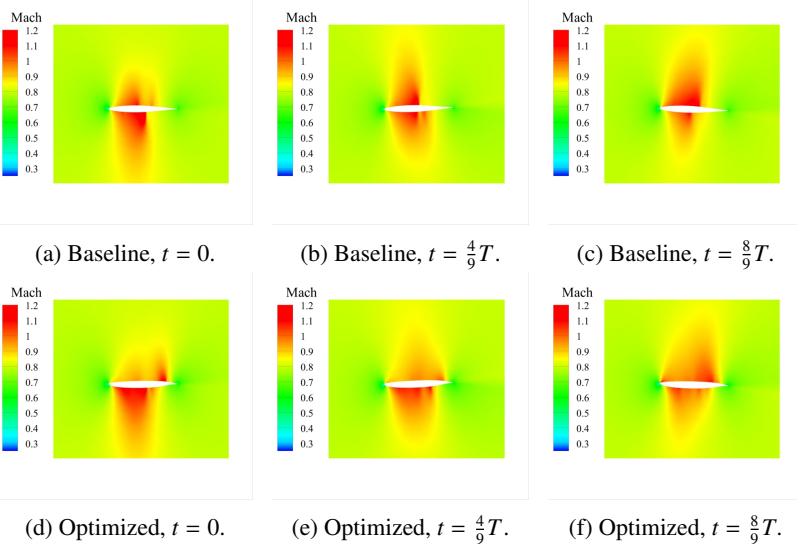


Figure 2.5: Pitching airfoil Mach number contours calculated at three different time instances with the HB method, for both the baseline (a, b, c) and the optimized (d, e, f) profile.

less than 1. This test case is a benchmark for the study of laminar-to-turbulent transition. However, since the present work aims to assess the methodology for design optimization only, the computations are performed assuming fully-turbulent conditions, employing the SST turbulence model [32].

In order to calculate the cascade performance, the total pressure loss coefficient is evaluated as

$$\zeta_P = \frac{\langle P_{tot,1} \rangle_{\partial\Omega_1} - \langle P_{tot,2} \rangle_{\partial\Omega_2}}{\langle P_{tot,2} \rangle_{\partial\Omega_2} - \langle P_2 \rangle_{\partial\Omega_2}}, \quad (2.46)$$

where $\langle P_{tot,1} \rangle_{\partial\Omega_1}$ and $\langle P_{tot,2} \rangle_{\partial\Omega_2}$ are the inlet and outlet total pressure averaged over their corresponding boundary, respectively. $\langle P_2 \rangle_{\partial\Omega_2}$ is the average static pressure at the cascade outlet. The averages at the boundaries are calculated using a mixed-out averaging procedure [44].

First, a validation is performed using the experimental data [43] of the turbine cascade operating at steady state (Fig. 2.7). The simulation results are in agreement with the experimental data except for the separation bubble in the suction side. As expected, the main deviation between CFD and experiments occurs at about $x/l = 0.75$, possibly due to transition not being accurately modeled.

For this test case, two configurations are considered for design: i) a spatially non-uniform, time-dependent inlet boundary condition; ii) a spatially uniform, time-dependent inlet boundary condition. The terminology OptC1 and OptC2 is used to refer to the first

Table 2.3: Simulation parameters of the T106D-EIZ test case, as described in [43]. Re_2 is the Reynolds number based on the exit velocity and density; Ma_2 the exit Mach number; Tu_1 the inlet turbulence intensity.

	Symbol	Value	Units
Exit Reynolds number	Re_2	200 000	[$-$]
Exit Mach number	Ma_2	0.593	[$-$]
Bars speed	v_b	21.4	[m/s]
Background turbulence level	Tu_1	2.5	[$\%$]
Eddy viscosity ratio	μ_t/μ	100	[$-$]

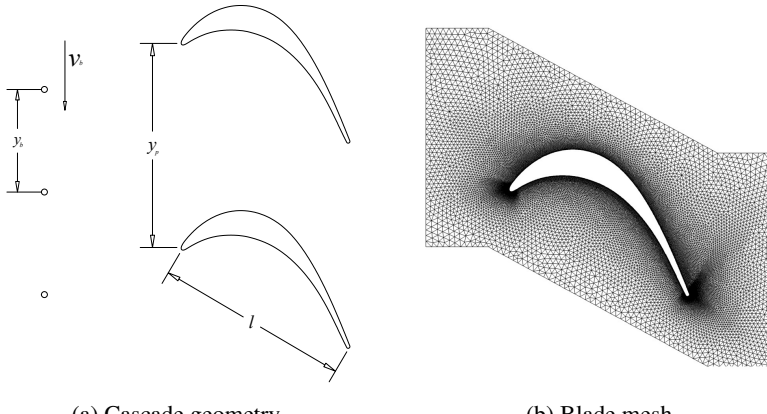


Figure 2.6: Schematic geometry of the T106D-EIZ turbine cascade [43] and blade mesh.

and the second shape optimization problem, respectively.

2.3.2.1 OptC1 configuration

In this configuration, an inlet boundary condition is imposed in order to reproduce the wakes generated by the moving bars. The imposed values of the total pressure, temperature, and flow direction at the boundary are interpolated from the results of a steady state simulation of the flow past the bars. With this boundary condition, only multiples of the blade passing frequency are expected. The fundamental blade passing frequency, given a ratio between the blade pitch and the bar pitch $y_p/y_b = 3$, is defined as

$$f_1 = 3 \frac{v_b}{y_p} . \quad (2.47)$$

To verify the HB solution, a second-order time-accurate URANS simulation using the dual time stepping method is performed with a time-step 150x smaller than the lowest period ($1/f_1$). The total pressure loss coefficient from this simulation is compared in

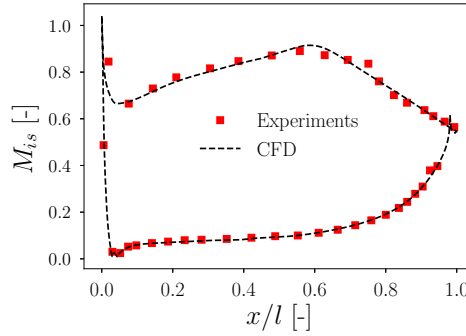


Figure 2.7: Validation of steady state simulation results with experimental data [43].

Fig. 2.8a with the HB solution obtained with 3, 5, and 7 time instances. The selected time instances correspond to the solution for the frequency vectors $\omega_{N3} = [0, \pm \omega_0]$, $\omega_{N5} = [0, \pm \omega_0, \pm 2\omega_0]$ and $\omega_{N7} = [0, \pm \omega_0, \pm 2\omega_0, \pm 3\omega_0]$. The resolved frequencies are, therefore, multiples of the fundamental blade passing frequency only. The total pressure loss coefficient, defined in (2.46), and shown in Fig. 2.8a as function of time, is obtained by spectral interpolation of the harmonic balance results using (2.43). The RMSE of the total pressure loss coefficient for the solution obtained with 5 time instances is equal to 0.010. The harmonic balance solution obtained with 5 time instances is about 9x faster than the time-accurate solution calculated over a total simulation time of five periods, which includes the initial transient before reaching convergence to a periodic flow field solution. 5 time instances are used for shape optimization, as a trade-off between accuracy and computational cost.

In Figs. 2.11a, 2.11b, and 2.11c, the Mach number contours from the HB simulation are reported for 3 different time instances with the simulation period given by $T = 1/f_1$. The results show the bar wakes entering the cascade and a separation area occurring at about $x/l = 0.7$.

Next, the shape optimization problem of the cascade configuration is considered. It can be expressed as

$$\begin{aligned}
 & \underset{\alpha}{\text{minimize}} \quad \zeta_P(\mathbf{U}_n, \mathbf{X}_n, \alpha) \\
 & \text{subject to: } \alpha_{out} < \alpha_{out_0} + 4^\circ, \\
 & \quad \delta_t = \delta_{t_0}, \\
 & \quad \mathbf{U}_n = \mathcal{G}_n, \quad n = 1, 2, \dots N \\
 & \quad \mathbf{X}_n = \mathbf{M}_n.
 \end{aligned} \tag{2.48}$$

where the time-averaged total pressure loss coefficient ζ_P , obtained from (2.43), is selected as objective function. Inequality constraints on the absolute exit flow angle (α_{out})

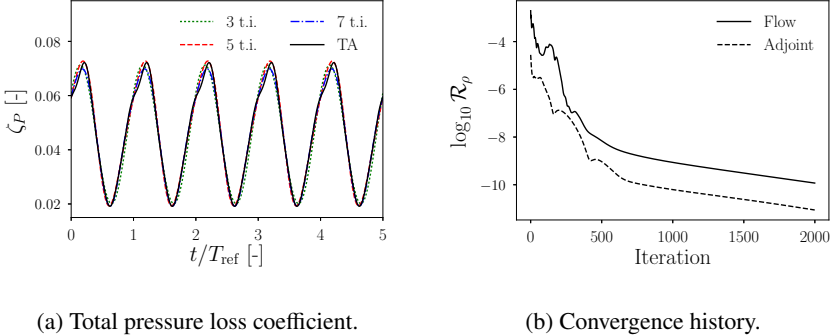


Figure 2.8: Comparison of the total pressure loss coefficient ζ_P as function of time, obtained with time accurate and HB simulations (a); convergence history of the first time instance density residual (b).

and trailing edge thickness (δ_t) are imposed. The optimization is performed using an ensemble of 16 geometrical design parameters α based on a free-form deformation (FFD) approach [45]. The gradients of the objective function are again obtained with the proposed adjoint technique and compared with the same gradients obtained by second-order central finite differences (FD). The results of this comparison are reported in Fig. 2.9a, showing excellent agreement between AD and FD gradients (RMSE = $2 \cdot 10^{-5}$). The ratio between the computational time of the adjoint solution and the primal flow solution is approximately 1.7. The average primal solver CPU time per iteration was about 1.41 seconds on a 4 cores *Intel Xeon E5-1620 Processor* with hyper-threading.

Fig. 2.10 shows that the convergence of the optimization to the minimum objective is nearly reached after only 7 evaluations, although satisfying the constraint requires more evaluations. Fig. 2.10b highlights that the performance of the optimized blade is significantly improved, as the total pressure loss coefficient is approximately 38% lower, while the constraint on the absolute outlet flow angle is satisfied. The separation area, as seen in Fig. 2.11, is considerably smaller with the optimized blade shape. The unsteady optimization leads to a decrease in the peak of the total pressure loss coefficient of 44% and a reduction of 54% of the signal amplitude (Fig. 2.12a). Furthermore, the objective function spectrum obtained from a URANS simulation of the optimized blade (Fig. 2.12b) does not contain additional frequencies when compared with the baseline configuration.

2.3.2.2 OpcC2 configuration

In order to investigate the capabilities of the HB-based design method to deal with problems characterized by frequencies that are not multiples of one fundamental harmonic, a second configuration of the *T106D-E1Z* cascade is considered. In analogy with previous

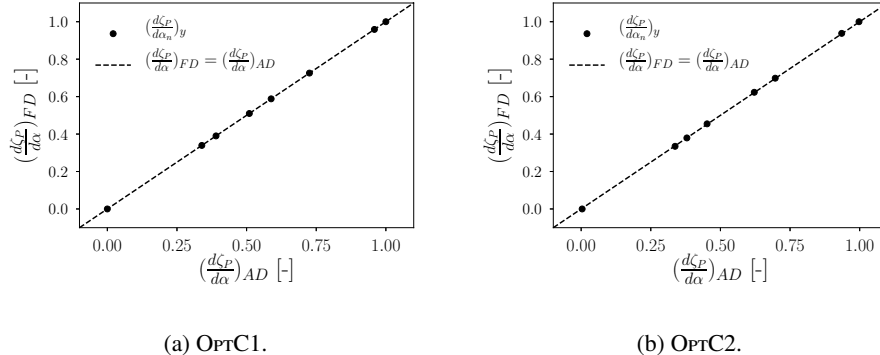


Figure 2.9: Verification between the normalized gradients of the objective function ζ_P with respect to the design variables α calculated with the adjoint mode of the AD and second order central difference finite difference (FD).

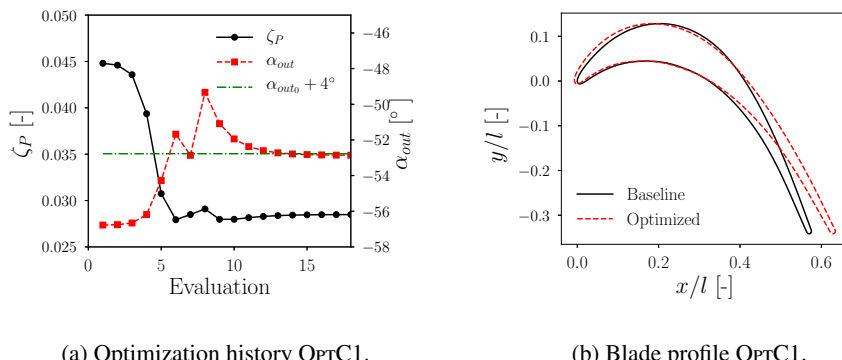


Figure 2.10: Shape optimization history of the total pressure loss coefficient and comparison between baseline and optimized blade profile (OPTC1).

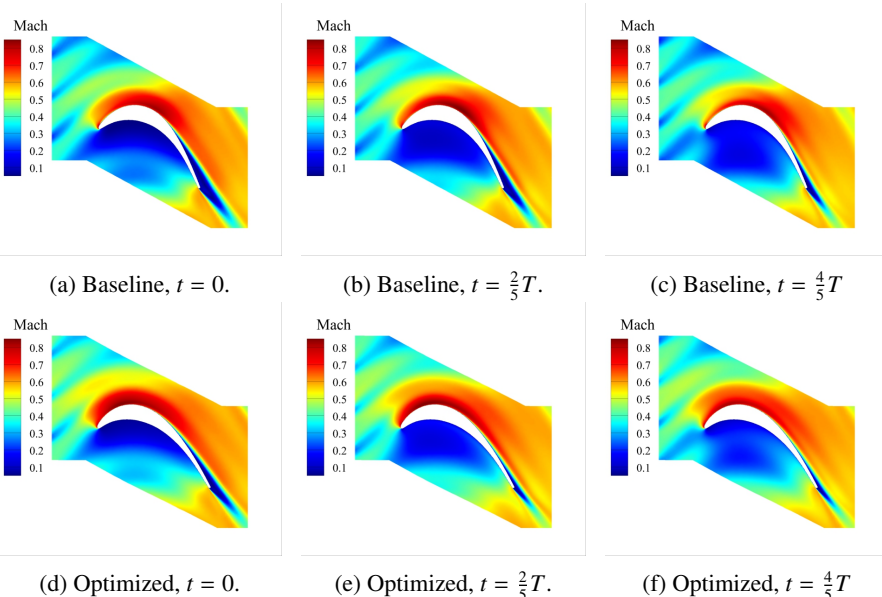


Figure 2.11: Mach number contours calculated at three different time instances with the HB method, based on the OPTC1 test case, for both the baseline (a, b, c) and the optimized (d, e, f) blade profile.

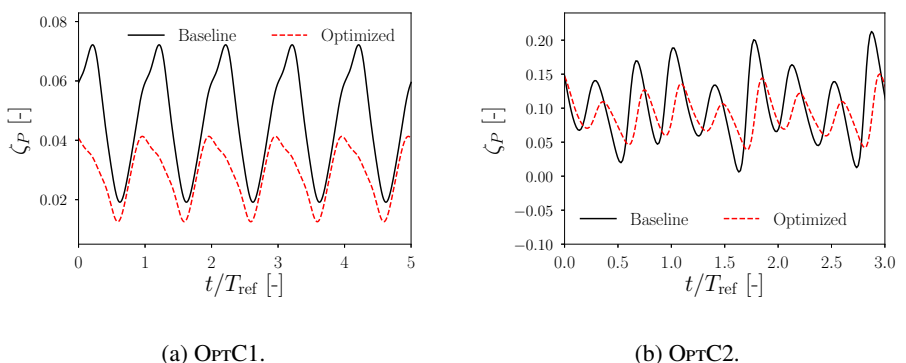


Figure 2.12: Total pressure loss coefficient evolution in time calculated with URANS simulation for both the baseline and the optimized configuration.

work [46], a time fluctuating inlet total pressure is prescribed as

$$\tilde{P}_{\text{tot}} = P_{\text{tot}} [1 + A_1 \sin(\omega_1 t) + A_2 \sin(\omega_2 t)], \quad (2.49)$$

where $A_1 = A_2 = 0.04$, $\omega_1 = 2\pi f_1$, and $\omega_2 = \omega_1/2.7$.

As for the OPTC1 configuration, a time-accurate simulation is performed to verify the HB solution and select the relevant input frequencies by analyzing the spectrum of the total pressure loss coefficient. Fig. 2.13a depicts the evolution in time of the total pressure loss coefficient resulting from both the URANS and HB computations. Tab. 2.4 reports the input frequency vectors for the HB simulation with the associated RMSE between the HB and URANS values of the total pressure loss coefficient.

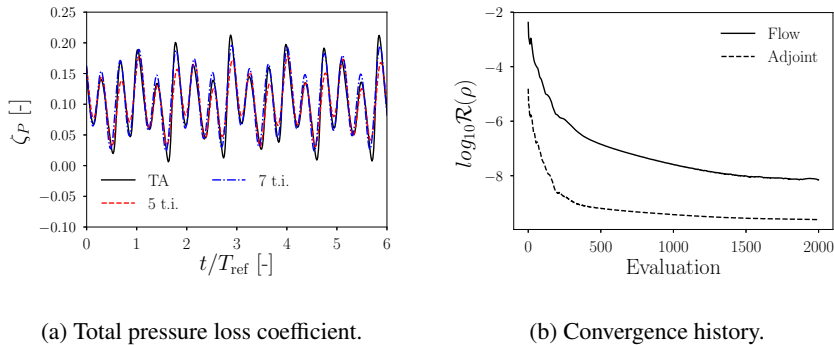


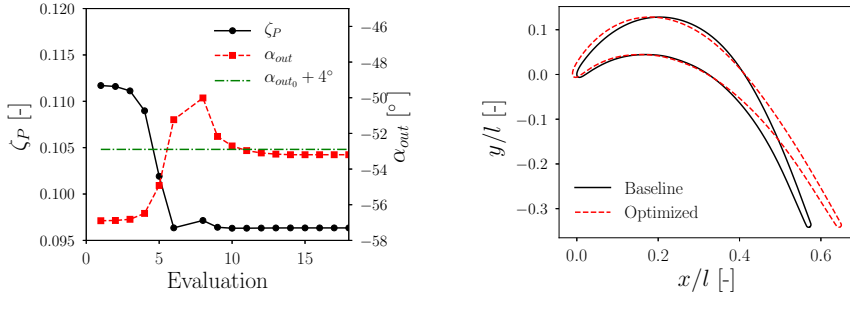
Figure 2.13: Comparison of the total pressure loss coefficient ζ_P as function of time, obtained with time-accurate and HB simulations (a); flow and adjoint solver convergence history of the first time instance density residual (b).

Figs. 2.15a, 2.15b, and 2.15c show Mach number contour plots, obtained for 3 of the 7 resolved time instances. In this case, as opposed to the OPTC1 configuration, the inlet flow field at the upstream boundary is uniform in space with no incoming wakes, given that time-varying, but uniform-in-space, values of total pressure and total temperature are imposed.

Table 2.4: Input frequencies corresponding to a different number of resolved time instances, for the OPTC2 (i.e. $\omega_2 = 2.7\omega_1$) configuration, and corresponding RMSE of the total pressure loss coefficient between time-accurate and HB simulation results.

N. time instances	Input frequencies	RMSE
5	$0, \pm\omega_1, \pm\omega_2$	0.041
7	$0, \pm\omega_1, \pm(\omega_2 - \omega_1), \pm\omega_2$	0.019

After analysis of the flow solution, the shape optimization is performed based on 7 time instances, and the corresponding averaged total pressure loss coefficient is chosen as



(a) Optimization history OptC2.

(b) Blade profile OptC2.

Figure 2.14: Shape optimization history of the total pressure loss coefficient and comparison between baseline and optimized blade profile (OptC2) .

the objective function. The adjoint-based gradients needed for the optimization are first compared with second-order finite differences. The results of this comparison are reported in Fig. 2.9b, and are characterized by a RMSE lower than $2 \cdot 10^{-5}$. Furthermore, as seen in Fig. 2.13b, the adjoint solver again inherits the convergence rate from the primal solver and its computational cost is about 1.7 higher than that associated with the primal solver. The average computational cost of the primal solver, for a single iteration, was about 1.98 seconds on a 4 cores *Intel Xeon E5-1620 Processor* with hyper-threading.

The design problem considered in this test case is analogous to that for the OptC1 configuration, and it is formally expressed by (2.48). Fig. 2.14a shows that the final design is reached after approximately 14 optimizer evaluations, satisfying the constraint on the outlet flow angle. The Mach contour plots for the optimized shape are shown in Fig. 2.15. Again, the flow separation on the rear suction side is significantly mitigated for all of the resolved time instances, due to the lower camber angle of the optimized blade profile (Fig. 2.14b). In this case, a reduction in the average pressure loss coefficient of approximately 14% is achieved with both the amplitude and maximum peak reduced by 44% and 29%, respectively. The time-dependent simulation of the optimized blade confirms these results (Fig. 2.12b) and reveal that no additional frequencies in the objective function spectrum are present when compared with those appearing in the solution for the baseline shape.

2.4 Conclusions

A fully-turbulent harmonic balance discrete adjoint formulation has been developed and applied to the shape optimization of two test cases in unsteady flows: i) a pitching airfoil with a moving grid, and ii) an axial turbine cascade subject to unsteady flow conditions at the inlet. The proposed method is based on a duality-preserving algorithm, which enables

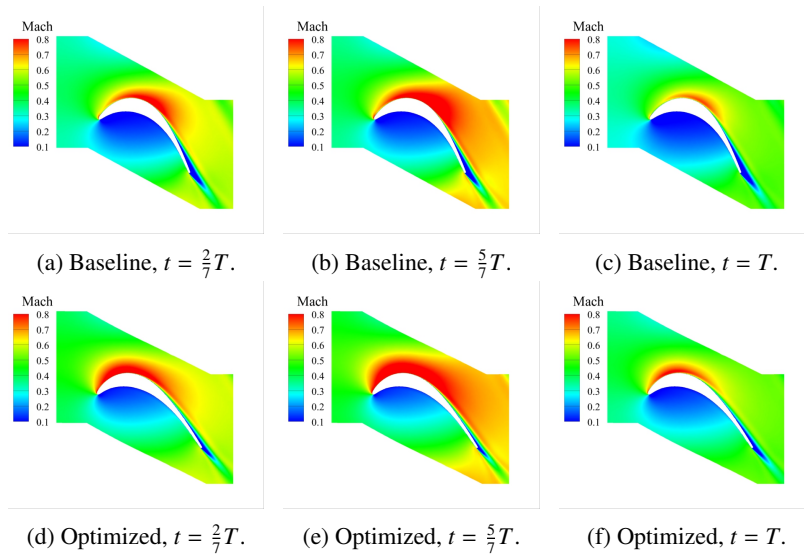


Figure 2.15: Mach number contours calculated at three different time instances with the HB method, based on the OptC2 test case, for both the baseline (a, b, c) and the optimized (d, e, f) blade profile.

the adjoint solver to inherit the convergence properties from the primal flow solver. Due to its efficiency, the framework enables shape optimization for quasi-periodically forced nonlinear fluid problems characterized by a set of frequencies that are not necessarily integer multiple of one fundamental harmonic.

The results of the two test cases have clearly demonstrated that the method is capable of providing accurate gradients in the unsteady setting, as compared to sensitivities computed by second-order finite differences. The gradient-based unsteady optimization has led to improvements of practical significance. The mean and the amplitude of the time-varying aerodynamic losses have been minimized with respect to the baseline configuration. This has been accomplished by considering the minimum number of input frequencies, according to a spectral analysis of the flow field, which results in significant computational cost savings.

The development of a fully-turbulent adjoint optimization framework based on HB paves the way to the solution of additional unsteady design problems that are encountered in numerous advanced applications, such as the multi-disciplinary optimization of turbomachinery, including novel concepts of propulsion systems based on boundary layer ingestion. Future efforts will be devoted to the comparison between fully-turbulent, time-accurate and HB adjoint-based shape optimization methods in order to assess advantages and drawbacks.

References

- [1] Johnson, F. T., Tinoco, E. N., and Yu, N. J., 2005. “Thirty years of development and application of CFD at Boeing Commercial Airplanes, Seattle”. *Computers & Fluids*, **34**(10), pp. 1115–1151.
- [2] Mavris, D. N., and Pinon, O. J., 2012. *An overview of design challenges and methods in aerospace engineering*. Springer, pp. 1–25.
- [3] Sobiesczanski-Sobieski, J., and Haftka, R. T., 1997. “Multidisciplinary aerospace design optimization: survey of recent developments”. *Structural and Multidisciplinary Optimization*, **14**(1), pp. 1–23.
- [4] Lian, Y., Oyama, A., and Liou, M.-S., 2010. “Progress in design optimization using evolutionary algorithms for aerodynamic problems”. *Progress in Aerospace Sciences*, **46**(5), pp. 199–223.
- [5] Li, Z., and Zheng, X., 2017. “Review of design optimization methods for turbomachinery aerodynamics”. *Progress in Aerospace Sciences*, **93**, pp. 1 – 23.
- [6] Pironneau, O., 1974. “On optimum design in fluid mechanics”. *Journal of Fluid Mechanics*, **64**(01), pp. 97–110.
- [7] Jameson, A., 1988. “Aerodynamic design via control theory”. *Journal of Scientific Computing*, **3**(3), pp. 233–260.
- [8] Kenway, G. K., and Martins, J. R., 2014. “Multipoint high-fidelity aerostructural optimization of a transport aircraft configuration”. *Journal of Aircraft*, **51**(1), pp. 144–160.
- [9] Lyu, Z., and Martins, J. R., 2014. “Aerodynamic design optimization studies of a blended-wing-body aircraft”. *Journal of Aircraft*, **51**(5), pp. 1604–1617.
- [10] Wang, D., He, L., Li, Y., and Wells, R., 2010. “Adjoint aerodynamic design optimization for blades in multistage turbomachines part ii: Validation and application”. *Journal of Turbomachinery*, **132**(2), p. 021012.
- [11] Mavriplis, D. J., 2008. *Solution of the unsteady discrete adjoint for three-dimensional problems on dynamically deforming unstructured meshes*. Aerospace Sciences Meetings. AIAA, Jan.

- [12] Economou, T. D., Palacios, F., and Alonso, J. J., 2015. “Unsteady continuous adjoint approach for aerodynamic design on dynamic meshes”. *AIAA Journal*, **53**(9), pp. 2437–2453.
- [13] Lucia, D. J., Beran, P. S., and Silva, W. A., 2004. “Reduced-order modeling: new approaches for computational physics”. *Progress in Aerospace Sciences*, **40**(1), pp. 51–117.
- [14] Hall, K. C., Thomas, J. P., and Clark, W. S., 2002. “Computation of unsteady nonlinear flows in cascades using a harmonic balance technique”. *AIAA journal*, **40**(5), pp. 879–886.
- [15] Gopinath, A., Van Der Weide, E., Alonso, J., Jameson, A., Ekici, K., and Hall, K., 2007. “Three-dimensional unsteady multi-stage turbomachinery simulations using the harmonic balance technique”. In 45th AIAA Aerospace Sciences Meeting and Exhibit, p. 892.
- [16] Ekici, K., Hall, K. C., and Dowell, E. H., 2008. “Computationally fast harmonic balance methods for unsteady aerodynamic predictions of helicopter rotors”. *Journal of Computational Physics*, **227**(12), pp. 6206–6225.
- [17] Van Der Weide, E., Gopinath, A., and Jameson, A., 2005. “Turbomachinery applications with the time spectral method”. *AIAA paper*, **4905**, p. 2005.
- [18] Choi, S., Lee, K., Potsdam, M. M., and Alonso, J. J., 2014. “Helicopter rotor design using a time-spectral and adjoint-based method”. *Journal of Aircraft*.
- [19] Huang, H., and Ekici, K., 2014. “A discrete adjoint harmonic balance method for turbomachinery shape optimization”. *Aerospace Science and Technology*, **39**, pp. 481–490.
- [20] Thomas, J. P., Hall, K. C., and Dowell, E. H., 2005. “Discrete adjoint approach for modeling unsteady aerodynamic design sensitivities”. *AIAA journal*, **43**(9), p. 1931.
- [21] Nadarajah, S. K., and Jameson, A., 2007. “Optimum shape design for unsteady three-dimensional viscous flows using a nonlinear frequency-domain method”. *Journal of Aircraft*, **44**(5), pp. 1513–1527.
- [22] Engels-Putzka, A., and Frey, C., 2015. “Adjoint harmonic balance method for forced response analysis in turbomachinery”. In Proceedings of the VI International Conference on Coupled Problems in Science and Engineering, International Center for Numerical Methods in Engineering, Barcelona, Spanien, pp. 645–656.
- [23] Ma, C., Su, X., and Yuan, X., 2017. “An efficient unsteady adjoint optimization system for multistage turbomachinery”. *Journal of Turbomachinery*, **139**(1), p. 011003.

-
- [24] Lyu, Z., Kenway, G. K., Paige, C., and Martins, J., 2013. “Automatic differentiation adjoint of the Reynolds-averaged Navier–Stokes equations with a turbulence model”. In 21st AIAA computational fluid dynamics conference, San Diego, CA, Vol. 10, pp. 6–2013.
 - [25] Palacios, F., Alonso, J., Duraisamy, K., Colombo, M., Hicken, J., Aranake, A., Campos, A., Copeland, S., Economou, T., Lonkar, A., et al., 2013. “Stanford University Unstructured (SU2): an open-source integrated computational environment for multi-physics simulation and design”. In 51st AIAA Aerospace Sciences Meeting Including the New Horizons Forum and Aerospace Exposition, p. 287.
 - [26] Economou, T. D., Palacios, F., Copeland, S. R., Lukaczyk, T. W., and Alonso, J. J., 2015. “SU2: An Open-Source Suite for Multiphysics Simulation and Design”. *AIAA Journal*, **54**(3), pp. 828–846.
 - [27] Nielsen, E. J., Lu, J., Park, M. A., and Darmofal, D. L., 2004. “An implicit, exact dual adjoint solution method for turbulent flows on unstructured grids”. *Computers & Fluids*, **33**(9), pp. 1131–1155.
 - [28] Mavriplis, D. J., 2006. “Multigrid solution of the discrete adjoint for optimization problems on unstructured meshes”. *AIAA journal*, **44**(1), pp. 42–50.
 - [29] Albring, T., Sagebaum, M., and Gauger, N. R., 2016. “Efficient aerodynamic design using the discrete adjoint method in SU2”. In 17th AIAA/ISSMO multidisciplinary analysis and optimization conference.
 - [30] Vitale, S., Albring, T. A., Pini, M., Gauger, N. R., and Colonna, P., 2017. “Fully turbulent discrete adjoint solver for non-ideal compressible flow applications”. *Journal of the Global Power and Propulsion Society*, **1**, pp. 252 – 270.
 - [31] Donea, J and Huerta, Antonio and Ponthot, J-Ph and Rodriguez-Ferran, A, 2004. *Arbitrary Lagrangian-Eulerian Methods*. Wiley, ch. 14.
 - [32] Menter, F., Kuntz, M., and Langtry, R., 2003. “Ten years of industrial experience with the sst turbulence model”. *Turbulence, Heat and Mass Transfer*; **4**(1), pp. 625–632.
 - [33] Jameson, A., Schmidt, W., and Turkel, E., 1981. “Numerical solution of the euler equations by finite volume methods using runge kutta time stepping schemes”. In 14th Fluid and Plasma Dynamics Conference, p. 1259.
 - [34] Jameson, A., 1991. “Time dependent calculations using multigrid, with applications to unsteady flows past airfoils and wings”. *AIAA paper*, **1596**, p. 1991.
 - [35] Gopinath, A., and Jameson, A., 2006. “Application of the time spectral method to periodic unsteady vortex shedding”. In 44th AIAA Aerospace Sciences Meeting and Exhibit, p. 449.

- [36] Banach, S., 1922. “Sur les opérations dans les ensembles abstraits et leur application aux équations intégrales”. *Fund. Math*, **3**(1), pp. 133–181.
- [37] Sagebaum, M., Albring, T., and Gauger, N. R., 2017. “High-Performance Derivative Computations using CoDiPack”. *arXiv preprint:1709.07229*.
- [38] Van Leer, B., 1979. “Towards the ultimate conservative difference scheme. V. A second-order sequel to Godunov’s method”. *Journal of Computational Physics*, **32**(1), pp. 101–136.
- [39] Kraft, D., 1998. A software package for sequential quadratic programming. Tech. rep., DLR German Aerospace Center Institute for Flight Mechanics, Köln, Germany.
- [40] Sagebaum, M., Albring, T., and Gauger, N. R., 2017. “High-Performance Derivative Computations using CoDiPack”. *arXiv preprint:1709.07229*.
- [41] Nimmagadda, S., Economou, T. D., Alonso, J. J., and Ilario da Silva, C. R., 2016. “Robust uniform time sampling approach for the harmonic balance method”. In 46th AIAA Fluid Dynamics Conference, p. 3966.
- [42] Hicks, R. M., and Henne, P. A., 1978. “Wing design by numerical optimization”. *Journal of Aircraft*, **15**(7), pp. 407–412.
- [43] Stadtmüller, P., and Fottner, L., 2001. “A test case for the numerical investigation of wake passing effects on a highly loaded LP turbine cascade blade”. In ASME Turbo Expo 2001: Power for Land, Sea, and Air, American Society of Mechanical Engineers.
- [44] Prasad, A., 2005. “Calculation of the mixed-out state in turbomachine flows”. *Journal of Turbomachinery*, **127**(3), p. 564.
- [45] Samareh, J., 2004. “Aerodynamic Shape Optimization Based on Free-Form Deformation”. In 10th AIAA/ISSMO Multidisciplinary Analysis and Optimization Conference.
- [46] Guédeney, T., Gomar, A., Gallard, F., Sicot, F., Dufour, G., and Puigt, G., 2013. “Non-uniform time sampling for multiple-frequency harmonic balance computations”. *Journal of Computational Physics*, **236**, pp. 317–345.

3

Fully-turbulent adjoint method for the
unsteady shape optimization of multi-row
turbomachinery

Abstract *The possibility of taking into account unsteady flow effects if performing turbomachinery shape optimization is attractive to accurately address inherently time dependent design problems. The harmonic balance method is an efficient solution for fluid dynamics turbomachinery problems characterized by quasi-periodic flows. If applied in combination with adjoint methods, it enables the computation of unsteady design problems in a cost effective way and opening up the way towards multi-disciplinary applications. This paper presents the development of a novel fully-turbulent discrete adjoint based on the time domain harmonic balance method and its application to the constrained fluid dynamic optimization of an axial turbine stage. As opposed to previous works the proposed method does not require any assumption on the turbulent eddy viscosity and on the set of input frequencies. The results show that the method provides accurate gradients, if compared with second order finite differences, and that the constant eddy viscosity approximation leads to significant deviation with respect to the fully-turbulent gradients. The application to the fluid-dynamic shape optimization of the exemplary stage leads to improvements of the total-to-static efficiency up to 0.8% and better performance if compared to the results obtained by means of a steady state optimization.*

3.1 Introduction

Adjoint-based shape optimization methods are increasingly becoming essential for automated design. Due to their efficiency in obtaining design sensitivities irrespectively of the number of design variables, these methods have allowed the possibility to effectively tackle multi-disciplinary optimization problems characterized by a high number of design variables and discretized on large domains [1].

Although originally formulated for aircraft design [2, 3], adjoint-based methods have been successfully extended to turbomachinery design problems. However, the majority of the methods currently adopted is based on steady state flow computations, essentially because this enables the reduction of the computational cost for design optimization [4–9].

Given the inherently unsteady nature of turbomachinery flows, the use of unsteady design methods is expected to provide steps forward in fluid dynamic performance as compared to steady state methods. Furthermore, if transient flow effects are accounted for, intrinsically unsteady multi-disciplinary optimization problems of turbomachinery can be effectively addressed. Examples include the minimization of tonal noise in transonic fans [10], the minimization of structural excitations caused by dynamic fluid-structure interaction phenomena [11], and the aero-thermal performance improvement of cascades subject to unsteady heat transfer mechanisms [12–14].

Due to the high computational cost and memory storage requirements associated with unsteady adjoints [15], several methods have been proposed to improve the efficiency of obtaining time-accurate design sensitivities. These methods mainly target the reduction of memory storage requirements. The algorithm proposed have resulted in less accurate gradient computations by time and space coarsening techniques [16] or in higher I/O overhead if checkpointing algorithms are adopted [17]. Recently, a discrete-adjoint method has been applied to time-accurate turbomachinery optimization in combination with time

coarsening [18].

Reduced order models have been investigated as a possible effective alternative to time-accurate simulations, in order to decrease the computational cost and storage requirements of the primal solver. The harmonic balance (HB) method, based on spectral discretization in time of the unsteady flow equations, is a cost effective option for non-linear dynamic problems dominated by a known set of frequencies.

Past work has been conducted to obtain HB-based adjoint design gradients for turbomachinery applications. Nevertheless, these studies are limited to the design of a single blade row, constant eddy viscosity and the inability to solve for spectral gaps [19, 20]. A design algorithm based on a fully-turbulent HB adjoint has been recently developed and applied to the optimization of problems characterized by quasi-periodic flows [21]. This algorithm is restricted to a single computational domain, thus only suited for the automated design of isolated turbomachinery cascades.

This paper documents the extension of the novel HB-based design method proposed in Ref. [21] to fully-turbulent multi-row simulations, enabling the solution of quasi-periodic unsteady optimization turbomachinery problems, without any restriction on the turbulent eddy viscosity and on the set of input frequencies to be resolved. The method is based on a *duality-preserving* approach [22] and it is implemented in the open source code SU2 [23, 24].

The design gradients obtained from the HB adjoint equations are verified using second-order central finite differences and applied to the constrained shape optimization of a gas turbine stage. Two expansion ratios are considered for the selected stage, corresponding to subsonic and transonic flow conditions. Furthermore, the baseline stage shape is optimized by means of both the proposed HB-based unsteady method and of a steady state method based on the mixing plane (MP) row interface. The objective of this comparison is to assess whether the HB-based automated design provides a gain in computed fluid dynamic performance over the MP-based one, and if these are dependent on the operating conditions. Finally, the computational performance of the method is analyzed in detail in terms of computational cost, memory, and storage requirements.

3.2 Method

Let ρ be the density, E the total specific energy, t time and \mathbf{v} the velocity vector in a Cartesian frame of reference, the semi-discrete form of the Navier-Stokes equations can be written as

$$\Omega \frac{\partial \mathbf{U}}{\partial t} + \mathcal{R}(\mathbf{U}) = 0, t > 0. \quad (3.1)$$

$\mathbf{U} = (\rho, \rho v_1, \rho v_2, \rho v_3, \rho E)$ is the vector of conservative variables and \mathcal{R} the residual operator applied to the spacial integration of the convective and viscous fluxes \mathbf{F}^c and \mathbf{F}^v . The application of an Arbitrary Lagrangian-Eulerian (ALE) formulation on the domain Ω , moving with velocity \mathbf{u}_Ω without deforming in time, and its boundary $\partial\Omega$ [25] results

in

$$\begin{aligned}\mathcal{R}(\mathbf{U}) &= f(\mathbf{F}^c, \mathbf{F}^v) && \text{in } \Omega, t > 0, \\ \mathbf{v} &= \mathbf{u}_\Omega && \text{on } \partial\Omega, t > 0.\end{aligned}\quad (3.2)$$

The convective fluxes are

$$\mathbf{F}^c = \begin{pmatrix} \rho(\mathbf{v} - \mathbf{u}_\Omega) \\ \rho\mathbf{v} \times (\mathbf{v} - \mathbf{u}_\Omega) + p\bar{\mathbf{I}} \\ \rho E(\mathbf{v} - \mathbf{u}_\Omega) + p\mathbf{v} \end{pmatrix}, \quad (3.3)$$

and the viscous fluxes are

$$\mathbf{F}^v = \begin{pmatrix} \cdot \\ \dot{\bar{\tau}} \\ \bar{\tau} \cdot \mathbf{v} + \kappa \nabla T \end{pmatrix}. \quad (3.4)$$

Here, p and T are the static pressure and temperature, κ the thermal conductivity, μ the dynamic viscosity and $\bar{\tau}$ the viscous stress tensor. More in general, for RANS equations, the vector of the conservative variables \mathbf{U} can be redefined as

$$\mathbf{U} := \begin{pmatrix} \mathbf{U}_l \\ \mathbf{U}_t \end{pmatrix}, \quad \mathcal{R}(\mathbf{U}) = \mathcal{R}(\mathbf{U}_f, \mathbf{U}_t) := \begin{pmatrix} \mathcal{R}_f(\mathbf{U}_l, \mathbf{U}_t) \\ \mathcal{R}_t(\mathbf{U}_l, \mathbf{U}_t) \end{pmatrix}, \quad (3.5)$$

in which $\mathbf{U}_l = (\rho, \rho v_1, \rho v_2, \rho v_3, \rho E)$ and \mathbf{U}_t is the vector of the conservative variables associated to the selected turbulence model. For example, in case of the Menter Shear Stress Transport (SST) model [26], $\mathbf{U}_t = (\rho\kappa, \rho\omega)$ with κ the turbulent kinetic energy and ω the specific dissipation.

Using an implicit Euler scheme, for time-discretization of (3.1), leads to

$$\Omega \mathcal{D}_t(\mathbf{U}^{q+1}) + \mathcal{R}(\mathbf{U}^{q+1}) = 0, \quad (3.6)$$

where q is the physical time step index, and \mathcal{D}_t is the time-derivative operator. After time-integration and linearizing the residual operator one can obtain the following expression applying the harmonic balance method [21] with dual-time stepping [27, 28] of pseudo-time τ

$$\left(\frac{\Omega \mathbf{I}}{\Delta\tau} + \mathbf{J} \right) \Delta \mathbf{U}_n = -\widehat{\mathcal{R}}_n(\mathbf{U}^q), \quad n = 0, 1, \dots, N-1. \quad (3.7)$$

with $\Delta \mathbf{U} = \mathbf{U}^{q+1} - \mathbf{U}^q$. N is the total number of resolved time instances, linked to the number of input frequencies K by $N = 2K + 1$. The operator $\widehat{\mathcal{R}}_n$ is defined as

$$\widehat{\mathcal{R}}_n(\mathbf{U}^q) = \mathcal{R}_n(\mathbf{U}^q) + \Omega \sum_{i=0}^{N-1} H_{n,i} \Delta \mathbf{U}_i + \Omega \sum_{i=0}^{N-1} H_{n,i} \mathbf{U}_i^q. \quad (3.8)$$

in which

$$\mathbf{H} = \begin{pmatrix} H_{1,1} & H_{1,2} & \cdots & H_{1,N} \\ H_{2,1} & H_{2,2} & \cdots & H_{2,N} \\ \vdots & \vdots & \ddots & \vdots \\ H_{N,1} & H_{N,2} & \cdots & H_{N,N} \end{pmatrix}, \quad (3.9)$$

is the harmonic balance operator, calculated as

$$\mathbf{H} = \mathbf{E}^{-1} \mathbf{D} \mathbf{E}. \quad (3.10)$$

\mathbf{E} and \mathbf{E}^{-1} are the direct and inverse Fourier matrix, and \mathbf{D} is the diagonal matrix containing the K input frequencies, i.e., $\mathbf{D} = \text{diag}(0, i\omega_1, \dots, i\omega_K, -i\omega_{-K}, \dots, -i\omega_1)$. A more detailed description is given in Ref. [21, 29].

For a steady-state calculation (3.7) reduces to

$$\left(\frac{\Omega \mathbf{I}}{\Delta \tau} + \mathbf{J} \right) \Delta \mathbf{U}_0 = -\mathcal{R}_0(\mathbf{U}^q). \quad (3.11)$$

3.2.1 Fully-turbulent discrete adjoint

The equations for the time-domain HB method formulated in Ref. [21] are here extended to account for multi-row fully-turbulent optimization of turbomachinery. The general formulation given here can be applied to any design problem involving multiple time-zones and geometrical zones and it does not require any restrictive assumption on the eddy viscosity.

The expression of (3.7) written as a fixed-point iteration is

$$\mathbf{U}_{z,n}^{q+1} = \mathcal{G}_{z,n}(\mathbf{U}^q), \quad (3.12)$$

in which $\mathbf{U}_{z,n}$ and $\mathcal{G}_{z,n}$ are the vector of conservative variables and the iteration operator of the pseudo time-stepping relative to the physical zone z and for time instance n . Each physical zone z corresponds to a blade row.

Using the definition of the operator $\mathcal{G}_{z,n}$ given in (3.12), the optimization problem for the generic objective function \mathcal{J} can be written as

$$\begin{aligned} & \underset{\alpha_z}{\text{minimize}} \quad \mathcal{J}(\mathbf{U}(\alpha_z), X(\alpha_z)) \\ & \text{subject to} \quad \mathbf{U}_{z,n}(\alpha_z) = \mathcal{G}_{z,n}(\mathbf{U}(\alpha_z), X_{z,n}(\alpha_z)), \quad n = 0, 1, \dots, N-1 \quad z = 0, 1, \dots, Z-1 \\ & \quad X_{z,0}(\alpha_z) = \mathcal{M}_z(\alpha_z). \end{aligned} \quad (3.13)$$

For each physical zone z and time instance n , α_z is the set of design variable, $X_{z,n}$ the physical grid, and \mathcal{M}_z is a differentiable function representing the mesh deformation algorithm. The objective function \mathcal{J} is obtained as the spectral average over the resolved

time instances and the physical zones

$$\mathcal{J} = \frac{1}{ZN^*} \sum_{z=0}^{Z-1} \sum_{n=0}^{N^*-1} \mathcal{J}_{z,n}^*, \quad (3.14)$$

with

$$\mathcal{J}_{z,n}^* = E^{*-1}(\mathcal{J}_{z,n} E), \quad (3.15)$$

in which E^{*-1} is the extended inverse discrete Fourier transform matrix of size $N \times N^*$ calculated for N^* time instances, whereas E is the $N \times N$ discrete Fourier transform matrix computed for the N input time instances ($N < N^*$). Equation (3.15) allows one, by means of Fourier interpolation on uniformly spaced samples, to reconstruct the trend of the objective function in time. Interpolation of the objective function to a larger time domain of N^* time instances, uniformly sampled.

The Lagrangian of the constrained optimization problem is given by

$$\mathcal{L} = \mathcal{J} + \sum_{z=0}^{Z-1} \sum_{n=0}^{N-1} ((\mathcal{G}_{z,n}(U(\alpha_z), X_{z,n}(\alpha_z)) - U_{z,n}(\alpha_z))^T \lambda_{z,n} + (\mathcal{M}_z(\alpha_z) - X_{z,0}(\alpha_z))^T \mu_z), \quad (3.16)$$

The differential of the Lagrangian is

$$\begin{aligned} d\mathcal{L} = & \sum_{z=0}^{Z-1} \sum_{n=0}^{N-1} \left(\frac{\partial \mathcal{J}}{\partial U_{z,n}}^T + \sum_{i=0}^{Z-1} \sum_{j=0}^{N-1} \frac{\partial \mathcal{G}_{i,j}}{\partial U_{z,n}}^T \lambda_{i,j} - \lambda_{z,n} \right) dU_{z,n} + \\ & \sum_{z=0}^{Z-1} \sum_{n=0}^{N-1} \left(\frac{\partial \mathcal{J}}{\partial X_{z,n}}^T + \frac{\partial \mathcal{G}_{z,n}}{\partial X_{z,n}}^T \lambda_{z,n} \right) dX_{z,n} - \mu_z dX_{z,0} + \\ & \sum_{z=0}^{Z-1} \frac{\partial \mathcal{M}_z}{\partial \alpha_z}^T \mu_z d\alpha_z, \end{aligned} \quad (3.17)$$

from which the adjoint equations can be obtained as

$$\frac{\partial \mathcal{J}}{\partial U_{z,n}}^T + \sum_{i=0}^{Z-1} \sum_{j=0}^{N-1} \frac{\partial \mathcal{G}_{i,j}}{\partial U_{z,n}}^T \lambda_{i,j} = \lambda_{z,n}, \quad (3.18)$$

and

$$\frac{\partial \mathcal{J}}{\partial X_{z,n}}^T + \frac{\partial \mathcal{G}_{z,n}}{\partial X_{z,n}}^T \lambda_{z,n} = \mu_z. \quad (3.19)$$

Equation (3.19) can be solved directly once the solution of (3.18) is known. Similar to the flow solver, (3.18) can be seen as a fixed-point iteration in $\lambda_{z,n}$, namely

$$\lambda_{z,n}^{q+1} = \frac{\partial \mathcal{N}}{\partial U_{z,n}}(U_{z,n}^*, \lambda^q, X_{z,n}), \quad (3.20)$$

where \mathbf{U}_n^* is the numerical solution for the flow equation (3.12) and \mathcal{N} is the shifted Lagrangian defined as

$$\mathcal{N} = \mathcal{J} + \sum_{z=0}^{Z-1} \sum_{n=0}^{N-1} \mathcal{G}_{z,n}^T(\mathbf{U}, X_{z,n}) \lambda_{z,n}. \quad (3.21)$$

Finally, the gradient of the objective function \mathcal{J} with respect to the vector of the design variables α_z can be computed from the converged flow and adjoint solutions using

$$\frac{d\mathcal{L}^T}{d\alpha_z} = \frac{d\mathcal{J}^T}{d\alpha_z} = \frac{\partial \mathcal{M}_z^T(\alpha_z)}{\partial \alpha_z} \boldsymbol{\mu}_z \quad z = 0, 1, \dots, Z - 1. \quad (3.22)$$

3.3 Application

The two-dimensional axial stage depicted in Fig. 3.1 was chosen in this work in order to test the proposed method. The blade geometries correspond to the mid-span profiles adapted from the 1.5 stage experimental setup of the Institute of Jet Propulsion and Turbomachinery at RWTH Aachen [30]. Compared to the original geometry the stator-rotor blade count ratio has been modified from 36:41 to 41:41. In order to resemble the flow characteristics of a typical gas turbine stage, the test case is simulated under the operating conditions given in Tab. 3.1, which correspond to subsonic (C1) and transonic (C2) flow conditions.

Table 3.1: Axial turbine stage main simulation parameters.

Parameter	C1	C2	Unit
Stator inlet blade angle	0	0	[°]
Total inlet reduced temperature	2.3	2.3	[·]
Expansion ratio	1.5	1.9	[·]
Isentropic work coefficient	0.9	2.2	[·]
Inlet turbulence intensity	5%	5%	[·]
Turbulent viscosity ratio	100	100	[·]

The fluid dynamic simulations are carried out using the open-source code *SU2* [23, 24], extended in this work to allow for multi-row HB based flow solutions and unsteady constrained optimization using the method discussed in Sec. 3.2. For both C1 and C2 the Roe scheme [31] is used to discretize the convective fluxes and second order accuracy is obtained by means of the MUSCL [32] approach with gradient limitation. The SST turbulence model [26] is employed for both test cases with a hybrid quad-triangular mesh of approximately 80,000 elements, in order to ensure a value of y^+ lower than 1 all along the blade surface. Non-reflective boundary conditions are imposed at the inlet and outlet

of the turbine cascade according to the formulation described in Refs. [33, 34]. The selected objective function is the dimensionless stage entropy generation calculated as

$$s_{\text{gen}} = \frac{\langle s_{\text{s,out}} \rangle - \langle s_{\text{s,in}} \rangle}{v_0^2/T_{0\text{s,in}}} + \frac{\langle s_{\text{r,out}} \rangle - \langle s_{\text{r,in}} \rangle}{v_0^2/T_{0\text{s,in}}}. \quad (3.23)$$

in which $\langle s_{\text{s,in}} \rangle$ and $\langle s_{\text{s,out}} \rangle$ are the entropy values calculated as mixed-out average [35] over the stator inlet and outlet. The same procedure is used to retrieve the average entropy at the rotor inlet, i.e. $\langle s_{\text{r,in}} \rangle$, and at the rotor outlet, i.e. $\langle s_{\text{r,out}} \rangle$. $T_{0\text{s,in}}$ is the total temperature at the stator inlet and v_0 the spouting velocity defined as $v_0 = \sqrt{2(h_{0,\text{in}} - h_{\text{is,out}})}$, where $h_{0,\text{in}}$ is the total enthalpy at the inlet of the stage and $h_{\text{is,out}}$ is the isentropic stage outlet static enthalpy. The stage entropy generation is calculated as the summation of the stator and rotor generation separately in order to prevent spurious entropy drops across the interface resulting from numerical accuracy and truncation errors.

3.3.1 Flow field analysis

The results from the harmonic balance (HB) simulations are first verified by comparison with the results obtained using a second-order accurate in time (TA) simulation and those obtained using a steady state mixing plane (MP) model at the stator-rotor interface. The time-accurate simulations are based on the dual time stepping method [28], using 50 time steps per period (corresponding to the blade pitch) and 80 inner iterations for a total of 10 periods.

Figure 3.2 shows the total-to-total stage efficiency, η_{tt} , as a function of time obtained from the TA and from the HB simulations. The HB-based unsteady η_{tt} approaches the TA results by increasing the number of resolved harmonics, with the subsonic configuration C1 approximating the URANS results by resolving a lower number of frequencies if compared to C2. This can be explained by observing that, in case of transonic simulations performed with the HB solver, flow effects that are non linear in time caused by the shock interaction between stator and rotor have to be modeled.

Table 3.1 summarizes $\delta_{\text{MP-HB}}$, i.e., the relative difference between the main time-averaged quantities characterizing the stage performance computed from the HB simulations and the corresponding ones resulting from the MP-based calculations. Furthermore, Tab. 3.1 reports the root mean square error of the HB-based and the TA-based stage performance as a function of time (RMSE_{TA-HB}). For both C1 and C2, the total-to-static stage efficiency given by the steady state simulations is characterized by a low deviation compared to the HB time-averaged results. The relative deviation is approximately 0.05% for C1 and 0.02% for C2. However, the total-to-total efficiency exhibits a larger relative difference between the HB-based and the MP-based simulation results, with the transonic configuration having a relative difference of 0.49% and the subsonic configuration of 0.17%.

Finally, Fig. 3.3 and Fig. 3.4 show the dimensionless static pressure distribution along the blade profiles retrieved from the MP and HB simulation results. For both C1 and C2, the steady state blade loading differs from the time-averaged harmonic balance blade

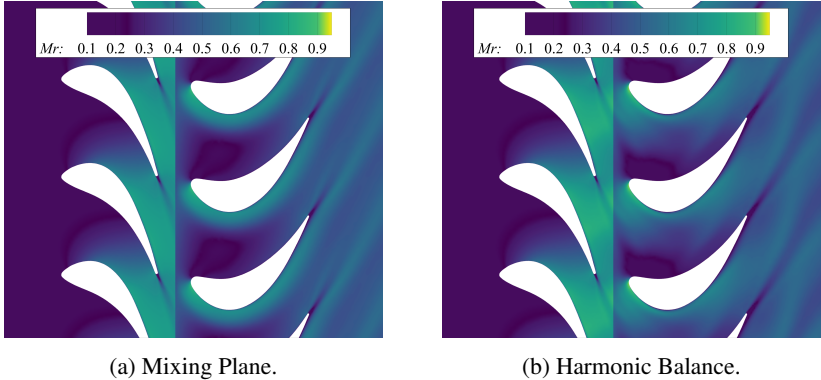
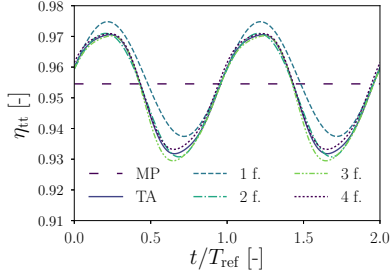


Figure 3.1: Relative Mach number contour plot for C1. The harmonic balance simulation results depicted in Fig. 3.1b are relative to $t = 0$.

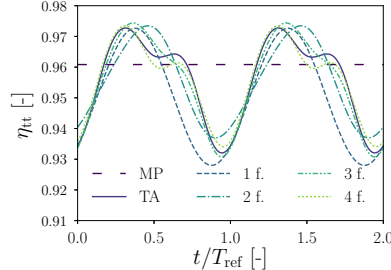
Table 3.2: Comparison of mixing plane (MP), harmonic balance (HB), and time accurate (TA) simulations results of the stage performance. $\delta_{\text{MP-HB}}$ is the relative difference between MP and time-averaged HB results for the selected performance. $\text{RMSE}_{\text{TA-HB}}$ represents the root mean square error between the time dependent TA and HB results.

	Parameter	MP	HB	TA	$\delta_{\text{MP-HB}} [\%]$	$\text{RMSE}_{\text{TA-HB}}$
C1	$\eta_{ts} [\%]$	83.15	83.19	83.13	-0.05	1.01e-4
	$\eta_{tt} [\%]$	95.45	95.29	95.19	+0.17	4.44e-5
C2	$\eta_{ts} [\%]$	84.24	84.26	84.26	-0.02	2.00e-3
	$\eta_{tt} [\%]$	96.08	95.61	95.64	+0.49	6.43e-4

loading. Furthermore, the shock wave intensity and the location of the associated flow discontinuity computed by the MP-based simulation deviate from the time-averaged HB results, for the transonic configuration C2. The main reasons for this difference are: i) a steady-state model with the MP interface cannot simulate the unsteady potential effects generated by the stator-rotor interaction; ii) the stator wake is not transported to the rotor when using the mixing plane interface; iii) for transonic calculations, the HB method is able to model the unsteady non-linear effects deriving from the shock waves appearing due to the imposed flow conditions and to the time-dependent mutual position of the blade rows.

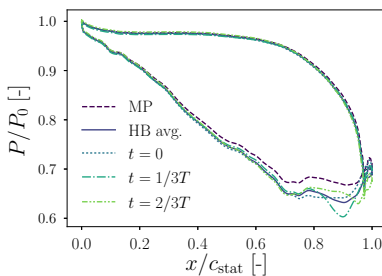


(a) C1.

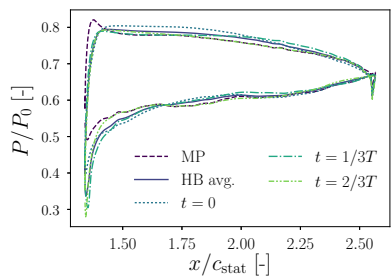


(b) C2.

Figure 3.2: Verification of the total-to-total efficiency as a function of time obtained with the HB method for a different number of input frequencies and the time-accurate URANS results (TA). The constant value corresponds to the steady state simulation results adopting the mixing plane (MP) stator-rotor interface.



(a) Stator.



(b) Rotor.

Figure 3.3: Dimensionless static pressure distribution over the stator and rotor blade surfaces for C1. The total inlet pressure P_0 is used as reference, for both stator and rotor.

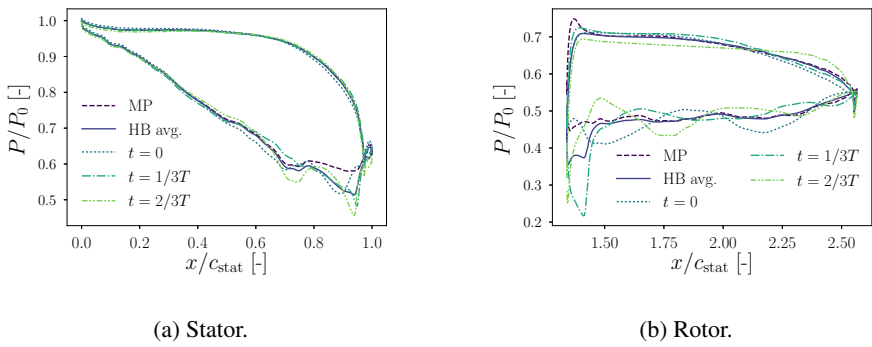


Figure 3.4: Dimensionless static pressure distribution over the stator and rotor blade surfaces for C2. The total inlet pressure P_0 is used as reference, for both stator and rotor.

3.3.2 Adjoint-based design sensitivities

The design gradients of the objective function with respect to the design variables, as defined by (3.22), are calculated for both the stator and the rotor of the selected test case. To this purpose, two free form deformation (FFD) boxes [36] containing the stator and rotor blade profiles are employed. The design variables (DVs) correspond to the control points of the FFD box as shown in Fig.3.5 for a set of twelve DVs per row.

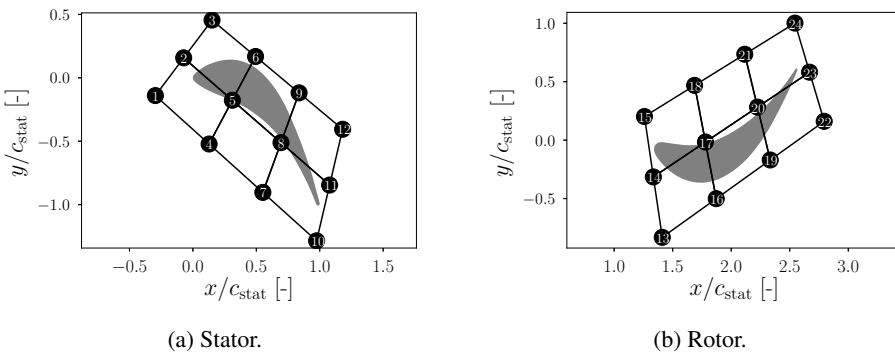


Figure 3.5: Blade profiles and example of free-form deformation (FFD) box.

The gradients obtained using the HB-based adjoint equations are first verified using second order finite differences (FD). The results of this verification are reported in Fig. 3.6a together with the results obtained using a steady-state adjoint solver [9] with the mixing-plane MP interface. For both HB and MP results there is a very good agreement between adjoint-based and finite differences gradients, with a RMSE of approximately 4e-3.

Fig. 3.6b depicts the normalized values of the design gradients for an increasing number of resolved frequencies as well as those computed with the steady state MP approach. The design variable numbering corresponds to the DV labels given in Fig. 3.5b. There are two main observations that can be drawn by analyzing Fig.3.6b: i) the value of the gradients computed with the HB-based adjoint is comparatively the same for more than two frequencies; ii) the largest discrepancy between HB and MP simulation results occurs in the proximity of the rotor leading edge. This can be attributed to the different physical models used for the steady and unsteady computations at the stator-rotor interface. All gradients converge to the same values towards the rotor outlet.

3.3.3 Constant eddy viscosity (CEV) assumption

As discussed in Sec. 3.2, the proposed HB-based adjoint method allows one to avoid the use of any restrictive condition on the turbulent eddy viscosity. Past work focused in adopting a constant eddy viscosity (CEV) approximation to ease the development process of the adjoint solver and to improve its computational efficiency but at the cost of a

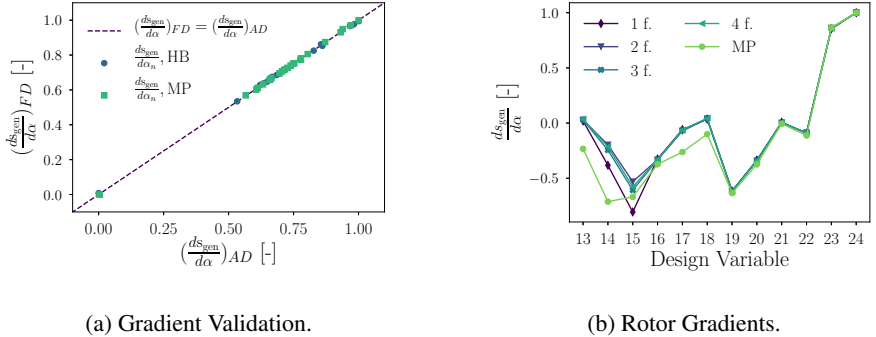
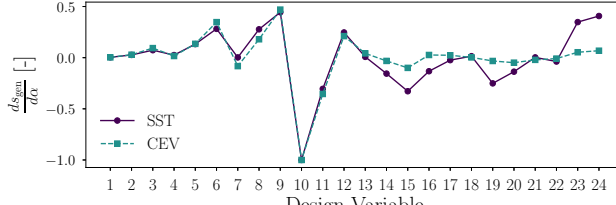


Figure 3.6: Validation of the C1 normalized adjoint-based design gradients using second-order finite differences, for both MP and HB (Fig. 3.6a). Rotor design gradients (y-direction) obtained with the MP and the HB method for a different number of input frequencies (Fig. 3.6b). The number of the design variables corresponds to the rotor FFD box given in Fig. 3.5b.

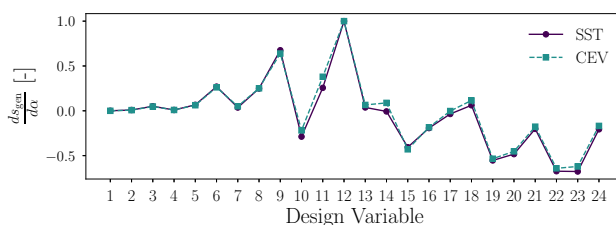
lower gradient accuracy [20, 37]. Because of this consideration, the impact of the CEV assumption on the design gradients is assessed. The aim of the analysis described here is to quantify the importance of adopting fully-turbulent adjoint methods for unsteady turbomachinery design.

Figure 3.7 reports the design gradients of the entropy generation obtained by using a fully-turbulent SST model and the CEV assumption. For both the C1 and C2 operating conditions, the largest differences between the two computed gradients are those relative to the rotor design variables. In addition, the deviations between CEV and SST-based gradients are more marked for the C1 configuration, therefore in case the flow is subsonic.

In order to quantify these differences, the relative deviation between the sensitivities computed by the CEV and SST model are presented in Fig. 3.8. Relative differences in excess of 20% can be observed for the C1 configuration whereas they are up to 12% for the C2 configuration. Differently from what has been reported in Ref. [37], the results of this analysis shows that the CEV approximation has a relevant effect on the final design gradients if compared to the fully-turbulent adjoint solution. This outcome confirms the results of a previous similar study, but limited to a comparison between the solutions obtained from a steady-state adjoint method [38].

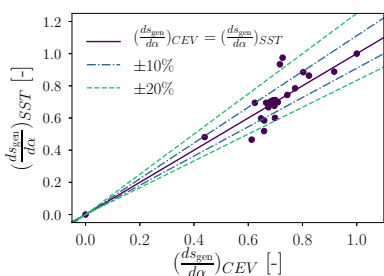


(a) C1 - Design Gradients.

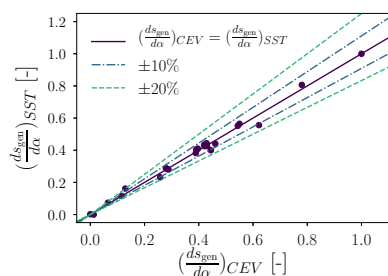


(b) C2 - Design Gradients.

Figure 3.7: Fully-turbulent (based on the SST turbulence model) vs constant eddy viscosity (CEV) design gradients, in the y -direction. The number of the design variables corresponds to the stator and rotor FFD boxes given in Fig. 3.5.



(a) C1 - Design Gradients.



(b) C2 - Design Gradients.

Figure 3.8: Comparison of the design gradients based on the SST turbulence model and those obtained by using a constant eddy viscosity (CEV) assumption.

3.3.4 Constrained optimization

The fully-turbulent design sensitivities, computed with the steady state MP and the unsteady HB method, are employed in a gradient-based design procedure to perform a constrained shape optimization of the selected turbomachinery test case. The modified version of the nonlinear least-squares method (SLSQP) [39] was selected as gradient-based optimization algorithm.

The constrained optimization problem of the turbine stage is formulated as

$$\begin{aligned} & \underset{\alpha}{\text{minimize}} \quad s_{\text{gen}}(\alpha), \quad \alpha = \{\alpha_1, \alpha_2\} \\ & \text{subject to: } P^* = P_0^*, \\ & \quad \delta_{t,z} = \delta_{t_0,z}, \quad z = 1, 2, \dots, n = 1, 2, \dots, N \\ & \quad \mathbf{U}_{z,n} = \mathcal{G}_{z,n}, \\ & \quad \mathbf{X}_{z,n} = \mathbf{M}_{z,n}. \end{aligned} \tag{3.24}$$

in which the objective function is given by the entropy generation of the stage, s_{gen} , averaged over all the N resolved time instances. s_{gen} is a function of the ensemble of the stator and rotor design variables, i.e. α_1 and α_2 . The dimensionless nominal power output of the stage P_0^* as well as the trailing edge thickness of both blade rows δ_{t_0} are imposed as constraints. The dimensionless power output is defined as follows

$$P^* = \frac{w \dot{m}}{\rho_{0,\text{in}} y_p u_b^3}, \tag{3.25}$$

with w the Euler work, \dot{m} the 2D mass flow rate based on the blade pitch y_p , $\rho_{0,\text{in}}$ the total density at the stage inlet, and u_b the blade speed.

Five time instances are selected to perform the optimization, from the analysis of the spectrum of the objective function and from the design sensitivities given by an increasing number of input frequencies (see e.g. Fig. 3.6b).

Figure 3.9 shows the evolution of the optimization for both C1 and C2. The entropy generation and the stage power output are scaled in order to better visualize the deviations between the steady and the unsteady results. In the case of the C1 configuration (Fig. 3.9a) the computed stage entropy generation is reduced by about 7% with the steady state optimization method and by approximately 20% with the HB-based optimization. The constraint on the power output is satisfied within 0.6% in both cases. Figure 3.9b depicts the optimization convergence for the C2 configuration. In this case, the objective function is reduced by approximately 11% for the steady optimization and 14% for the unsteady one. The equality constraint on the non-dimensional stage power is maintained within 0.8%.

Figures 3.10 and 3.11 report the baseline and the optimized blade profiles. For both C1 and C2 the largest deformations are located in the area of the rotor leading edge. The HB-based optimized shape is furthermore characterized, for C1 only, by a significant shape deformation on the stator suction side and on the rotor rear area. From the analysis of the final design, the largest differences between the steady and the unsteady optimization

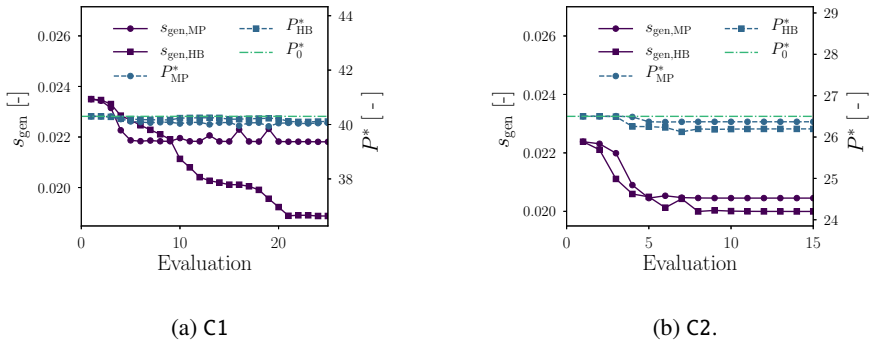


Figure 3.9: Optimization history.

results are associated with the subsonic operative conditions, i.e. C1. This occurs despite the fact that the discrepancy in performance between the steady and the HB simulation results, computed on the baseline profile, is lower for the C1 configuration (Tab. 3.2).

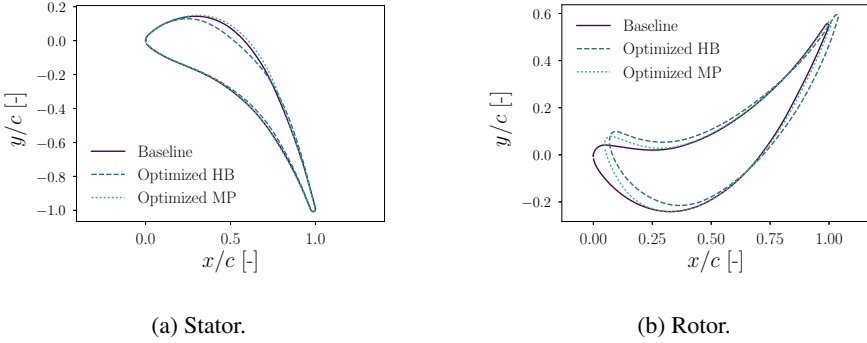
Additionally, a time-accurate simulation is performed using the optimized shapes obtained with both the steady and the unsteady optimization method. Figures 3.12 and 3.13 display the total-to-total stage efficiency and the non-dimensional stage power as a function of time computed with URANS simulations as well as the time-averaged values. Table 3.3 reports a summary of the final optimization results based on the total-to-total efficiency. The total-to-total efficiency of the C1 configuration is increased by approximately one percentage point using the HB-based optimization. The increase in efficiency achieved by means of the steady MP optimization is of 0.2 percentage points. Thus, the unsteady optimization method results in a higher performance improvement.

Table 3.3: Summary of harmonic balance (HB) and mixing plane (MP) optimization results. δ_{HB} and δ_{MP} are the relative difference between the baseline and the optimized results based on HB and MP, respectively.

Parameter	Baseline	HB_{opt}	MP_{opt}	δ_{HB}	δ_{MP}
C1	$\eta_{\text{tt}} \text{ [%]}$	95.10	96.05	95.30	+1.00
C2	$\eta_{\text{tt}} \text{ [%]}$	95.61	95.95	95.76	+0.36

Furthermore, the unsteady-based optimization better satisfies the power constraint, as depicted in Fig. 3.13a. The final time-averaged non-dimensional power from the HB-optimized stage differs by 0.3% from the baseline one whereas the MP-optimized solution differs by 2.0%.

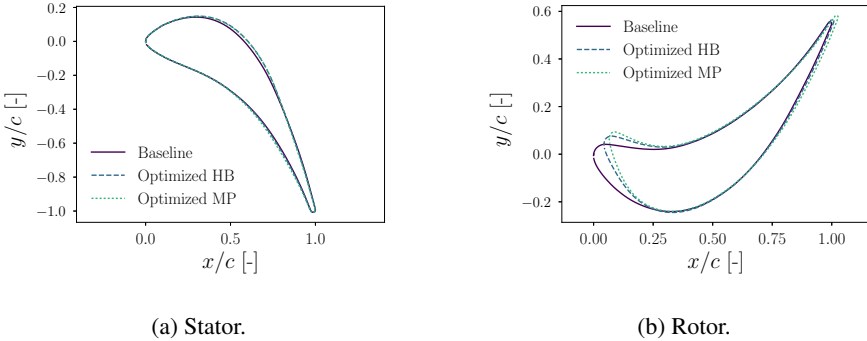
The time-accurate simulation results for the C2 configuration indicate that the HB-based optimization leads to an efficiency increase of about 0.4% compared to the 0.2% obtained by the MP-based one. For both final design solutions the power constraint is satisfied within 1%.



(a) Stator.

(b) Rotor.

Figure 3.10: Shape optimization for the C1 configuration.



(a) Stator.

(b) Rotor.

Figure 3.11: Shape optimization for the C2 configuration.

Finally, for both operating conditions the optimization leads to a reduced amplitude of the time-dependent efficiency and the dimensionless power. The decrease in amplitude of the total-to-total efficiency is 24.4% for C1 and 14.1% for C2. This demonstrates that the application of the proposed unsteady method intrinsically affects the variation in time of the objective function. As consequence, the variability can be optimized, if needed, by simply reformulating the objective function, i.e. including the amplitude of the quantity of interest in the optimization problem.

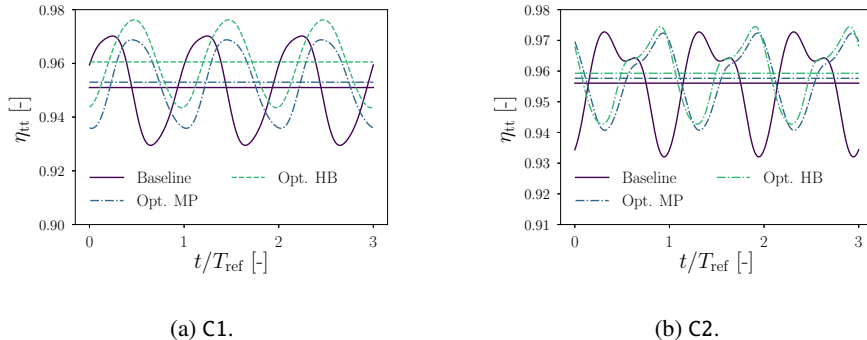


Figure 3.12: Total-to-total efficiency as a function of time for the baseline and the optimized blade profiles. The constant lines correspond to the average values.

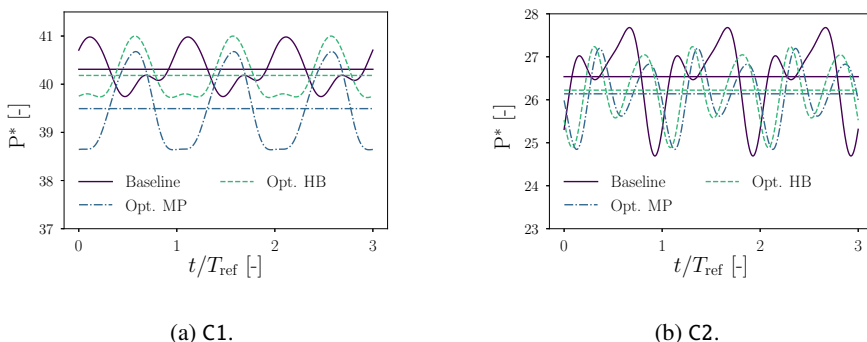


Figure 3.13: Dimensionless stage power as a function of time for the baseline and the optimized blade profiles. The constant lines correspond to the average values.

3.4 Performance assessment

The performance of the proposed HB-based design method is assessed in terms of computational cost, memory and storage requirements. This analysis is conducted for both the primal and the adjoint solver on a 2D and a 3D geometry.

3.4.1 2D stage

Figure 3.14 shows the performance results of the primal flow solver for the C1 configuration. The results are given as a function of the resolved input frequencies. The time-accurate simulations (TA) are initialized from a converged steady simulation. This is done in order to decrease the numerical transients necessary to reach a converged periodic solution.

Figure 3.14a reports the computational cost for the steady state (MP), harmonic balance (HB), and time-accurate (TA) simulations. The computational cost for the HB simulations scales as $2N + 1$, with N the number of input frequencies. This can be explained by recalling that, with the proposed HB method, in order to solve N frequencies $2N + 1$ time instances are required as expressed, e.g, in (3.8)). However, because of the semi-implicit HB formulation adopted in (3.7), for a number of frequencies higher than 4 a deterioration of the convergence rate is observed. This explains why the computational cost increases at a higher rate if the number of resolved frequencies is greater than four (Fig. 3.14a). In the case of two input frequencies the HB simulation is approximately 6.5 faster than the time-accurate (TA) simulation. The TA and the HB simulations feature nearly the same CPU time for 10 frequencies. The computational time associated to the steady state simulation is approximately 3 times lower than that of the HB simulation obtained for one input frequency.

Figure 3.14b depicts the memory and storage requirements for an increasing number of resolved frequencies. The results are normalized using the values obtained from the TA simulations. Both storage and memory increase linearly at a rate of $2N + 1$. For 2 input frequencies the the memory requirements of the TA simulations is about 4 times lower than the HB simulations, whereas the necessary storage is 41 times higher. These results outline the performance advantage of using HB-based over TA-based adjoint methods, for unsteady turbomachinery design.

The CPU time and memory requirements of the adjoint solver are 1.2 and 4.5 times higher if compared to the primal flow solver.

3.4.2 3D stage

The performance is analyzed for a 3D turbine stage operating at the same working conditions of C1. The goal of this analysis is to assess the capability to obtain adjoint-based sensitivities for a three-dimensional geometry and to evaluate its scalability in terms of computational cost, memory requirements and storage. Given the objective of the analysis, the calculations are conducted by assuming shrouded blades with and free-slip boundary conditions are applied to the hub and shroud. Based on these model assumptions, a

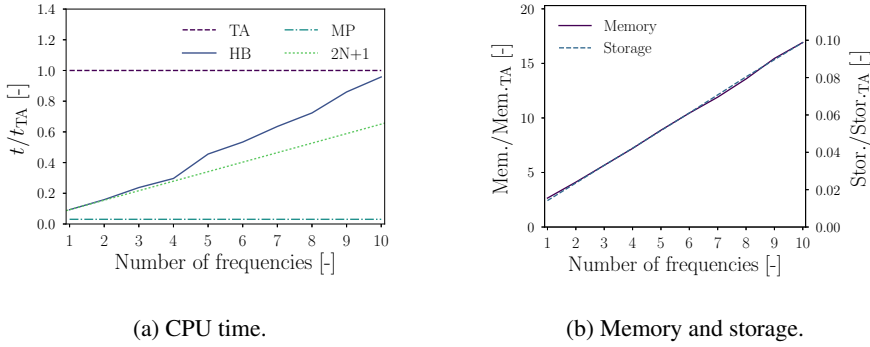


Figure 3.14: Performance assessment of the primal flow solver, as a function of the input frequencies: (a) Non-dimensional computational cost; (b) memory and storage requirements. The results of the time accurate (TA) simulations are used as reference values.

structured mesh of about 250 000 elements was selected after a mesh independence study. For this test case the numerical schemes employed are those used for C1 and C2.

A HB simulation based on 3 time instances is considered in order to compute the design sensitivities. Fig. 3.15a shows the geometry of the stage as well as the mid-span contours of the entropy generation normalized with the inlet conditions. The results are relative to the time instance $t = T/3$. Fig. 3.15b depicts the HB adjoint-based sensitivity corresponding to $t = T/3$.

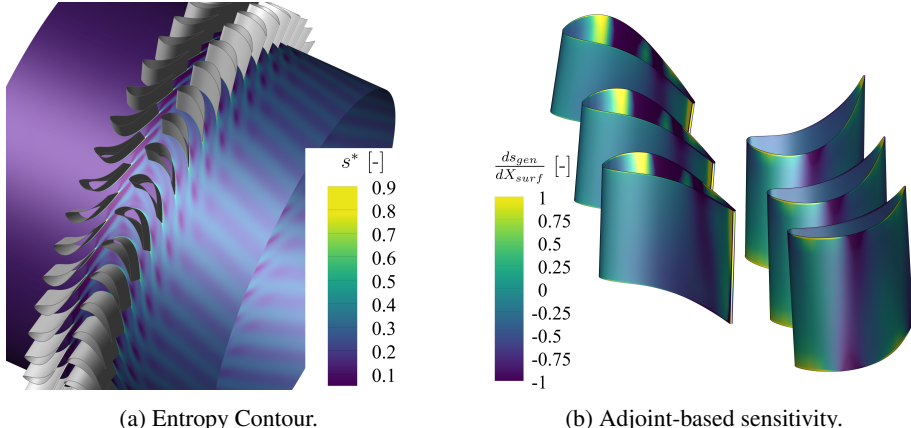


Figure 3.15: 3D axial stage simulation results: (a) normalized entropy generation contours; (b) normalized adjoint-based surface sensitivity.

Furthermore, the primal and the adjoint solver are tested considering a varying number of input frequencies to investigate the computational performance. Fig. 3.16 reports

the performance results of the primal flow solver obtained with a number of resolved harmonics ranging from 1 to 5. Similarly to the 2D test case the computational cost, the memory and storage requirements increase linearly at a rate of $2N + 1$. When 2 frequencies are resolved, the computational cost and the storage required by the TA simulation are approximately 3.5 and 42 times higher than the HB-based simulation. The memory required by the HB solver for 2 harmonics is about 4.7 times larger than that of the TA solver.

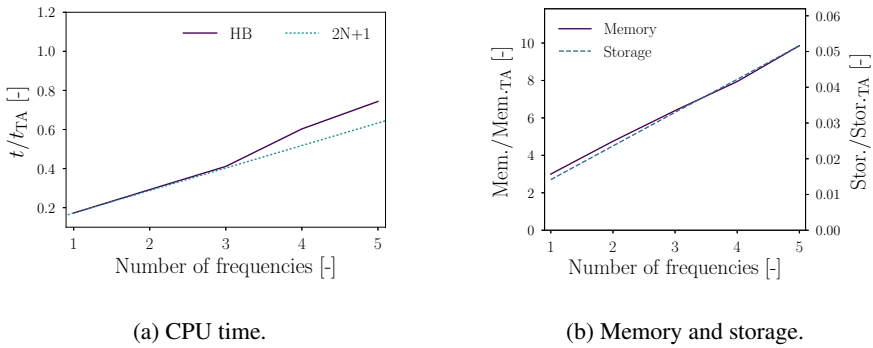


Figure 3.16: Performance assessment of the primal flow solver, as a function of the input frequencies: (a) Non-dimensional computational cost; (b) memory and storage requirements. The results of the time accurate (TA) simulations are used as reference values.

The computational cost of the adjoint solver is approximately 1.2 times higher than the primal solver, whereas the required memory of adjoint solver is about 4.9 times that of the flow solver. The memory required by the adjoint solver for the 250 000 elements mesh was 32.2Gb. The total simulation time for the adjoint solver was of approximately 450 minutes using a 10 cores *Intel Xeon E5-2687W v3* CPU with hyper-threading.

3.5 Conclusions

This work documents the development of a fully-turbulent harmonic balance (HB) discrete adjoint method for multi-row turbomachinery design. The method was applied to the constrained shape optimization of an exemplary axial turbine stage.

The key findings of this study can be summarized as follows

- The design sensitivities can be accurately calculated with the proposed HB discrete adjoint method. These sensitivities were verified using second order finite differences, without any assumption on the turbulent eddy viscosity.
- For fluid dynamic design purposes the number of relevant input frequencies to be resolved can be lower than those necessary to accurately model the flow behavior.
- The assumption of constant eddy viscosity (CEV) was found to significantly affect the accuracy of the design sensitivities. Relative differences in excess of 20% between the CEV-based and the fully-turbulent results were calculated.
- Computational cost, memory and storage requirements increase linearly at a rate proportional to the number of time instances. For a number of input frequencies higher than 4 the computational cost featured a slower convergence due to the semi-implicit formulation adopted for the HB flow solver.
- The HB-based simulations exhibited higher memory requirements but lower storage if compared to time-accurate (TA) RANS simulations. For the analyzed test case, if 2 input frequencies are considered, the memory requirements were approximately 4 times larger than that of the TA simulations, whereas the storage required was about 41 times smaller.
- The HB adjoint solver featured a computational cost approximately 1.2 higher when compared to the primal flow solver. The ratio between the memory required by the adjoint and flow solver was approximately 4.5.
- The optimization results achieved by the proposed HB adjoint show remarkable differences when compared with steady state optimization results. Differences in the optimized total-to-total stage efficiency up to 0.8 percentage points were obtained for the exemplary 2D test case.
- For the analyzed test case, the use of the unsteady optimization method always led to better fluid dynamics performance if compared to the steady state optimization results.

The focus of the present analysis was on the unsteady adjoint-based fluid dynamic optimization of a turbine stage characterized by an equal number of blade count per row. Future developments are devoted to extend the periodic boundary condition of the flow solver in order to simulate a single blade passage having unequal azimuthal blade pitch. This would enable the resolution of multi-stage unsteady problems characterized by a set of frequencies that are not integer multiple of one fundamental harmonic.

References

- [1] Kenway Gaetan K. W., and Martins Joaquim R. R. A., 2014. “Multipoint High-Fidelity Aerostructural Optimization of a Transport Aircraft Configuration”. *Journal of Aircraft*, **51**(1), p. 144160.
- [2] Jameson, A., 1988. “Aerodynamic design via control theory”. *Journal of scientific computing*, **3**(3), pp. 233–260.
- [3] Giles, M. B., and Pierce, N. A., 2000. “An introduction to the adjoint approach to design”. *Flow, turbulence and combustion*, **65**(3-4), pp. 393–415.
- [4] Wang, D., and He, L., 2010. “Adjoint aerodynamic design optimization for blades in multistage turbomachinespart i: Methodology and verification”. *Journal of Turbomachinery*, **132**(2), p. 021011.
- [5] Wang, D., He, L., Li, Y., and Wells, R., 2010. “Adjoint aerodynamic design optimization for blades in multistage turbomachinespart ii: Validation and application”. *Journal of Turbomachinery*, **132**(2), p. 021012.
- [6] Luo, J., Xiong, J., Liu, F., and McBean, I., 2011. “Three-dimensional aerodynamic design optimization of a turbine blade by using an adjoint method”. *Journal of Turbomachinery*, **133**(1), p. 011026.
- [7] Walther, B., and Nadarajah, S., 2015. “Optimum shape design for multirow turbomachinery configurations using a discrete adjoint approach and an efficient radial basis function deformation scheme for complex multiblock grids”. *Journal of Turbomachinery*, **137**(8), p. 081006.
- [8] Pini, M., Persico, G., Pasquale, D., and Rebay, S., 2015. “Adjoint method for shape optimization in real-gas flow applications”. *Journal of Engineering for Gas Turbines and Power*, **137**(3), p. 032604.
- [9] Vitale, S., Albring, T. A., Pini, M., Gauger, N. R., and Colonna, P., 2017. “Fully turbulent discrete adjoint solver for non-ideal compressible flow applications”. *Journal of the Global Power and Propulsion Society*, **1**, pp. 252–270.
- [10] Defoe, J. J., and Spakovszky, Z. S., 2013. “Effects of boundary-layer ingestion on the aero-acoustics of transonic fan rotors”. *Journal of Turbomachinery*, **135**(5), p. 051013.

- [11] He, L., and Wang, D., 2011. “Concurrent blade aerodynamic-aero-elastic design optimization using adjoint method”. *Journal of Turbomachinery*, **133**(1), p. 011021.
- [12] Michelassi, V., Martelli, F., Dénos, R., Arts, T., and Sieverding, C., 1998. “Unsteady heat transfer in stator-rotor interaction by two equation turbulence model”. In ASME 1998 International Gas Turbine and Aeroengine Congress and Exhibition, American Society of Mechanical Engineers, pp. V001T01A058–V001T01A058.
- [13] Ameri, A. A., Rigby, D. L., Steinþorsson, E., Heidmann, J., and Fabian, J. C., 2010. “Unsteady analysis of blade and tip heat transfer as influenced by the upstream momentum and thermal wakes”. *Journal of Turbomachinery*, **132**(4), p. 041007.
- [14] Atkins, N. R., Thorpe, S. J., and Ainsworth, R. W., 2012. “Unsteady effects on transonic turbine blade-tip heat transfer”. *Journal of Turbomachinery*, **134**(6), p. 061002.
- [15] Mavriplis, D. J., 2006. “Multigrid solution of the discrete adjoint for optimization problems on unstructured meshes”. *AIAA journal*, **44**(1), pp. 42–50.
- [16] Nimmagadda, S., Economou, T. D., Alonso, J. J., Silva, C., Zhou, B. Y., and Albring, T., 2018. “Low-cost unsteady discrete adjoints for aeroacoustic optimization using temporal and spatial coarsening techniques”. In 2018 AIAA/ASCE/AHS/ASC Structures, Structural Dynamics, and Materials Conference, p. 1911.
- [17] Wang, Q., Moin, P., and Iaccarino, G., 2009. “Minimal repetition dynamic checkpointing algorithm for unsteady adjoint calculation”. *SIAM Journal on Scientific Computing*, **31**(4), pp. 2549–2567.
- [18] Ntanakas, G., Meyer, M., and Giannakoglou, K. C., 2018. “Employing the time-domain unsteady discrete adjoint method for shape optimization of three-dimensional multirow turbomachinery configurations”. *Journal of Turbomachinery*, **140**(8), p. 081006.
- [19] Huang, H., and Ekici, K., 2014. “A discrete adjoint harmonic balance method for turbomachinery shape optimization”. *Aerospace Science and Technology*, **39**, pp. 481–490.
- [20] Ma, C., Su, X., and Yuan, X., 2017. “An efficient unsteady adjoint optimization system for multistage turbomachinery”. *Journal of Turbomachinery*, **139**(1), p. 011003.
- [21] Rubino, A., Pini, M., Colonna, P., Albring, T., Nimmagadda, S., Economou, T., and Alonso, J., 2018. “Adjoint-based fluid dynamic design optimization in quasi-periodic unsteady flow problems using a harmonic balance method”. *Journal of Computational Physics*.
- [22] Albring, T., Sagebaum, M., and Gauger, N. R., 2016. “Efficient aerodynamic design using the discrete adjoint method in SU2”. In 17th AIAA/ISSMO multidisciplinary analysis and optimization conference.

-
- [23] Palacios, F., Alonso, J., Duraisamy, K., Colombo, M., Hicken, J., Aranake, A., Campos, A., Copeland, S., Economou, T., Lonkar, A., et al., 2013. “Stanford University Unstructured (SU2): an open-source integrated computational environment for multi-physics simulation and design”. In 51st AIAA Aerospace Sciences Meeting Including the New Horizons Forum and Aerospace Exposition, p. 287.
 - [24] Economou, T. D., Palacios, F., Copeland, S. R., Lukaczyk, T. W., and Alonso, J. J., 2015. “SU2: An Open-Source Suite for Multiphysics Simulation and Design”. *AIAA Journal*, **54**(3), pp. 828–846.
 - [25] Donea, J and Huerta, Antonio and Ponthot, J-Ph and Rodriguez-Ferran, A, 2004. *Arbitrary Lagrangian-Eulerian Methods*. Wiley, ch. 14.
 - [26] Menter, F. R., 1993. *Zonal two equation k- ω , turbulence models for aerodynamic flows*. Fluid Dynamics and Co-located Conferences. AIAA, Jul. 1993-2906.
 - [27] Jameson, A., Schmidt, W., and Turkel, E., 1981. “Numerical solution of the euler equations by finite volume methods using runge kutta time stepping schemes”. In 14th Fluid and Plasma Dynamics Conference, p. 1259.
 - [28] Jameson, A., 1991. “Time dependent calculations using multigrid, with applications to unsteady flows past airfoils and wings”. *AIAA paper*, **1596**, p. 1991.
 - [29] Naik, K. R., 2017. “Fourier collocation methods for unsteady flows”. PhD thesis, Stanford University.
 - [30] Stephan, B., Gallus, H., and Niehuis, R., 2000. “Experimental investigations of tip clearance flow and its influence on secondary flows in a 1-1/2 stage axial turbine”. In ASME Turbo Expo 2000: Power for Land, Sea, and Air, American Society of Mechanical Engineers, pp. V001T03A099–V001T03A099.
 - [31] Roe, P. L., 1981. “Approximate riemann solvers, parameter vectors, and difference schemes”. *Journal of computational physics*, **43**(2), pp. 357–372.
 - [32] Van Leer, B., 1979. “Towards the ultimate conservative difference scheme. v. a second-order sequel to godunov’s method”. *Journal of computational Physics*, **32**(1), pp. 101–136.
 - [33] Giles, M. B., 1990. “Nonreflecting boundary conditions for euler equation calculations”. *AIAA journal*, **28**(12), pp. 2050–2058.
 - [34] Vitale, S., Albring, T. A., Pini, M., Gauger, N. R., and Colonna, P. “Fully turbulent discrete adjoint solver for non-ideal compressible flow applications”. *Journal of the Global Power and Propulsion Society*, **1**, pp. 252 – 270.
 - [35] Saxer, A. P., 1992. A numerical analysis of 3-D inviscid stator/rotor interactions using non-reflecting boundary conditions. Tech. rep., Cambridge, Mass.: Gas Turbine Laboratory, Massachusetts Institute of Technology.

- [36] Samareh, J., 2004. “Aerodynamic shape optimization based on free-form deformation”. In 10th AIAA/ISSMO multidisciplinary analysis and optimization conference, p. 4630.
- [37] Marta, A. C., and Shankaran, S., 2013. “On the handling of turbulence equations in RANS adjoint solvers”. *Computers & Fluids*, **74**, pp. 102–113.
- [38] Vitale, S., 2018. “Advancements in automated design methods for NICFD turbomachinery”. PhD thesis, Delft University of Technology.
- [39] Kraft, D., 1998. A software package for sequential quadratic programming. Tech. rep., DLR German Aerospace Center Institute for Flight Mechanics, Kohn, Germany.

4

A look-up table method based on unstructured grids and its application to non-ideal compressible fluid dynamic simulations

Part of the contents of this chapter appeared in:

A look-up table method based on unstructured grids and its application to non-ideal compressible fluid dynamic simulations. Rubino A., Pini, M., Kosec M., Vitale S., Colonna, P.

Journal of Computational Science, 2018

Abstract *Fast and accurate computation of thermo-physical properties is essential in computationally expensive simulations involving fluid flows that significantly depart from the ideal gas or ideal liquid behavior. A look-up table algorithm based on unstructured grids is proposed and applied to non-ideal compressible fluid dynamics simulations. The algorithm grants the possibility of a fully-automated generation of the tabulated thermodynamic region for any boundary and to use mesh refinement. Results show that the proposed algorithm leads to a computational cost reduction up to one order of magnitude, while retaining the same accuracy level compared to simulations based on more complex equation of state. Furthermore, a comparison of the LuT algorithm with a uniformly spaced quadrilateral tabulation method resulted in similar performance and accuracy.*

4.1 Introduction

The accurate estimation of the thermo-physical properties of fluids is essential for many engineering and scientific applications, and it requires complex models in case the behavior of the fluid departs from that of the ideal gas or ideal liquid. Fluids exhibiting non-ideal behavior are involved in various technologies such as advanced power and propulsion systems, refrigeration and air conditioning systems, oil and gas processes, etc. [1–4]. In these cases, the evaluation of thermo-physical properties is often necessary for system design and performance evaluation or to simulate the flow behavior within components. Fluid dynamic simulations of vapors in non-ideal states are also employed in more fundamental research (see, e.g., Ref. [5]) and the branch of fluid mechanics dealing with this type of fluid flows was recently termed *non-ideal compressible fluid dynamics* (NICFD) [6].

The computational cost associated with fluid thermodynamic models expressed in terms of equations of state (EoS) can become a limiting factor if accurate estimations are needed in combination with expensive simulations. This is the case, e.g., in the design and optimization of industrial components [7] or in computational fluid dynamics (CFD) [8]. In order to decrease the computational time related to the calculation of thermo-physical fluid properties, while maintaining a satisfactory level of accuracy, look-up table (LuT) methods are convenient and widely adopted [9].

A LuT method consists of three basic parts: 1. the tabulation of a discrete set of values of thermodynamic properties pertaining to states generated with a given EoS-base model; 2. a search algorithm; 3. an interpolation method. Since the tabulation is performed only once, at preprocessing level, this way of evaluating fluid thermophysical properties can greatly reduce the computational effort if the models are based on complex EoS, provided that the associated search algorithm is efficient. Furthermore, the interpolation technique must be carefully chosen in order to achieve a satisfactory level of accuracy, which is a fundamental requirement to guarantee convergence in CFD simulations and accuracy of the final result. LuT methods based on a structured mesh of the thermodynamic region of interest have been documented in the literature [9–12]. In order to increase the accuracy and decreasing the number of discretization points for the thermodynamic region of interest, algorithms based on adaptive Cartesian mesh have been proposed [13, 14].

However, the use of quadrilateral grids, in combination with local refinement, can lead to local discontinuities and poor interpolation accuracy of properties in the proximity of smooth boundaries [13, 15]. This can especially occur for property reconstructions or for interpolation close to the vapor-liquid saturation line.

The study described here resulted in *ug-LUT*, a new LuT method based on meshing the thermodynamic region of interest for a given fluid dynamic simulation by means of unstructured triangular grids. The generation of multidimensional thermodynamic tables is fully automated, even in case multiple fluid phases need to be computed. Unstructured grids allow for mesh refinements, a valuable feature in case of strong property variations, which occur in proximity of the vapor-liquid critical point, and of the saturation line in general. The *ug-LUT* method is applicable also to multi-component fluids. A search algorithm based on a trapezoidal map of the tabulated region contributes significantly to its computational efficiency. The *ug-LUT* method for thermo-physical property calculations is implemented within the open-source code *SU2* [16–18] and its verification is presented by means of paradigmatic CFD test cases of increasing fidelity. Finally, the *ug-LUT* algorithm is compared to a structured-based LuT approach with the aim of assessing its computational cost and memory requirements.

4.1.1 Generation of the thermodynamic mesh

An unstructured mesh is generated for the thermodynamic domain of interest. A 2D grid generator [19], based on the Advancing-Delaunay front method, was used in this study. The adopted grid generator allows for local refinements in selected regions of the thermodynamic domain. Figure 4.1 shows examples of thermodynamic meshes for siloxane MM (hexamethyldisiloxane, $C_6H_{18}OSi_2$), generated by selecting T and $\log(\rho)$ as input state variables. The use of unstructured mesh in combination with local refinement is proposed here as an effective alternative to structured and quad-tree grids. Quad-tree based algorithms are efficient for controlling the mesh refinement level, but can suffer from the following issues [13, 15]: i) storing and retrieving the mesh connectivity associated to the recursive tree structure; ii) hanging nodes at different sizes cells interfaces, if continuous property reconstruction is required; iii) additional interpolation, triangulation or a curvilinear mesh system might be necessary to reconstruct smooth boundaries (e.g. vapor-liquid saturation line).

Once the mesh patches are generated using any suitable set of state variables (two if the fluid is pure), all other needed fluid thermo-physical properties are computed at each mesh node with an appropriate thermodynamic library. The current implementation of the *ug-LUT* method makes use of an external thermodynamic library [20], which embeds a large variety of models based on complex equations of state (EoS). As an example, Fig. 4.2 reports the pressure contour for siloxane MM, obtained using a model based on an EoS in the *Span-Wagner* functional form [21].

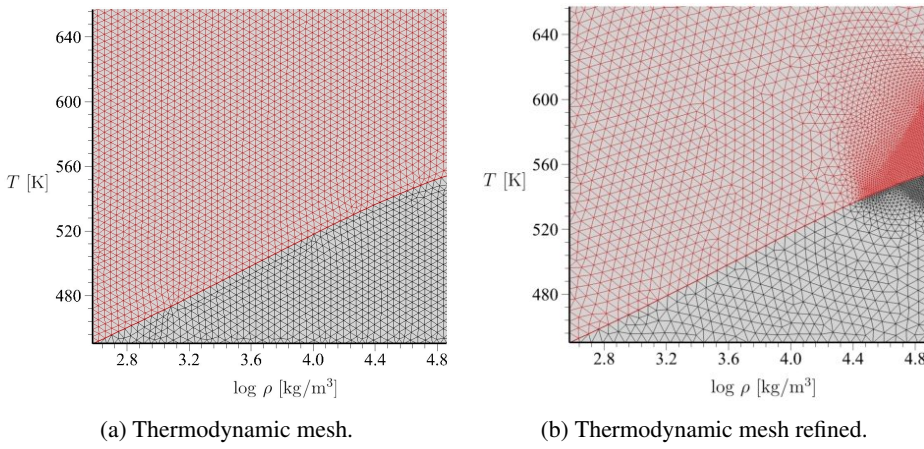


Figure 4.1: Thermodynamic triangular mesh for the siloxane MM. (a) Regular thermodynamic mesh. (b) Refined thermodynamic mesh.

4.1.2 Search algorithm

Once the set of needed thermo-physical properties of the selected fluid are stored in tabular form, a search algorithm is used to retrieve the best approximation of the query state or point. A point location algorithm based on a trapezoidal map has been adopted [22] because of the following considerations: i) the same geometrical connectivity is used for all the search pairs. This is especially beneficial because the connectivity has not to be recomputed for each search pair and it can be used to search in highly skewed thermodynamic planes. As an example for this, if the initial thermodynamic mesh is built for the (P, ρ) plane, the resulting mesh on the (h, s) plane will be highly skewed; ii) searching for the triangle containing the query vector by resorting to algorithms that do not use the mesh connectivity information (e.g. *kd-tree*) on an irregular and highly skewed grid can lead to inaccurate interpolation; iii) trapezoidal maps work for general polyhedra. The search algorithm can be used to switch between different mesh zones, characterized by a polyhedron outline. This feature avoids to perform a mapping of the grid for problems not conforming with a rectangular thermodynamic domain [13].

Given the set S of n triangular mesh edges, the trapezoidal map $\mathcal{T}(S)$ is built according to the following steps (see Fig. 4.3):

1. a unique set of edges and the corresponding list of its x coordinates is created by filtering out duplicates;
2. the intersecting edges are associated to each band;
3. the edges in each band are sorted.

The trapezoidal map $\mathcal{T}(S)$ is created in a pre-processing stage for each thermodynamic search pair, e.g., (h, s) , (ρ, v) , etc. A more detailed description of the trapezoidal

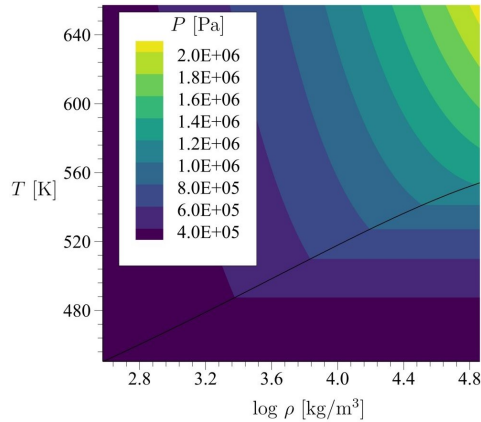


Figure 4.2: Tabulated pressure contours obtained for the siloxane MDM.

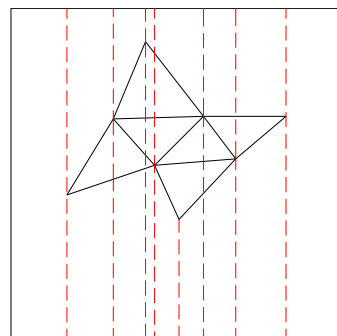


Figure 4.3: Schematic representation of the trapezoidal map for an unstructured grid.

map algorithm can be found in 4.4.

The mesh simplex, containing the query point q within $\mathcal{T}(S)$, is identified according to the following procedure:

1. the x coordinate of the query point is obtained with a binary search for its containing band;
2. within the containing band, the edge above and the one below the query point are identified;
3. the simplex containing the query point is singled out by using the edge-to-face connectivity of the two edges selected during the previous step.

The query algorithm is also detailed in 4.4.

4.1.2.1 Interpolation method

A two-dimensional linear interpolation problem can be written as

$$f(x, y) = \sum_{i=1}^N w_i g_i(x, y) = W^T G(x, y) = G^T(x, y) W, \quad (4.1)$$

where $G(x, y)$ is an interpolation basis which transforms the query coordinates x, y (raw features) into N linearly-independent interpolation features. An example of a polynomial basis function $G(x, y)$ on a triangle (three points, $N = 3$) is given by

$$G(x, y) = [1, x, y]^T. \quad (4.2)$$

In the implemented thermodynamic look-up-table, the two-dimensional coordinates are thermodynamic pairs such as $(\rho, u), (P, T), (h, s)$. This choice of $G(x, y)$ was found to provide sufficient accuracy, provided that a relatively fine mesh for the look-up-table is used. The vector of weights W is found through

$$A = \begin{bmatrix} G^T(x_1, y_1) \\ \vdots \\ G^T(x_i, y_i) \\ \vdots \\ G^T(x_N, y_N) \end{bmatrix}, \quad F = \begin{bmatrix} f(x_1, y_1) \\ \vdots \\ f(x_i, y_i) \\ \vdots \\ f(x_N, y_N) \end{bmatrix}, \quad AW = F \quad (4.3)$$

where N is the number of sample points on which the interpolation is based and the $f(x_i, y_i)$ are the known values. In the above relation F is an implicit function of the query point (x_q, y_q) . The mapping from the query point to the forcing vector F is given by the trapezoidal map algorithm, which provides the interpolation points. The interpolation is computationally efficient when a single function is being interpolated at many different combinations of query point coordinates (x_q, y_q) , as all the sample points can use the same weights.

However, the completion of the thermodynamic look-up-table requires the interpolation

of several functions (ten or more) for each query point. Thus, it is convenient to work out the dual form of the primal interpolation problem, such that the weights have to be computed only once for a given query point. The dual problem can be written as

$$G(x_q, y_q)^T W = F^T V, \quad (4.4)$$

where the interpolation weights V are now the adjoint solution of

$$A^T V = G(x_q, y_q). \quad (4.5)$$

The equivalence of the two formulations can be put into evidence by [23]

$$V^T F = V^T (AW) = (A^T V)^T W = G(x_q, y_q)^T W. \quad (4.6)$$

The weights V can be computed once for a given query point and reused to calculate the different thermodynamic properties of interest. Only one matrix-multiplication is therefore required per each mesh triangle instead of the twelve which would be needed with the primal interpolation method.

Additionally, since the $(A^T)^{-1}$ matrix depends only on a-priori established values, it can be completely pre-computed without additional runtime cost. If the condition number of the matrix is high, a pseudo-inverse should be applied; in this case pre-computation is only possible with the primal interpolation.

4.2 Application to NICFD simulations

In order to verify and provide information on the performance of the *ug-LUT* method, three CFD test cases of increasing complexity level are discussed. The selected test cases feature expansions characterized by relevant non-ideal compressible flow effects, requiring the use of complex equations of state to accurately compute the flow behavior. The simulations are performed with *SU2* [16], a code previously verified for non-ideal compressible fluid dynamics simulations [24]. For all test cases, the convective fluxes are discretized by a generalized Roe scheme [24, 25], and second-order accuracy is achieved with the *MUSCL* approach [26]. Ref. [16] provides a more detailed description of the flow solver and the associated numerical methods.

The thermodynamic properties needed by the flow solver, whose value is interpolated from the values stored in the LuT are

$$\rho, P, T, c, e, h, s, \left(\frac{\partial P}{\partial \rho} \right)_e, \left(\frac{\partial P}{\partial e} \right)_\rho.$$

The partial derivatives of the pressure are necessary to calculate the convective fluxes in non-ideal compressible flow simulations, see, e.g., Ref. [18].

Parameter	Value	Unit
Working fluid	MM	-
Total inlet temperature	530.28	K
Total-to-static pressure ratio	1.84	-
Inlet compressibility factor	0.64	-
Inlet turbulence intensity	0.05	-

Table 4.1: Input parameters for the 2D inviscid *ORCHID* nozzle simulation.

4.2.1 2D supersonic nozzle

The geometry of the converging-diverging supersonic nozzle is depicted in Fig. 4.5a, together with the Mach contour lines resulting from the Euler simulation. The two-dimensional flow domain is discretized with approximately 15,000 triangular mesh elements and the working fluid is siloxane MM. Tab. 4.1 reports the main simulation parameters.

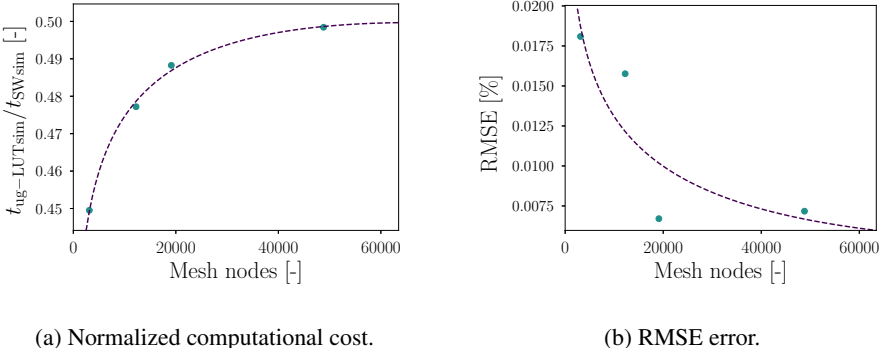
In order to assess the performance of the method, the computational cost of the nozzle simulation relying on the *ug-LUT* algorithm for the evaluation of fluid properties (*ug-LUTsim*) is compared with one in which the properties are provided to the flow solver by the external thermodynamic library based on the Span-Wagner EoS (*SWsim*), for an increasing number of thermodynamic mesh nodes. Figure 4.4a shows the computational cost of *ug-LUTsim* as a function of the mesh nodes, normalized with the computational cost of *SWsim*. Figure 4.4b reports the root-mean-square error (RMSE) between the flow field Mach number of *ug-LUTsim* with respect to *SWsim* for different thermodynamic mesh refinements. As expected, the RMSE value decreases with the number of thermodynamic mesh elements, whereas the computational cost shows the opposite trend.

Figure 4.5b shows a comparison of the Mach number calculated at the nozzle center line with *ug-LUTsim* and simulations in which fluid properties are evaluated with the ideal-gas model (*IGsim*) and with a model based on the Span-Wagner EoS (*SWsim*). The streamwise Mach distribution obtained with *ug-LUTsim* is well in agreement with the *SWsim*. As expected, both deviate from the distribution obtained with the *IGsim*, considering that the inlet compressibility factor significantly departs from unity ($Z = 0.64$).

4.2.2 Turbulent transonic 2D turbine cascade

The turbine cascade reported in Fig.4.6a was simulated under transonic conditions, in order to evaluate the performance of the *ug-LUT* method in case of RANS simulations. A hybrid mesh of approximately 40,000 elements was used to discretize the computational domain, with about 15,000 quads in the proximity of the blade surface to ensure $y^+ \approx 1$. The simulation parameters are listed in Tab.4.2.

Similarly to the previous test case, Fig. 4.6 reports the same trend in terms of computational cost and RMSE based on the Mach flow field. However, the computational gain provided in the RANS simulation is approximately 4 times higher as compared to



(a) Normalized computational cost.

(b) RMSE error.

Figure 4.4: Supersonic nozzle simulation results. (a) Normalized computational cost of the simulation employing the look-up table method (ug -*LUTsim*) compared to that of the simulation obtained using the Span-Wagner thermodynamic model ($SWsim$). (b) Relative mean square error of the Mach field from the $SWsim$ and ug -*LUTsim*. The $SWsim$ results obtained are taken as reference.

Parameter	Value	Unit
Working fluid	MDM	-
Total inlet temperature	592.30	K
Total-to-static pressure ratio	1.26	-
Inlet compressibility factor	0.598	-

Table 4.2: Input parameters for the 2D turbulent *LS89* turbine cascade simulation.

the inviscid test case. Fig.4.6b shows the comparison between the dimensionless static pressure, along the blade profile, from the *IGsim*, the *SWsim* and the *ug*-*LUTsim*. The results achieved with the *SWsim* are well in agreement with *ug*-*LUTsim*, while both differ from the ones obtained with *IGsim*.

In order to further investigate the performance of the proposed tabular method, the same turbine configuration is simulated with the binary mixture MDM(85%)/MM(15%) as working fluid. For this test case, the cost reduction is approximatively 5 times higher than the computation of the single-component working fluid (Fig. 4.8b), while retaining the same accuracy (Fig.4.6a). These results show that the use of the LuT method is even more attractive when applied to flow problems involving mixtures.

4.2.3 Turbulent 3D supersonic ORC turbine cascade

The supersonic stator of the mini-ORC turbine, documented in Ref. [27], is finally considered to investigate the computational efficiency of the look-up table method for three-dimensional RANS simulations. The numerical parameters of the test case are provided

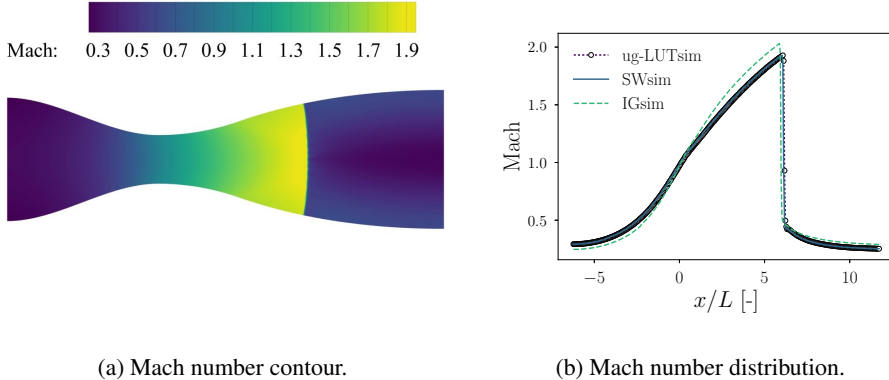


Figure 4.5: ORCHID nozzle simulation results, obtained with a thermodynamic mesh of about 20,000 elements. (a) Mach number contour obtained with the *ug-LUT* algorithm. (b) Mach number distribution at centerline obtained from the *IGsim*, *SWsim*, and *ug-LUTsim*.

Parameter	Value	Unit
Working fluid	MM	-
Total inlet temperature	573.15	K
Total-to-static pressure ratio	14.71	-
Inlet compressibility factor	0.77	-
Inlet turbulence intensity	0.05	-

Table 4.3: Input parameters for the 3D turbulent *ORCHID* turbine cascade simulation.

in Tab.4.3. The physical mesh consists of about one million cells and the thermodynamic grid is composed by approximately 20,000 elements.

Fig. 4.9a show the contour of the density gradient: a complex flow pattern of both shock-waves and fans is present in the semi-bladed region, due to the post-expansion phenomena. Fig. 4.9b displays the density field relative error between the *ug-LUTsim* and the *ug-LUTsim*. The deviation in the order of 0.1% points out that, even with a relatively coarse thermodynamic grid, the tabular approach is accurate for three-dimensional problems involving complex flow phenomena. Furthermore, the computational cost reduction for the 3D RANS simulation is very similar to the the analysed 2D RANS test case, as shown in Fig. 4.10.

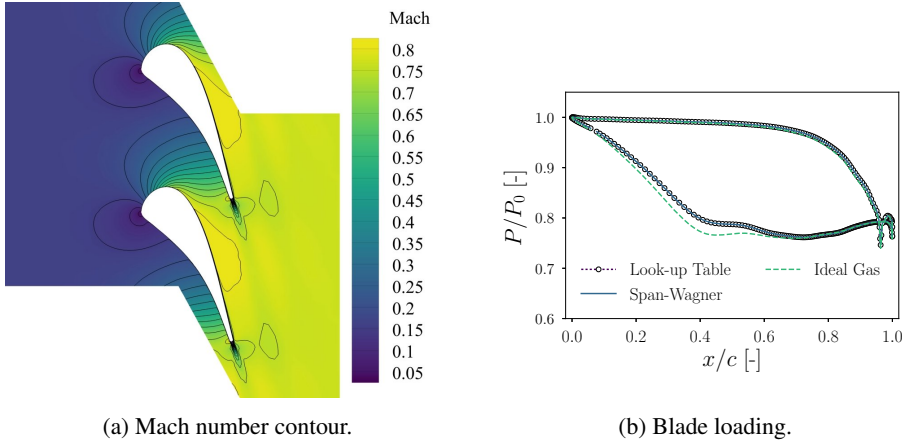


Figure 4.6: LS-89 simulation results. (a) Mach number distribution with the *ug-LUT* algorithm (b) Blade pressure distribution obtained from the *IGsim*, *SWsim* and *ug-LUTsim*.

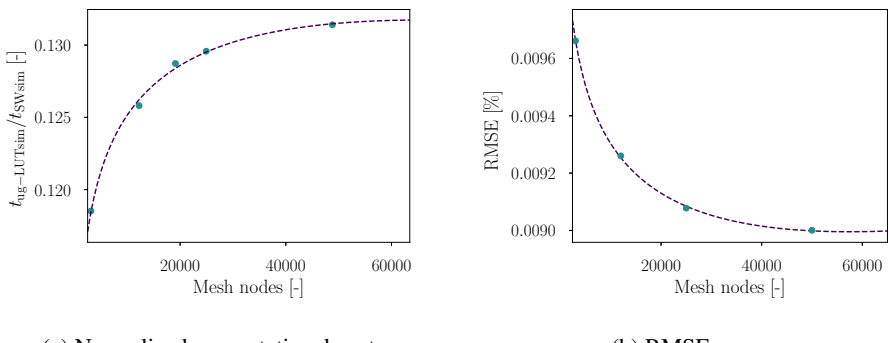


Figure 4.7: LS-89 simulation results. (a) Normalized computational cost of the simulation employing the look-up table method (*ug-LUTsim*) compared to that of the simulation obtained using the Span-Wagner thermodynamic model (*SWsim*). (b) Relative mean square error of the Mach field from the *SWsim* and *ug-LUTsim*. The *SWsim* results obtained are taken as reference.

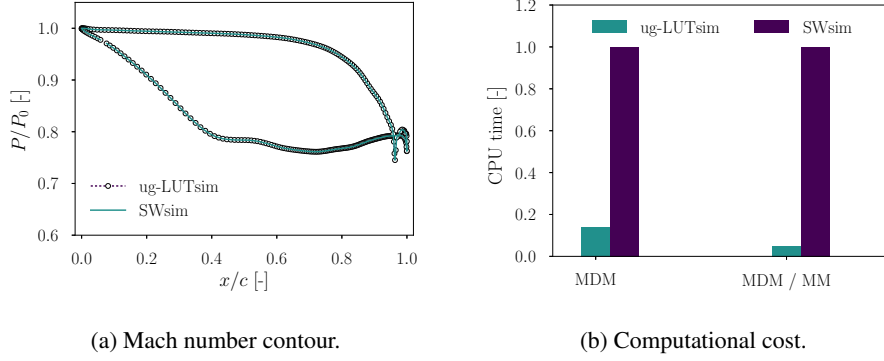


Figure 4.8: LS-89 simulation results operating with the MDM(85%)/MDM(15%) mixture. (a) Blade pressure distribution obtained from *ug-LUTsim* and *SWsim*. (b) Comparison between computational time associated with the single-component working fluid (MDM) and the MDM(85%)/MDM(15%) mixture. Results are normalized using the computational time associated with the *SWsim* as reference.

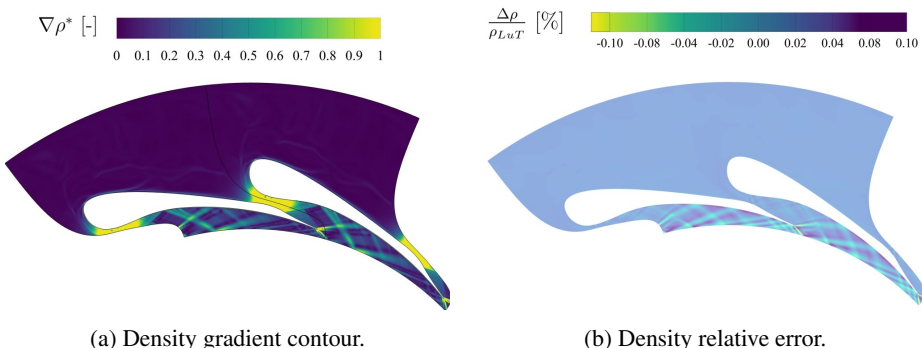


Figure 4.9: 3D turbine cascade simulation results. (a) Normalized density gradient distribution obtained with the *ug-LUT* algorithm (b) Density realtive error between the *ug-LUTsim* and the *SWsim* results.

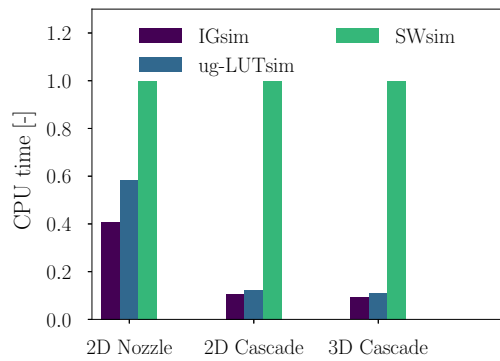


Figure 4.10: Summary of the computational time for the selected test-cases. Results are normalized using the computational time associated with the *SWsim* as reference.

4.3 Performance and memory assessment

An equally-spaced structured-based LuT method was implemented within *SU2*, in order to assess the performance of *ug-LUT*. The structured-based LuT algorithm was considered for carrying out a comparison in terms of computational cost and memory requirements because of its simple data structure and efficiency. The *LS-89* turbine cascade, described in Sec. 4.2.2, is selected as reference test case to perform this analysis. The nomenclature *sg-LUT* and *ug-LUT* is used hereinafter to refer to the structured-based and the unstructured-based LUT methods, respectively.

4.3.1 Structured-grid LuT algorithm — *sg-LUT*

The structured grid LuT (*sg-LUT*) implementation features the same interpolation method of *ug-LUT*. The thermodynamic query vectors, for the CFD application considered, are: (P, T) , (P, ρ) , (P, s) , (ρ, T) , (h, s) . By selecting the thermodynamic mesh as a function of pressure and density (Fig. 4.11), the searching algorithm is based on simple binary search for (P, T) , (P, ρ) , (P, s) , (ρ, T) , because they have at least one common input with respect to the thermodynamic mesh. A *kd-tree* is used for the (h, s) pair. Fig. 4.11 shows an example of both structured and unstructured mesh of the thermodynamic region of interest, generated using the same number of mesh nodes.

4.3.2 Comparison *sg-LUT* vs. *ug-LUT*

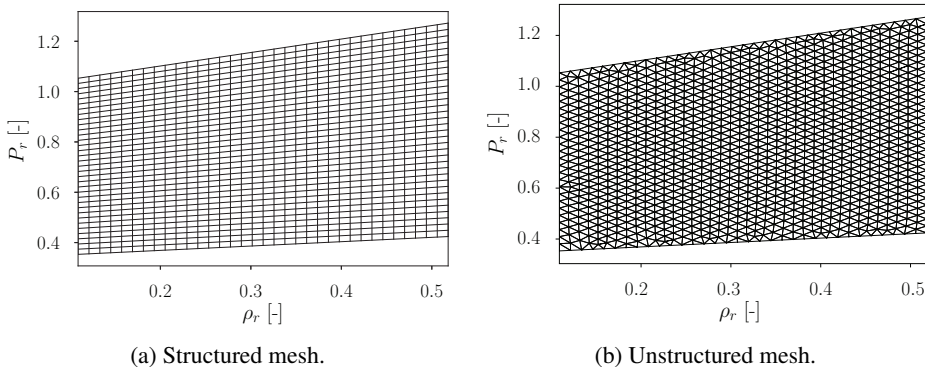


Figure 4.11: Mesh of the thermodynamic region of interest for the *LS89* turbine cascade test case (a) Example of structured mesh used for *sg-LUT*. (b) Example of unstructured mesh used for *ug-LUT*.

Figs. 4.12a and 4.12b report the normalized CPU time associated with the *sg-LUTsim* and *ug-LUTsim*. The total time includes both the LuT pre-processing and the total CFD solver iteration time. As can be noticed (Fig. 4.12b), the pre-processing time becomes a relevant fraction of the total time for *ug-LUT* as opposed to *sg-LUT*. This is due to the

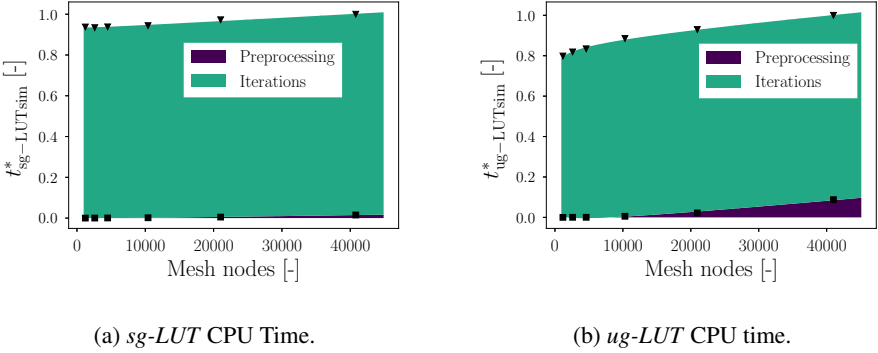


Figure 4.12: Normalized pre-processing and CFD iterations computational time as a function of the thermodynamic mesh nodes. The maximum total CPU time relative to each algorithm is used as reference value. (a) Computational time of the *sg*-LUT algorithm. (b) Computational time of the *ug*-LUT algorithm.

trapezoidal map generation for each thermodynamic input pair. This operation is done just once for *sg*-LUT, when creating the *kd-tree* relative to the (h, s) input pair.

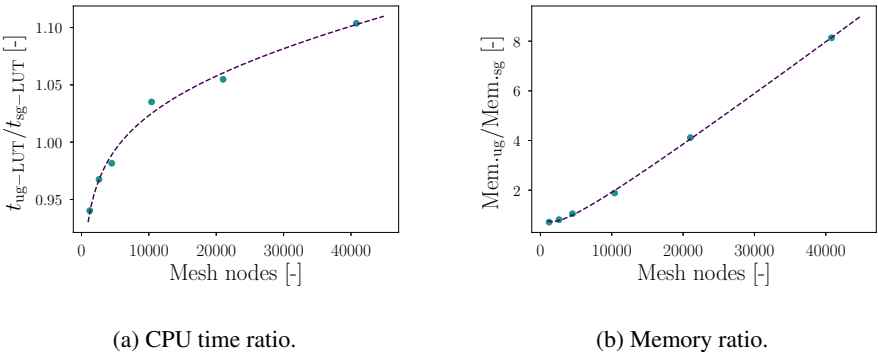


Figure 4.13: Total CPU time and memory ratio between *ug*-LUT and *sg*-LUT. (a) Computational time ratio. (b) Memory requirements ratio.

The ratio between the total simulation time obtained by *ug*-LUT and *sg*-LUT (Fig. 4.13a) indicates that *ug*-LUT is faster than *sg*-LUT, for thermodynamic meshes that are approximately composed by a number of mesh nodes lower than 10,000. The *sg*-LUT is about 5% faster than *ug*-LUT for 25,000 thermodynamic mesh nodes. The *ug*-LUT performance is in agreement with the computational cost of LuT based on quad-tree data structures, whose computational cost has been found to be 10% higher than equally-spaced structured tabulation methods [13]. Fig. 4.13b shows the comparison between the mem-

ory requirements of *ug-LUT* and *sg-LUT*. The *ug-LUT* memory requirements are higher than *sg-LUT* mainly due to the following reasons: i) in *ug-LUT* the trapezoidal maps are created for all the thermodynamic input pairs; ii) for *ug-LUT* the unstructured-mesh connectivity has to be stored. For practical applications, however, since thermodynamic meshes featuring around 10,000 elements are deemed sufficient for the required level of accuracy, the absolute memory associated never exceeded 200Mb. Furthermore, for problems discretized on large domains both the pre-processing computational cost and the memory burden are expected to be a negligible fraction when compared with the CPU time and memory requirements of the CFD simulation.

Finally, a comparative assessment of the RMSE with respect to the *SWsim* is carried out for both *ug-LUT* and *sg-LUT*. Fig. 4.14 depicts the ratio between the RMSE obtained by *ug-LUT* and *sg-LUT* relative to the conservative variables ρ , ρv_1 , ρv_2 , ρe (Fig. 4.14a), Pressure and Temperature (Fig. 4.14b). The RMSE is calculated, as shown in Sec. 5.3, with respect to *SWsim*. The *ug-LUT* algorithm is more accurate than *sg-LUT*, for the fluxes ρv_1 , ρv_2 , ρe and the pressure while the opposite occurs with regard to the density and temperature. Without being exhaustive, these results indicate that unstructured tabular methods may be advantageous when it comes to accuracy as compared to structured grids characterized by the same number of nodes and level of refinement.

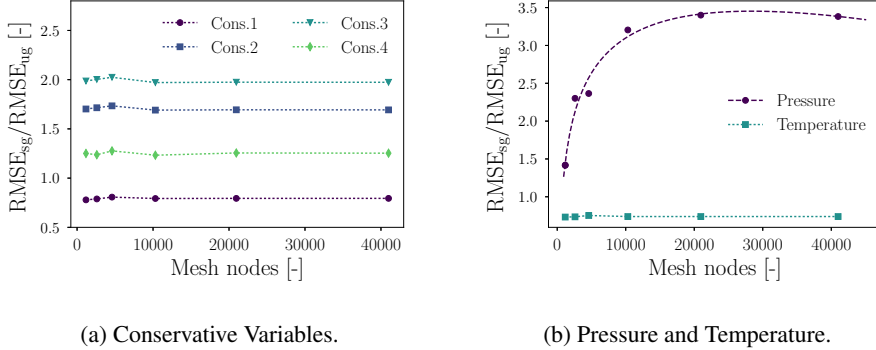


Figure 4.14: Relative Mean Square error ratio between *sg-LUT* and *ug-LUT*. (a) RMSE ratio of the conservative variables. (b) RMSE ratio of pressure and temperature.

4.4 Conclusions

This paper documents the *ug-LUT* method, a novel look-up table method that can be used to improve the computational performance in non-ideal compressible fluid dynamics (NICFD) simulations. The method is based on an unstructured mesh in combination with a trapezoidal-map searching algorithm and a piece-wise interpolation method based on the duality approach. The algorithm was successfully implemented in the open-source code

SU2 and its performance assessed in three paradigmatic NICFD cases: 1) an inviscid 2D supersonic nozzle; 2) a 2D RANS transonic turbine cascade; 3) a 3D RANS supersonic stator row. In all cases, the thermodynamic property model of reference is based on a multi-parameter technical equation of state.

The outcome of this study can be summarized as follows:

- The *ug-LUT* method provides a computational cost reduction compared to simulations in which properties are calculated directly by means of an external fluid property library of approximately one order of magnitude for RANS computations, whereas it is twice less expensive in case of inviscid simulations.
- The accuracy level was found to be satisfactory ($RMSE < 0.01\%$) for engineering applications, with a simple linear interpolation and a relatively coarse thermodynamic grid (of the order of 10 000 elements).
- The method is very efficient for flow simulations involving mixtures as working fluids, for which direct calculation of fluid properties might be prohibitive. The relative computational gain is in this case five times higher if compared to simulations involving pure fluids.
- *ug-LUT* can be regarded as an alternative algorithm to structured LuT methods, providing the possibility of using mesh refinement and featuring comparable performance and accuracy.

Current work is focused on extending the *ug-LUT* method to enable automatic differentiation of the LuT for adjoint-based shape optimization of NICFD problems and to allow its use in other demanding simulations, like dynamic system simulations of energy conversion systems.

Appendix A

Here the pseudo-codes of the algorithms used for the Trapezoidal Map are reported.

Algorithm 1 Build Trapezoidal Map is

```

1: input: list of unique edges:  $Edges$ ;
2:           list of edge to face connectivities:  $EdgeToFace$ ;
3:           list of the  $x$ -coordinates of the edges:  $x_{samples}$ ;
4:           list of the  $y$ -coordinates of the edges:  $y_{samples}$ ;
5: output: list of unique  $x$  bands through which to search:  $X_{Bands}$ ;
6:           list of connectivity of edges to a given unique  $x$ -band (order by  $y$ -value of edge at middle of band):  $Y_{WithinBands}$ ;
7: Filter out vertical edges from  $x_{samples}$  creating unique list:  $X_{Bands}$ ;
8: for each band  $b$  in  $X_{Bands}$  do
9:   for each edge  $e$  in  $Edges$  do
10:    if  $e$  intersects  $b$  then Add  $e$  to  $Y_{WithinBands}$ 
11:    end if
12:   end for
13:   Sort the edges in  $Y_{WithinBands}$  according to the  $y$  value of the edge in the center of the band
14: end for
15: return:  $X_{Bands}$ ,  $Y_{WithinBands}$ ;

```

Algorithm 2 Search Trapezoidal Map is

- 1: **input:** 2D query point (what to search for): x, y ;
 - 2: list of edge to face connectivities: $EdgeToFace$;
 - 3: list of unique x bands through which to search: X_{Bands} ;
 - 4: list of connectivity of edges to a given unique x -band (ordered by y -value of edge at middle of band): $Y_{WithinBands}$;
 - 5: **output:** the index of the face in which the query point lies: CF ;
 - 6:
 - 7: Use binary search to find band b in X_{Bands} which contains x ;
 - 8: Within band b use a binary search to find edge e_1 (below the query point) and e_2 (above the query point);
 - 9: Use interpolation to check if edge is below or above the query point;
 - 10: The containing face CF is given by the intersection of the edge to face connectivities of e_1 and e_2 ;
 - 11: **return:** CF ;
-

References

- [1] Colonna, P., Casati, E., Trapp, C., Mathijssen, T., Larjola, J., Turunen-Saaresti, T., and Uusitalo, A., 2015. “Organic rankine cycle power systems: from the concept to current technology, applications, and an outlook to the future”. *Journal of Engineering for Gas Turbines and Power*, **137**(10), p. 100801.
- [2] Kim, Y., Kim, C., and Favrat, D., 2012. “Transcritical or supercritical CO₂ cycles using both low-and high-temperature heat sources”. *Energy*, **43**(1), pp. 402–415.
- [3] Ahamed, J., Saidur, R., and Masjuki, H., 2011. “A review on exergy analysis of vapor compression refrigeration system”. *Renewable and Sustainable Energy Reviews*, **15**(3), pp. 1593–1600.
- [4] Brown, B. P., and Argrow, B. M., 2000. “Application of Bethe-Zel'dovich-Thompson fluids in organic Rankine cycle engines”. *Journal of Propulsion and Power*, **16**(6), pp. 1118–1124.
- [5] Colonna, P., Nannan, N., Guardone, A., and Van der Stelt, T., 2009. “On the computation of the fundamental derivative of gas dynamics using equations of state”. *Fluid Phase Equilibria*, **286**(1), pp. 43–54.
- [6] , 2017. “1st International Seminar on Non-Ideal Compressible-Fluid Dynamics for Propulsion & Power”. p. 011001.
- [7] Bahamonde, S., Pini, M., De Servi, C., Rubino, A., and Colonna, P., 2017. “Method for the preliminary fluid dynamic design of high-temperature mini-organic rankine cycle turbines”. *Journal of Engineering for Gas Turbines and Power*, **139**(8), p. 082606.
- [8] Pini, M., Persico, G., Pasquale, D., and Rebay, S., 2015. “Adjoint method for shape optimization in real-gas flow applications”. *Journal of Engineering for Gas Turbines and Power*, **137**(3), p. 032604.
- [9] Pini, M., Spinelli, a., Persico, G., and Rebay, S., 2015. “Consistent look-up table interpolation method for real-gas flow simulations”. *Computers & Fluids*, **107**, Jan., pp. 178–188.
- [10] Boncinelli, P., Rubechini, F., Arnone, A., Cecconi, M., and Cortese, C., 2004. “Real gas effects in turbomachinery flows: A computational fluid dynamics model for fast computations”. *Journal of Turbomachinery*, **126**(2), pp. 268–276.

- [11] Dumbser, M., Iben, U., and Munz, C.-D., 2013. “Efficient implementation of high order unstructured weno schemes for cavitating flows”. *Computers & Fluids*, **86**, pp. 141–168.
- [12] De Lorenzo, M., Lafon, P., Di Matteo, M., Pelanti, M., Seynhaeve, J.-M., and Bartosiewicz, Y., 2017. “Homogeneous two-phase flow models and accurate steam-water table look-up method for fast transient simulations”. *International Journal of Multiphase Flow*.
- [13] Xia, G., Li, D., and Merkle, C. L., 2007. “Consistent properties reconstruction on adaptive cartesian meshes for complex fluids computations”. *Journal of Computational Physics*, **225**(1), pp. 1175–1197.
- [14] Wilhelmsen, Ø., Aasen, A., Skaugen, G., Aursand, P., Austegard, A., Aursand, E., Gjennestad, M. A., Lund, H., Linga, G., and Hammer, M., 2017. “Thermodynamic modeling with equations of state: present challenges with established methods”. *Industrial & Engineering Chemistry Research*, **56**(13), pp. 3503–3515.
- [15] Yiu, K., Greaves, D., Cruz, S., Saalehi, A., and Borthwick, A., 1996. “Quadtree grid generation: information handling, boundary fitting and cfd applications”. *Computers & Fluids*, **25**(8), pp. 759–769.
- [16] Palacios, F., Alonso, J., Duraisamy, K., Colonno, M., Hicken, J., Aranake, A., Campos, A., Copeland, S., Economou, T., Lonkar, A., et al., 2013. “Stanford University Unstructured (SU2): an open-source integrated computational environment for multi-physics simulation and design”. In 51st AIAA Aerospace Sciences Meeting Including the New Horizons Forum and Aerospace Exposition, p. 287.
- [17] Economou, T. D., Palacios, F., Copeland, S. R., Lukaczyk, T. W., and Alonso, J. J., 2015. “SU2: An Open-Source Suite for Multiphysics Simulation and Design”. *AIAA Journal*, **54**(3), pp. 828–846.
- [18] Pini, M., Vitale, S., Colonna, P., Gori, G., Guardone, A., Economou, T., Alonso, J., and Palacios, F., 2017. “Su2: the open-source software for non-ideal compressible flows”. In *Journal of Physics: Conference Series*, Vol. 821, IOP Publishing, p. 012013.
- [19] Ghidoni, A., Pelizzari, E., Rebay, S., and Selmin, V., 2006. “3D anisotropic unstructured grid generation”. *International journal for numerical methods in fluids*, **51**(9-10), pp. 1097–1115.
- [20] Colonna, P., and Van der Stelt, T., 2004. “Fluidprop: a program for the estimation of thermo physical properties of fluids”. *Energy Technology Section, Delft University of Technology, Delft, The Netherlands*, <http://www.FluidProp.com>.
- [21] Colonna, P., Nannan, N., Guardone, A., and Lemmon, E. W., 2006. “Multiparameter equations of state for selected siloxanes”. *Fluid Phase Equilibria*, **244**(2), pp. 193–211.

-
- [22] De Berg, M., Van Kreveld, M., Overmars, M., and Schwarzkopf, O. C., 2000. “Computational geometry”. In *Computational geometry*. Springer, pp. 1–17.
 - [23] Giles, M. B., and Pierce, N. A., 2000. “An introduction to the adjoint approach to design”. *Flow, Turbulence and Combustion*, **65**(3), Dec, pp. 393–415.
 - [24] Vitale, S., Gori, G., Pini, M., Guardone, A., Economou, T. D., Palacios, F., Alonso, J. J., and Colonna, P., 2015. “Extension of the su2 open source cfd code to the simulation of turbulent flows of fluids modelled with complex thermophysical laws”. In 22nd AIAA Computational Fluid Dynamics Conference, p. 2760.
 - [25] Vinokur, M., and Montagné, J.-L., 1990. “Generalized flux-vector splitting and roe average for an equilibrium real gas”. *Journal of Computational Physics*, **89**(2), pp. 276–300.
 - [26] Van Leer, B., 1979. “Towards the ultimate conservative difference scheme. v. a second-order sequel to godunov’s method”. *Journal of computational Physics*, **32**(1), pp. 101–136.
 - [27] Pini, M., De Servi, C., Burigana, M., Bahamonde, S., Rubino, A., Vitale, S., and Colonna, P., 2017. “Fluid-dynamic design and characterization of a mini-orc turbine for laboratory experiments”. *Energy Procedia*, **129**, pp. 1141–1148.

5

Adjoint-based unsteady optimization of
turbomachinery operating with non-ideal
compressible flows

Abstract *The lack of established optimal design guidelines for turbomachinery operating in the non-ideal flow regime demands for effective and efficient automated design methods. Past research work has focused on gradient-free methods applied to computational fluid dynamic simulations. The application of the adjoint method is a cost-effective alternative as it enables gradient-based optimization irrespective of the number of design variables. This chapter presents the development of a fully-turbulent unsteady adjoint method for the automated design of multi-row turbomachinery operating in the non-ideal flow regime. The method therefore allows the resolution of constrained unsteady fluid dynamic optimization problems, in which the thermodynamic properties of the working fluid need to be modeled by means of complex equations of state. The optimal designs computed with unsteady simulations obtained with the harmonic balance method and a sliding mesh interface are then compared with optimal design computed with steady-state simulations implementing a mixing plane interface. The design sensitivities are successfully verified using second-order finite differences and applied to the optimization of two turbomachinery test cases: i) a turbine cascade subject to time-varying inlet conditions; ii) a turbine stage of an organic Rankine cycle power system. The results demonstrate the importance of computing fluid thermodynamic properties using accurate models for design optimization, and the advantage of optimizing the fluid dynamic shapes by means of unsteady simulations. As a matter of fact, the fluid dynamic performance estimated with such method is better than that obtained with an optimization method based on steady state simulations.*

5.1 Introduction

Turbomachinery components are fundamental in the aviation, automotive, and energy industry, to name a few. Diverse engineering applications require turbomachinery operating with non-ideal compressible fluid flows, i.e., flows of fluids whose thermodynamic properties cannot be modeled according to the ideal gas assumption, but require complex equations of state. Examples of such applications include compressors of supercritical CO₂ power plants, turbines of organic Rankine cycle power systems, compressors for refrigeration systems, and steam turbines [1–4].

For this turbomachinery, the shortage of experimental data and accurate loss models entails an absence of optimal design guidelines, especially for new and unconventional applications. In such cases, a viable solution is to obtain a preliminary design with methods originally developed for conventional turbines and compressors, being aware that the result is bound to be highly sub-optimal. The obtained preliminary design can then be optimized, but it is crucial that the optimization method is capable of taking into account non-ideal compressible fluid dynamic effects. This requirement makes the complexity of the method and the computational effort even more challenging.

In this realm, automated shape optimization methods can be seen as an effective approach to perform the design of unconventional turbomachines. Thanks to the advancements in computational resources, these methods are becoming more and more a viable option, offering the possibility to improve current components performance and to explore

innovative solutions.

Past work in the area of automated shape optimization of turbomachinery operating with non-ideal compressible flows, has focused on both non-deterministic and deterministic methods. Non-deterministic methods have been successfully applied, for example, to the constrained optimization of organic Rankine cycle turbine cascades [5–7]. These methods are robust if dealing with non-smooth objective functions and are suitable for global optimization. However, their computational cost can become prohibitive if a large set of design variables has to be considered and if fluid properties must be evaluated with complex thermodynamic models. Deterministic (gradient-based) algorithms are in general very efficient in converging to optimal solutions, but they require to evaluate the gradients of the objective function. The objective function must, therefore, feature regularity properties and the gradient estimation must be computationally inexpensive. In this respect, adjoint-based algorithms provide an efficient way to compute design gradients for deterministic optimization methods.

Recently, adjoint-based shape optimization methods have been extended to treat also turbomachinery affected by strong non-ideal compressible fluid dynamics (NICFD) effects [8]. These algorithms allow the possibility of performing automated design very efficiently when the number of design variables is much higher than the objective functions or constraints. For this reason, adjoint-based optimization methods are a very attractive, and sometimes necessary, alternative to non-deterministic algorithms for CFD-based turbomachinery design.

To date, however, adjoint-based turbomachinery optimization involving non-ideal compressible flows has been only successfully applied to single cascades and assuming the flow stationary [9, 10]. In the very recent past, the method has been extended to the optimization of multi-row machines [11]. This chapter documents the application of unsteady adjoint-based automated design to turbomachinery operating in the non-ideal flow regime. The method, implemented in the open-source code *SU2* [12, 13], is based on the harmonic balance (HB) method and the use of complex equations of state. The thermo-physical properties of the fluid are computed either employing a cubic equation of state model coded in *SU2*, or by using data from tables generated with an external fluid property library [14], as described in Chap. 4.

The method is first applied to the computation and verification of the design sensitivities of a turbine cascade, in order to test its capabilities and validity. Subsequently, to demonstrate its potential in a realistic case, the constrained shape optimization of an organic Rankine cycle turbine stage is performed.

5.2 Method

In analogy with the treatment of Chap.3, the Navier-Stokes equations can be discretized as

$$\left(\frac{\Omega I}{\Delta \tau} + J \right) \Delta U_n = -\widehat{\mathcal{R}}_n(U^q), \quad n = 0, 1, \dots, N - 1. \quad (5.1)$$

in which

$$\widehat{\mathcal{R}}_n(\mathbf{U}^q) = \mathcal{R}_n(\mathbf{U}^q) + \Omega \sum_{i=0}^{N-1} H_{n,i} \Delta \mathbf{U}_i + \Omega \sum_{i=0}^{N-1} H_{n,i} \mathbf{U}_i^q. \quad (5.2)$$

In (5.2), \mathbf{H} is the harmonic balance operator, calculated for a known set of K input frequencies and corresponding to $N = 2K + 1$ time instances. \mathbf{U} indicates here the vector of conservative variables and includes both laminar and turbulent quantities. More details on the flow solver method can be found in Chap. 2.

5.2.1 Fully-turbulent discrete adjoint and non-ideal compressible flows

The adjoint equations are derived by making explicit the dependence of the vector of conservative variables \mathbf{U} from the vector of primitive variables $\Theta = \rho, e, \mathbf{u}$, where \mathbf{u} is the velocity vector. The vector of turbulent quantities is herein omitted for simplicity. Note that the computation of the laminar part of \mathbf{U} from Θ requires the calculation of the primary and secondary thermodynamic variables through an equation of state model. This explicit dependence allows one to outline the additional sensitivities arising in the gradient equation for non-ideal compressible flows that can only be computed by differentiating a complex thermodynamic model or tabulation method.

Application of the fixed-point iteration method to (5.1) results in

$$\mathbf{U}_{z,n}^{q+1} = \mathcal{G}_{z,n}(\mathbf{U}^q), \quad (5.3)$$

in which $\mathbf{U}_{z,n}$ and $\mathcal{G}_{z,n}$ are the vector of conservative variables and the iteration operator of the pseudo time-stepping relative to the physical zone z and for time instance n . Each physical zone z corresponds to a blade row.

Making explicit the dependence of $\mathbf{U}_{z,n}$ from the set of design variables α_z and the thermodynamic model Θ , the optimization problem can be written as

$$\begin{aligned} & \underset{\alpha_z}{\text{minimize}} \quad \mathcal{J}(\mathbf{U}(\alpha_z, \Theta), X(\alpha_z)) \\ & \text{subject to} \quad \mathbf{U}_{z,n}(\alpha_z, \Theta) = \mathcal{G}_{z,n}(\mathbf{U}(\alpha_z, \Theta), X_{z,n}(\alpha_z)), \quad n = 0, 1, \dots, N - 1 \quad z = 0, 1, \dots, Z - 1 \\ & \quad X_{z,0}(\alpha_z) = \mathcal{M}_z(\alpha_z). \end{aligned} \quad (5.4)$$

\mathcal{J} is a generic objective function, $X_{z,n}$ is the physical grid, and \mathcal{M}_z is a differentiable function representing the mesh deformation algorithm. The objective function \mathcal{J} , as shown in Chap. 3, is computed as a time average by applying Fourier interpolation of the resolved time instances.

The Lagrangian of the optimization problem is

$$\mathcal{L} = \mathcal{J} + \sum_{z=0}^{Z-1} \sum_{n=0}^{N-1} ((\mathcal{G}_{z,n}(\mathbf{U}(\alpha_z, \Theta), X_{z,n}(\alpha_z)) - \mathbf{U}_{z,n}(\alpha_z, \Theta))^T \lambda_{z,n}) + (\mathcal{M}_z(\alpha_z) - X_{z,0}(\alpha_z))^T \mu_z,$$

(5.5)

with λ and μ being the adjoint variables. The differential of the Lagrangian is

$$\begin{aligned} d\mathcal{L} = & \sum_{z=0}^{Z-1} \sum_{n=0}^{N-1} \left(\frac{\partial \Theta_{z,n}}{\partial \mathbf{U}_{z,n}}^\top \frac{\partial \mathcal{J}}{\partial \Theta_{z,n}}^\top + \sum_{i=0}^{Z-1} \sum_{j=0}^{N-1} \frac{\partial \Theta_{z,n}}{\partial \mathbf{U}_{z,n}}^\top \frac{\partial \mathcal{G}_{i,j}}{\partial \Theta_{i,j}}^\top \lambda_{i,j} - \lambda_{z,n} \right) d\mathbf{U}_{z,n} + \\ & \sum_{z=0}^{Z-1} \sum_{n=0}^{N-1} \left(\frac{\partial \mathcal{J}}{\partial X_{z,n}}^\top + \frac{\partial \mathcal{G}_{z,n}}{\partial X_{z,n}}^\top \lambda_{z,n} \right) dX_{z,n} - \mu_z dX_{z,0} + \\ & \sum_{z=0}^{Z-1} \frac{\partial \mathcal{M}_z}{\partial \alpha_z}^\top \mu_z d\alpha_z, \end{aligned} \quad (5.6)$$

from which the adjoint equations can be derived as

$$\frac{\partial \Theta_{z,n}}{\partial \mathbf{U}_{z,n}}^\top \frac{\partial \mathcal{J}}{\partial \Theta_{z,n}}^\top + \sum_{i=0}^{Z-1} \sum_{j=0}^{N-1} \frac{\partial \Theta_{z,n}}{\partial \mathbf{U}_{z,n}}^\top \frac{\partial \mathcal{G}_{i,j}}{\partial \Theta_{i,j}}^\top \lambda_{i,j} = \lambda_{z,n}, \quad (5.7)$$

and

$$\frac{\partial \mathcal{J}}{\partial X_{z,n}}^\top + \frac{\partial \mathcal{G}_{z,n}}{\partial X_{z,n}}^\top \lambda_{z,n} = \mu_z. \quad (5.8)$$

μ_z is directly computed from (5.8) given the solution λ_{zn} of (5.7). In analogy to the flow solver, (5.7) can be expressed as a fixed-point iteration in λ_{zn}

$$\lambda_{z,n}^{q+1} = \frac{\partial \mathcal{N}}{\partial \mathbf{U}_{z,n}}(\mathbf{U}_{z,n}^*, \lambda^q, X_{z,n}), \quad (5.9)$$

where \mathbf{U}_n^* is the solution of (5.3) and \mathcal{N} is the shifted Lagrangian defined as

$$\mathcal{N} = \mathcal{J} + \sum_{z=0}^{Z-1} \sum_{n=0}^{N-1} \mathcal{G}_{z,n}^\top(\mathbf{U}, X_{z,n}) \lambda_{z,n}. \quad (5.10)$$

The gradient of the objective function \mathcal{J} with respect to the vector of the design variables α_z can be computed, for each numerical zone, from the converged flow and adjoint solutions using

$$\frac{d\mathcal{L}^\top}{d\alpha_z} = \frac{d\mathcal{J}^\top}{d\alpha_z} = \frac{\partial \mathcal{M}_z^\top(\alpha_z)}{\partial \alpha_z} \mu_z \quad z = 0, 1, \dots, Z-1. \quad (5.11)$$

Figure 5.1 reports a schematic representation summarizing the design chain procedure. In this work, the term $\frac{\partial \Theta}{\partial \mathbf{U}}$ contains the derivation of the tabulation (look-up table) method. All the derivatives needed to solve (5.9) are obtained by means of Algorithmic Differentiation (AD). As opposed to the approach documented in [9], the reverse mode of the open-source

AD tool CoDiPack [15] is used in this work to linearize the primal solver along with the equation of state model in a fully black-box manner. For turbomachinery design problems in which fluid-dynamic losses are to be minimized, the objective function \mathcal{J} is usually expressed as entropy generation or total pressure loss coefficient. The former is used in this work.

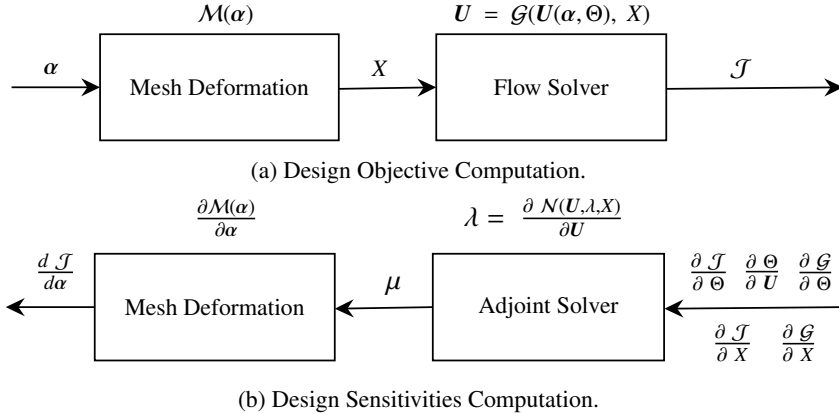


Figure 5.1: Schematic representation of the design problem.

5.3 Adjoint-based optimization using *ug-LUT*

The adjoint-based gradients of the entropy generation are computed for the turbine cascade described in Chap. 4, using the same boundary conditions, working fluid (MM), numerical schemes, and mesh. Differently from Chap. 4, a time-varying total pressure, \tilde{P}_{tot} , is imposed at the inlet of the cascade according to

$$\tilde{P}_{tot} = P_{tot}[1 + A \sin(2\pi t^*)], \quad (5.12)$$

in which $A = 0.03$ and $t^* = t/T_0$. The shape optimization is performed using the HB method proposed in Chap. 2 in combination with the Look-up Table method (*ug-LUT*) presented in Chap. 4. Figure 5.2 shows the free-form deformation (FFD) box adopted for the turbine blade and α , i.e, the corresponding set of 12 design variables (DVs). In order to quantify the unsteady fluid dynamic performance of the stator, the dimensionless entropy generated in the flow passage of the stator is considered and calculated as

$$s_{\text{gen}} = \frac{\langle s_{\text{out}} \rangle - \langle s_{\text{in}} \rangle}{v_0^2/T_{0,\text{in}}} . \quad (5.13)$$

Here, $\langle s_{\text{out}} \rangle$ and $\langle s_{\text{in}} \rangle$ are the outlet and inlet entropy averaged over the respective boundaries using the mixed-out procedure [16]. v_0 is the spout velocity and $T_{0,\text{in}}$ the inlet total

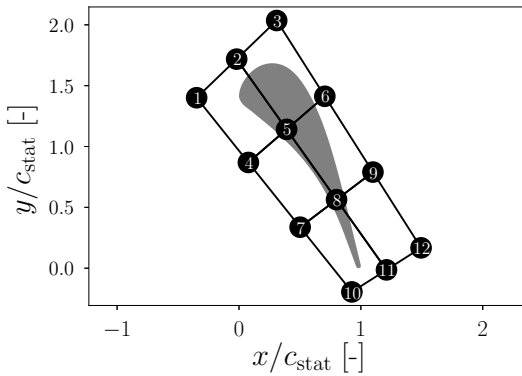


Figure 5.2: LS-89 turbine cascade blade geometry, FFD box and design variables.

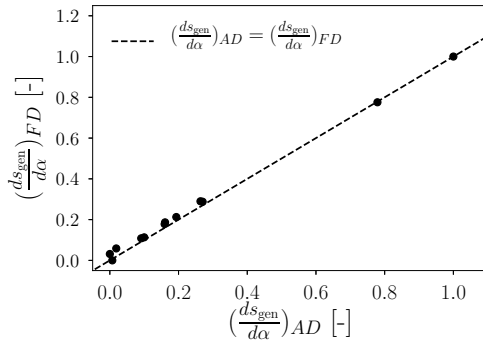


Figure 5.3: Adjoint-based (AD) vs second order finite differences (FD) design gradients.

temperature. All the single quantities used in (5.13) are computed as the time-averaged values of for the resolved time instances.

In this chapter, the adjoint-based gradients obtained from the simulations in which the fluid properties are computed using the *ug-LUT* method are denoted for simplicity as *LUT*. The tabulated thermodynamic properties were computed through a model based on an equation of state in the *Span-Wagner* functional form. Furthermore, *LUT-AD* and *LUT-FD* refer to the sensitivities calculated using the adjoint method and finite differences respectively. In order to verify the results, the adjoint-based design gradients are compared with those obtained by employing second-order accurate finite differences (Fig. 5.3). The root mean square error (RMSE) between the gradients from *LUT-AD* and *LUT-FD* is approximately 0.021.

Figure 5.4 displays the gradients with respect to the design variables obtained from

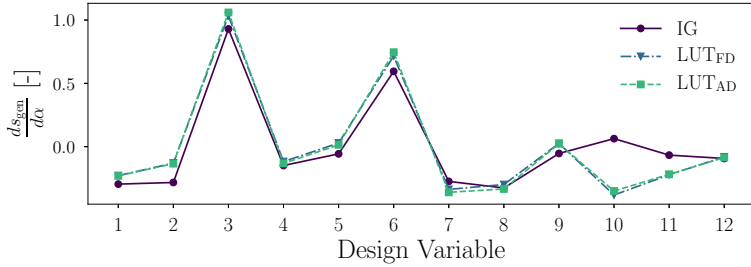


Figure 5.4: Entropy generation gradients relative to the FFD box design variables (Fig. 5.2) obtained from *LUT-AD*, *LUT-FD*, and *IG*.

LUT-AD and *LUT-FD*, relative to the DVs reported in Fig. 5.2. Moreover, it reports the adjoint-based gradients from the simulation in which the ideal gas equation of state is adopted to model the fluid properties (*IG*). The relative difference of the values calculated with *LUT* and those calculated with *IG* of the gradients is in excess of 20% for most DVs (Fig. 5.5) and up to 110% for the DVs located in proximity of the blade trailing edge (Fig. 5.4).

The verified adjoint-based gradients are finally used to perform the constrained shape optimization of the illustrative transonic turbine cascade. The selected gradient-based optimization algorithm is the modified version of the nonlinear least-squares method (SLSQP) [17].

The constrained optimization problem is formulated as

$$\begin{aligned} & \underset{\alpha}{\text{minimize}} \quad s_{\text{gen}}(\alpha), \\ & \text{subject to: } \beta_{\text{out}} = \beta_{\text{out},0}, \end{aligned} \tag{5.14}$$

in which β_{out} is the outlet flow angle with the correspondent constrained nominal value $\beta_{\text{out},0}$. The results of the blade shape optimizations are termed *LUT* if fluid properties are obtained from look-up tables and *PR* if properties are calculated with the *Peng Robinson* model implemented in *SU2*. Figure 5.7 shows the optimized shapes highlighting, therefore, the differences. The convergence to the optimal solution of the constrained optimization problem is reached in 10 iterations, and the final results are summarized in Tab. 5.1. The results reported in Tab. 5.1 relative to the *PR*-based optimization are computed by running *LUT* and using the optimized shape from *PR*. The *LUT*-based design leads to a decrease in entropy generation by approximately 19.2%, whereas a decrease by about 12.0% if *PR* is used. For both optimizations, the constraint is met by a deviation below 0.05% with respect to the baseline outlet flow angle. Figure 5.6 reports the loss breakdown in terms of the kinetic energy loss coefficient of the cascade, computed according to the procedure indicated in Ref. [18]. The optimization based on *LUT* results in lower trailing edge losses and comparable boundary layer loss if compared to the *PR*-based design, thus resulting in overall better fluid dynamic performance. Figure 5.8 shows the

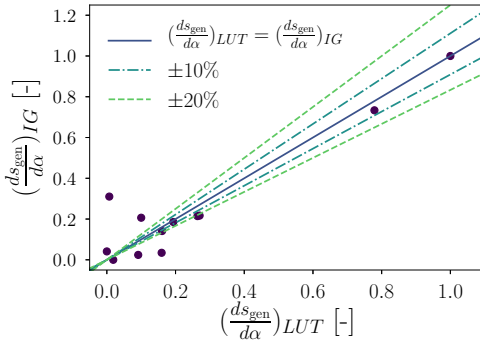


Figure 5.5: Adjoint-based vs second order finite differences design gradients.

Mach number contours obtained from simulations of the flow around the baseline, *LUT*, and *PR* geometries.

These results show that the use of an accurate equation of state is essential to optimize turbine cascades operating in the non-ideal flow regime as this can enable a considerable attenuation of loss mechanisms occurring when the flow already reached ideal gas states. Regarding the computational cost, the comparison of blade-shape optimizations described here confirm the advantage of evaluating fluid thermophysical properties with a look-up table algorithm outlined in Chap.4 (Fig.4.10).

Table 5.1: *LS89* turbine cascade optimization results.

	Baseline	<i>PR</i> Opt.	<i>LUT</i> Opt.
s_{gen} [-]	0.020	0.018	0.017
β_{out} [°]	74.86	74.88	74.89
δs_{gen} [-]	0.00 %	-12.0 %	-19.2 %
$\delta \beta_{\text{out}}$ [-]	0.00 %	+0.03 %	+0.04 %

5.4 Shape optimization of an axial ORC turbine stage

The test case described here represents an exemplary stage encountered in organic Rankine cycle (ORC) turbines, operating in the non-ideal compressible fluid dynamic regime. The constrained shape optimization problem of the axial stage depicted in Fig. 5.11 is performed according to the following formulation

$$\begin{aligned} & \underset{\alpha_i}{\text{minimize}} \quad s_{\text{gen}}(\alpha_i), \quad i = 1, 2 \\ & \text{subject to: } P^* > P_0^*, \end{aligned} \tag{5.15}$$

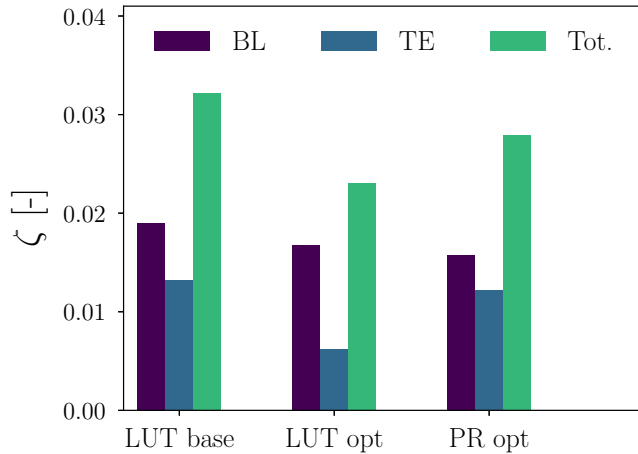


Figure 5.6: Fluid dynamics loss breakdown in terms of the dimensionless kinetic energy loss coefficient ζ . BL refers to the boundary layer, TE to the trailing edge and Tot. to the total loss of the cascade. *LUT base* refers to the results obtained using *ug-LUT* for the baseline geometry; *LUT opt* and *PR opt* refer to the results from the *LUT*-based and the *PR*-based optimizations.

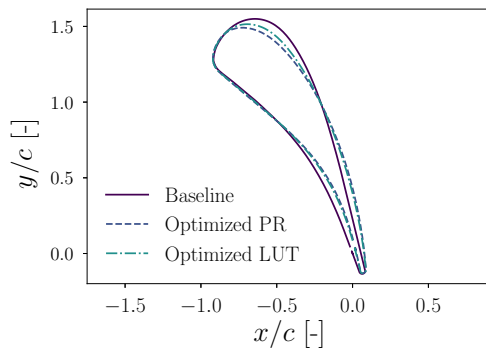


Figure 5.7: Shape optimization results for the *ls89* cascade, obtained from *IG*, *PR*, and *LUT*.

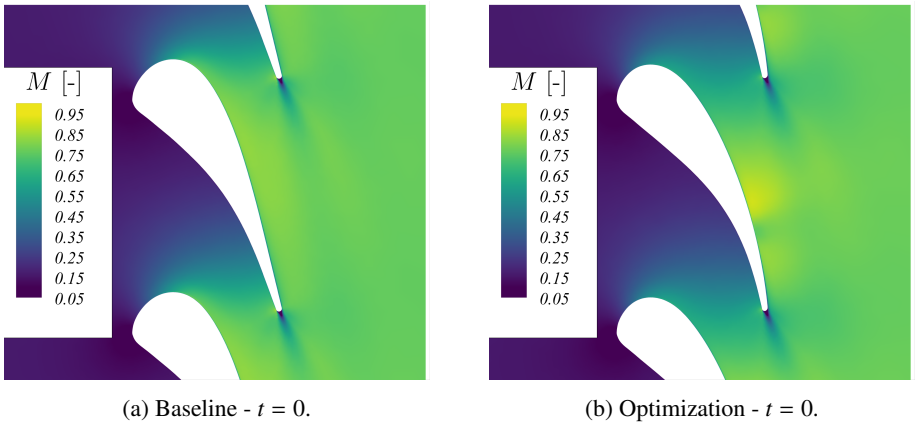


Figure 5.8: Mach number contours plot obtained from the *LUT* simulations using the baseline and optimized blade profiles.

in which P^* is the dimensionless power of the stage defined as

$$P^* = \frac{w \dot{m}}{\rho_{0,\text{in}} y_p u_b^3}. \quad (5.16)$$

Here, w is the specific work, \dot{m} the mass flow rate based on the blade pitch y_p , $\rho_{0,\text{in}}$ the total density at the stage inlet, and u_b the blade speed. Table 5.2 reports the main simulation parameters. A hybrid structured-unstructured mesh of approximately 70 000 grid elements is adopted to guarantee a value of $y^+ \approx 1$ and the solution independence from the number of elements. A second-order accurate Roe scheme [19] is used in combination with the MUSCL approach and gradient limitation. The HB-based simulation results are computed for one single input frequency, i.e., the blade passage frequency. A study on the influence of a higher number of harmonics is suggested as future work. The current implementation of the *ug-LUT* algorithm in *SU2* does not yet allow the shape optimization of multi-row turbomachinery. Due to this limitation, in this section, the optimizations are based on *PR*.

The design variables are the 84 control points of the FFD boxes highlighted in Fig. 5.10. Figure 5.9 shows the optimization evolution of the dimensionless entropy generation and power. Additionally, in Fig. 5.9, the results from a steady state optimization in which the blade-row interface is modeled by means of the mixing-plane (MP) method are reported. Figure 5.11 depicts the baseline and the optimized blade shapes resulting from both the steady and the unsteady-based optimization. The HB-based optimization leads to a reduction in the computed entropy generation by 4.2% whereas for the MP-based optimization a decrease by 5.2% is observed. However, if the MP-based optimized blade profiles are employed in a HB simulation, the decrease in entropy is approximately 1.2%. Furthermore, the HB-based optimization leads to a power output higher by 5.4% if compared to the MP-based optimization results. From these findings, it can be inferred that the use

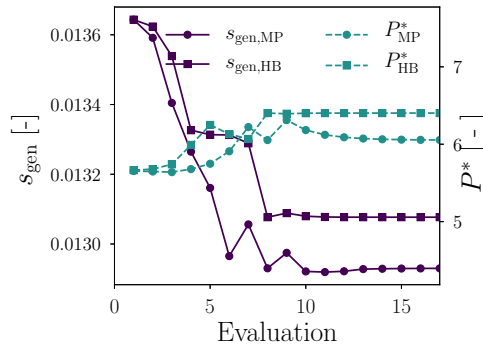


Figure 5.9: ORC axial stage optimization history.

of unsteady automated design methods could provide a step change in the fluid-dynamic performance of unconventional turbomachinery.

Table 5.2: Main simulation parameters of the axial ORC turbine stage.

Parameter	Value	Unit
Total inlet reduced temperature	1.1	[−]
Inlet compressibility factor	0.77	[−]
Expansion ratio	1.5	[−]
Isentropic load coefficient	1.0	[−]
Inlet turbulent intensity	5%	[−]
Turbulent viscosity ratio	100	[−]
Working fluid	R1234yf	

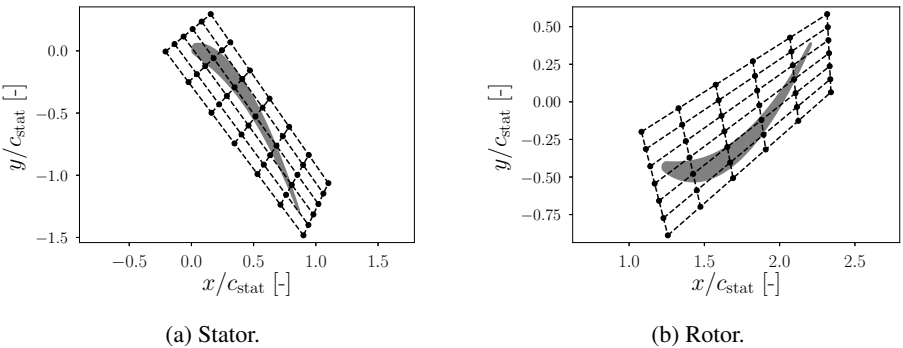


Figure 5.10: Free-form deformation box and design variables.

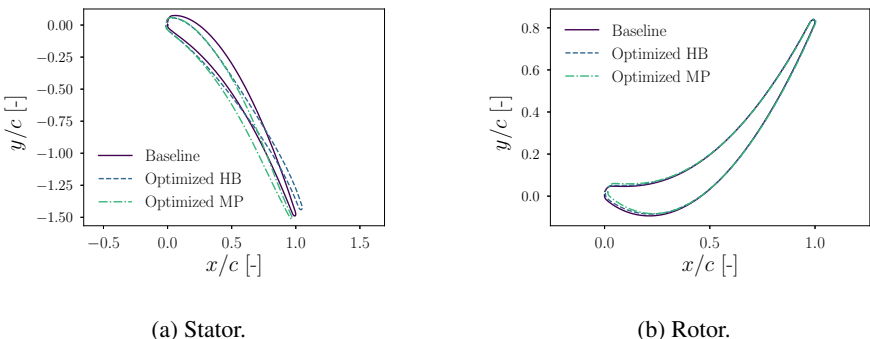


Figure 5.11: Shape optimization for the subsonic test case.

5.5 Conclusions

This chapter documents the application of a fully-turbulent adjoint method to the unsteady design of turbomachinery working in the non-ideal flow regime.

The following conclusions can be drawn.

- The adjoint-based sensitivities based on the harmonic balance(HB) method are accurately computed and verified using second-order finite differences, for non-ideal flow computations. The proposed adjoint method proved to be accurate if complex thermodynamic models are adopted or if the requested thermodynamic properties are computed via tabulation methods.
- The effectiveness of the method was demonstrated by performing a 2D constrained shape optimization of two exemplary turbomachinery test cases operating in the non-ideal flow regime: i) a stator subject to a periodic inlet working condition; ii) a 2-dimensional axial stage of an organic Rankine cycle power system.

- The accuracy of the adopted thermodynamic model has an impact on the optimized blade profiles. In the turbine stator analyzed, the optimization using the thermodynamic model based on an EoS in the Span-Wagner functional form led to approximately 8% higher fluid dynamic performance if compared to the model based on a cubic EoS.
- The combination of the HB-based adjoint and the use of thermodynamic models based on look-up tables enables an efficient multi-row optimization in turbomachinery operating in non-ideal flow conditions.
- The use of the unsteady-based optimization method leads to better calculated fluid dynamic performance if compared with the optimization based on steady state methods. For the ORC turbine stage, the unsteady optimization led to an entropy generation reduction by 4.2% whereas the steady state optimization a decrease by 1.2%.

References

- [1] Colonna, P., Casati, E., Trapp, C., Mathijssen, T., Larjola, J., Turunen-Saaresti, T., and Uusitalo, A., 2015. “Organic rankine cycle power systems: from the concept to current technology, applications, and an outlook to the future”. *Journal of Engineering for Gas Turbines and Power*, **137**(10), p. 100801.
- [2] Kim, Y., Kim, C., and Favrat, D., 2012. “Transcritical or supercritical CO₂ cycles using both low-and high-temperature heat sources”. *Energy*, **43**(1), pp. 402–415.
- [3] Ahamed, J., Saidur, R., and Masjuki, H., 2011. “A review on exergy analysis of vapor compression refrigeration system”. *Renewable and Sustainable Energy Reviews*, **15**(3), pp. 1593–1600.
- [4] Kunick, M., Kretzschmar, H.-J., di Mare, F., and Gampe, U., 2015. “CFD analysis of steam turbines with the IAPWS standard on the spline-based table look-up method (SBTL) for the fast calculation of real fluid properties”. In ASME Turbo Expo 2015: Turbine Technical Conference and Exposition, American Society of Mechanical Engineers. V008T26A037.
- [5] Congedo, P. M., Cinnella, P., and Corre, C., 2009. “Shape optimization for dense gas flows in turbine cascades”. In *Computational Fluid Dynamics 2006*. Springer, pp. 555–560.
- [6] Pasquale, D., Ghidoni, A., and Rebay, S., 2013. “Shape optimization of an organic rankine cycle radial turbine nozzle”. *Journal of Engineering for Gas Turbines and Power*, **135**(4), p. 042308.
- [7] Persico, G., 2017. “Evolutionary optimization of centrifugal nozzles for organic vapours”. In Journal of Physics: Conference Series, Vol. 821, IOP Publishing, p. 012015.
- [8] Vitale, S., Albring, T. A., Pini, M., Gauger, N. R., and Colonna, P. “Fully turbulent discrete adjoint solver for non-ideal compressible flow applications”. *Journal of the Global Power and Propulsion Society*, **1**, pp. 252 – 270.
- [9] Pini, M., Persico, G., Pasquale, D., and Rebay, S., 2015. “Adjoint method for shape optimization in real-gas flow applications”. *Journal of Engineering for Gas Turbines and Power*, **137**(3), p. 032604.

- [10] Vitale, S., Albring, T. A., Pini, M., Gauger, N. R., and Colonna, P., 2017. “Fully turbulent discrete adjoint solver for non-ideal compressible flow applications”. *Journal of the Global Power and Propulsion Society*, **1**, pp. 252 – 270.
- [11] Vitale, S., 2018. “Advancements in automated design methods for NICFD turbomachinery”. PhD thesis, Delft University of Technology.
- [12] Palacios, F., Alonso, J., Duraisamy, K., Colonna, M., Hicken, J., Aranake, A., Campos, A., Copeland, S., Economou, T., Lonkar, A., et al., 2013. “Stanford University Unstructured (SU2): an open-source integrated computational environment for multi-physics simulation and design”. In 51st AIAA Aerospace Sciences Meeting Including the New Horizons Forum and Aerospace Exposition, p. 287.
- [13] Economou, T. D., Palacios, F., Copeland, S. R., Lukaczyk, T. W., and Alonso, J. J., 2015. “SU2: An Open-Source Suite for Multiphysics Simulation and Design”. *AIAA Journal*, **54**(3), pp. 828–846.
- [14] Colonna, P., Van der Stelt, T., and Guardone, A., 2019. “Fluidprop (version 3.1): a program for the estimation of thermo physical properties of fluids”. *A computer program since 2004*.
- [15] Sagebaum, M., Albring, T., and Gauger, N. R., 2017. “High-Performance Derivative Computations using CoDiPack”. *arXiv preprint arXiv:1709.07229*.
- [16] Saxer, A. P., 1992. A numerical analysis of 3-D inviscid stator/rotor interactions using non-reflecting boundary conditions. Tech. rep., Cambridge, Mass.: Gas Turbine Laboratory, Massachusetts Institute of Technology.
- [17] Kraft, D., 1998. A software package for sequential quadratic programming. Tech. rep., DLR German Aerospace Center Institute for Flight Mechanics, Kohn, Germany.
- [18] Mee, D., Baines, N., Oldfield, M., and Dickens, T., 1990. “An examination of the contributions to loss on a transonic turbine blade in cascade”. In ASME 1990: International Gas Turbine and Aeroengine Congress and Exposition, American Society of Mechanical Engineers. V005T16A012.
- [19] Roe, P. L., 1981. “Approximate riemann solvers, parameter vectors, and difference schemes”. *Journal of computational physics*, **43**(2), pp. 357–372.

6

Conclusion

Automated design based on the adjoint method is a computationally efficient solution for constrained shape optimization if the number of design variables is large. For turbomachinery, most of the adjoint-based optimization methods documented in the literature are based on steady state computational fluid dynamic simulations. Because of the inherently unsteady nature of turbomachinery flows, methods that enable unsteady optimization have the potential to improve current design paradigms. Given the currently prohibitive computational cost of employing fully unsteady flow simulations in the optimization process, a procedure for the optimal design of turbomachinery that takes into account the unsteady characteristics of the flow has been obtained by adopting reduced order models.

This dissertation documents research work on reduced order models for the unsteady adjoint-based optimization of turbomachinery. In particular, the work resulted in a new fluid dynamic design optimization framework, implemented in the open-source code *SU2*, based on a harmonic balance discrete adjoint solver. The framework is also capable of accounting for fluid flows affected by non-ideal compressible fluid dynamic effects. Therefore, it is suitable for the design of unconventional turbomachinery like organic Rankine cycle turbines or supercritical CO₂ Brayton cycle compressors.

The main contributions of the investigation can be summarized as follows

- A novel fully-turbulent adjoint solver based on the time-domain harmonic balance method is conceived and developed by using algorithmic differentiation. The solver, based on the duality-preserving method, results in accurate design sensitivities and inherits the convergence properties of the primal flow solver.
- A new tabulation method for thermodynamic properties of fluids based on unstructured grids was implemented and proved to be efficient if compared with tabulation methods based on structured grids. The merits of the tabulation method were successfully tested with fluid dynamic simulations of turbomachinery operating in the non-ideal compressible flow regime.
- The relevance of accurate predictions of fluid thermodynamic properties was also quantified for the solution of optimal design problems related to turbomachinery affected by non-ideal compressible fluid dynamics.
- The unsteady optimization procedure based on the HB method led to the prediction of higher improvements in fluid dynamic performance if compared to the optimizations based on steady state methods with mixing-plane interface.
- The computational efficiency of optimal design calculations employing the adjoint method and unsteady simulations performed with the harmonic balance method is superior to those based on time-accurate simulations. However, if a large number of input frequencies need to be resolved to obtain sufficiently accurate unsteady simulations, the limiting factor becomes the memory requirements.

6.1 Limitations and recommendations

The following main limitations and suggestions are outlined based on the findings of the work presented in this dissertation.

- The current fluid dynamic design optimization framework can only deal with turbomachinery blade rows with equal angular pitch. A phase-shift boundary condition needs to be implemented in order to investigate unsteady effects in multi-stage turbomachinery with different angular pitches.
- Issues related to the high memory usage must be investigated in case the design framework is used for the fluid dynamic optimization of 3D multi-stage turbomachinery.
- The current free-form deformation algorithm adopted as shape deformation method is not suitable for 3D turbomachinery applications. The main issues of this approach are: i) difficulty in meeting the constraints on the end-wall and thus maintaining the desired geometrical continuity properties; ii) lack of correspondence between the design variables and the geometrical characteristic of turbomachinery blades. A parametric representation of the design variables based on computer-aided-design can be regarded as a potential solution to the limitations mentioned above.
- In order to increase the computational efficiency of the primal flow solver, the following improvements shall be undertaken: i) extension of the multi-grid method to the HB solver, including the HB source terms; ii) implementation of a fully-coupled system of equations resolving all the time-instances together. In the current implementation, each time instance is computed separately. In order to solve the fully-coupled system of equations, a suitable preconditioner must be considered for numerical stability.
- The HB method described in this dissertation is limited to the resolution of problems characterized by a known set of discrete frequencies.

6.2 Outlook

The results of the work documented in this thesis open up to the possibility to further expand the work in these directions:

- The development of computationally efficient unsteady methods for turbomachinery design is a key enabler to address multi-disciplinary problems. By leveraging on the current unsteady optimization framework, for example, aero-mechanical design problems can be tackled.

- If the current HB method is extended to deal with an unknown set of input frequencies, a new class of problems can be addressed. A relevant example of a turbomachinery optimization problem, which would require a time-accurate resolution of the flow characteristics, is noise minimization.
- A hybrid time-accurate/HB method can be devised in which the flow solver is based on a time-accurate algorithm whereas the adjoint solver is based on the HB method. In quasi-periodic unsteady problems, this would enable the simultaneous minimization of the memory storage and of the computational cost required by a time-accurate adjoint solver.

Acknowledgements

I am writing these acknowledgments with my heart full of gratitude for all the people I have crossed paths with in my life. This thesis is the result of all these life interactions.

Prof. Colonna, I am thankful for all the support you gave me, but especially for believing in me from the very first moment. Without this trust, I would not have started and pursued my PhD. Thank you also for the scientific freedom and empathy in the difficult moments.

It is difficult to express in words my gratitude to my supervisor, Dr. Pini. Matteo, this journey would not have been possible without you. Your professional attitude, enthusiasm, your scientific knowledge, and critical mindset, have been an essential component towards the realization of this work. I have learned a lot from you. The time we spent together has been an unqualified delight. Thanks for being there when I really needed it, and thanks for your kindness.

Additionally, I would like to thank the doctoral examination committee for their commitment, interest, and feedback on my research.

During the years of my PhD I had the privilege to work with a fantastic group of colleagues, of friends. We have shared great moments that are now part of my life. I want to acknowledge the contribution of the open-source community of *SU2* and in particular thanks to Tim, Tom, Sravya, Edwin, Ruben, and Giulio. Thanks to prof. Juan Alonso for hosting me at Stanford University and for your fundamental inputs on my research. Kedar, thanks for our great discussions and all the knowledge you shared with me. A particular thanks my colleagues André, Akshay, Fabrizio, Federico, Irene, Lucia, Maurice, Matteo, Nando, Nitish, Nitish2, Raynard, Sonia, Stefano, Zeno and to all the football teammates of A.C. Brancaleone. I am thankful to Adam and Sebastian, for always being there to help me from the very beginning and for all the joyful times. Tomas thanks for the friendly chats on our train journeys. A special thanks goes to my two paronyms Salvo and Imco. Salvo, it has been a pleasure to work with you but most importantly to have met you. We have shared a lot during these years, and I am honored of this, my friend. Imco I am really grateful for your friendship, your support and the many unforgettable moments we spent together. Thanks also for the Dutch translation of the summary and propositions of this dissertation. A huge thanks goes to all the students I had the honor of supervising. You enriched me.

My thoughts of gratitude go to my family and my friends Stefania, Ernesto, Betty, and Paolo. Even in the distance, your presence has been fundamental every moment.

Alejandra, my special acknowledgment is for you, for all the unconditional support you gave me during all these years. If this work has reached an end is thanks to your

presence and all the wonderful time we shared together.

Finally, my deepest gratitude goes to my brother, Andrea, and my parents Alfonso and Maria to whom this thesis is dedicated. I could not become who I am now without your unconditional love.

A handwritten signature in black ink, appearing to read "Alonso Jiménez". The signature is fluid and cursive, with "Alonso" on the left and "Jiménez" on the right, separated by a vertical line.

Leiden, June 12th, 2019

List of publications

Journal papers

Rubino, A. and Pini M., 2019 “Adjoint-based unsteady optimization of turbomachinery operating with non-ideal compressible flows”. *Journal of Turbomachinery*, Manuscript Submitted.

Rubino, A. ,Vitale, S., Pini, M., and Colonna, P., 2019 “Fully-turbulent adjoint method for the unsteady shape optimization of multi-row turbomachinery”. *Journal of Turbomachinery*, Under Review.

Rubino, A., Pini, M., Kosec, M., Vitale, S., and Colonna, P., 2018 “A look-up table method based on unstructured grids and its application to non-ideal compressible fluid dynamic simulations”. *Journal of Computational Science*, **28** pp. 70-77

Rubino, A., Pini, M., Colonna, P., Albring, T., Nimmagadda, S., Economou, T. and Alonso J.J., 2018 “Adjoint-based fluid dynamic design optimization in quasi-periodic unsteady flow problems using a harmonic balance method”. *Journal of Computational Physics*, **372** pp. 220-235

Bahamonde, S., Pini, M., De Servi, C., Rubino, A. and Colonna, P., 2017. “Centrifugal turbines for mini-organic Rankine cycle power systems”. *Journal of Engineering for Gas Turbines and Power*, **139**(8), 082606.

Demierre, J., Rubino, A., Schiffman, J., Rubino, A., 2015. “Modeling and experimental investigation of an oil-free microcompressor-turbine unit for an organic Rankine cycle driven heat pump”. *Journal of Engineering for Gas Turbines and Power*, **137**(3), 032602.

Conference proceedings

Rubino, A., Vitale, S., Pini, M., and Colonna, P., 2018 “Assessment of fully-turbulent steady and unsteady adjoint sensitivities for stator-rotor interaction in turbomachinery”. *Proceedings of the Global Power and Propulsion Forum*, Montreal, Canada.

Rubino, A., Pini, M., and Colonna, P., 2017. “Unsteady simulation of quasi-periodic flows in Organic Rankine Cycle cascades using a Harmonic Balance method”. *Proceedings of the 4th International Seminar on ORC Power Systems*, Milan - Italy.

Pini, M., De Servi, C., Burigana, M., Bahamonde, S., Rubino, A., Vitale, S., and Colonna, P., 2017. "Fluid-dynamic design and characterization of a mini-ORC turbine for laboratory experiments". *Proceedings of the 4th International Seminar on ORC Power Systems*, Milan - Italy.

Demierre, J., Rubino, A., Schiffman, J., Rubino, A., 2014. "Modeling and experimental investigation of an oil-free microcompressor-turbine unit for an organic Rankine cycle driven heat pump". *ASME Turbo Expo*, Düsseldorf, Germany.

About the author

Antonio Rubino was born in Avellino, Italy. After receiving, in 2009, his Aerospace Engineering BSc cum laude from La Sapienza University of Rome, he enrolled in the Mechanical Engineering MSc program - Sustainable Process and Energy Technologies track - at TU Delft, in 2010. He graduated cum laude under the supervision of prof. Dirk Roekaerts, with a thesis on computational modeling of hydrogen production from the solar thermal cracking of methane. After a period at École Polytechnique Fédérale de Lausanne (EPFL), within the Laboratory for Applied Mechanical Design directed by prof. Jürg Schiffmann, in 2015 he joined as PhD candidate the group of Propulsion & Power led by prof. Piero Colonna, at the Aerospace Faculty of TU Delft. He is currently part of the team of the startup Dutch Analytics, focusing on the application of Artificial Intelligence to engineering problems.

